Morphology is a Link to the Past: examining formative and secular galactic evolution through morphology

A THESIS
SUBMITTED TO THE FACULTY OF THE GRADUATE SCHOOL
OF THE UNIVERSITY OF MINNESOTA
BY

Melanie A. Galloway

IN PARTIAL FULFILLMENT OF THE REQUIREMENTS
FOR THE DEGREE OF
Doctor of Philosophy

Advisor:
Lucy Fortson

month, 2017

Acknowledgements

Some acknowledgements

Dedication

Firstly dedicated to Zuko, for being the sweetest little bird.

Abstract

Galaxy morphology is one of the primary keys to understanding a galaxy's evolutionary history. External mechanisms (environment/clustering, mergers) have a strong impact on the formative evolution of the major galactic components (disk, bulge, Hubble type), while internal instabilities created by bars, spiral arms, or other substructures drive secular evolution via the rearrangement of material within the disk. This thesis will explore several ways in which morphology may impact the dynamics and evolution of a galaxy using visual classifications from several Galaxy Zoo projects. Section 1 will focus on the present morphology of galaxies in the local Universe ($z < 0.2$) using data from Galaxy Zoo 2 and Galaxy Zoo UKIDSS. Section 2 will examine populations of morphologies at various lookback times, from $z = 0$ out to $z = 1$ using data from Galaxy Zoo Hubble.

This thesis will first explore the impact of bars in disc galaxies on channeling gas from the outer regions of the disk to the inner few kpc necessary to fuel an active galactice nucleus (AGN). Using a sample of 19,756 disk galaxies at $0.01 < z < 0.05$ imaged by the Sloan Digital Sky Survey and morphologically classified by Galaxy Zoo 2, the difference in AGN fraction in barred and unbarred disks was measured. A weak, but statistically significant, effect was found in that the population of AGN hosts exhibited a 16.0% increase in bar fraction as compared to their unbarred counterparts at fixed mass and color. These results are consistent with a cosmological model in which bar-driven fueling contributes to the fueling of growing black holes, but other dynamical mechanisms must also play a significant role.

Next, the wavelength dependence on morphology is studied by comparing the optical morphological classifications from GZ2 to classifications done on infrared images in GZ:UKIDSS. Consistent morphologies were found in both sets and similar bar fractions, which confirms that for most glaxies, both old and young stellar populations follow similar spatial distributions.

Last, the morphological changes in galaxy populations are computed as a function of their age using classifications from Galaxy Zoo: Hubble. A sample of 14,663 disc galaxies from the COSMOS field at $0 < z < 1$ were identified as active or passive using a NUV-r / r -J diagnostic with rest-frame colors from the UltraVISTA catalog. This study found evolutions of the fraction of disk galaxies which are red, and the fraction of disks occupyting the red sequence from $z = 1$ to $z = 0$were mass-dependent: both fractions decreased or remained constant for high mass galaxies($\log(M/M_{\odot}) > 10.7$), but increased with time for low mass galaxies ($\log(M/M_{\odot}) < 10.7$). The results suggest that massive galaxies are more likely to retain their disk structure after quenching, and that 20% of massive galaxies go through a passive disk phase. Addionally, the challenges of visual classification that are particular to galaxies at high redshift we investigated. To address these biases, a new correction technuique is presented using simulated images of nearby SDSS galaxies which were artificially redshifted using the FERENGI code and classified in GZH.

Contents

List of Tables

List of Figures

Chapter 1

Introduction

The clues to galaxy formation and evolution are hidden in the fine details of galaxy structure.

Peng et al., 2002

The processes which govern the formation, growth, and eventual death of galaxies are uniquely difficult to investigate. A galaxy cannot ever be directly observed from its birth to its death; the only data available is a single snapshot of the Universe as it exists at the moment of observing, in its current cosmological state. To begin to map out the complete evolutionary history of a galaxy, astronomers must instead use other clever, indirect methods.

Morphology is one of the most powerful tools for revealing the physical processes that shape the evolution of galaxies. Details of a galaxy's structure are known to be linked with its color (Tully, R.B., Mould, J.R., Aaronson, 1982; Strateva et al., 2001; Baldry et al., 2004), recent star-formation (Conselice, 2006; Martin et al., 2007a; Mignoli et al., 2009), merger rate (Hammer et al., 2009; Oesch et al., 2010; Smethurst et al., 2017), and black hole activity (Athanassoula, 1992; Friedli & Benz, 1993; Schawinski et al., 2010), among others. There is no debate today that morphology is strongly linked to galactic evolution, but the extent to which these relationships hold is still difficult to quantify. Morphological classifications on scales large enough for results to claim statistical significance have been, in the past, unavailable. While expert visual classifications succeeded in accuracy, they lacked in numbers, and the opposite has been true for computational methods.

The research described in this thesis examines the link between morphology and evolution using data from the Galaxy Zoo project, which uses crowd-sourcing to provide a "best-of-both-worlds" approach to morphological classifications. To date, over one million volunteers have identified the structures of over one million galaxies, providing the benefits of both visual inspection and large numbers. With these data, the ways in which morphology drives (or is driven by) a galaxy's evolution has been investigated on a scale previously unachievable. Three topics will be considered in detail: the influence of bars on AGN activity (Chapter 4), the dependence of observed wavelength on tracing different stellar populations (Chapter 5), and the interplay between quenching mechanisms and morphological transformations of galaxies from redshift $z \sim 1$ (Chapter 6). This thesis also includes a detailed summary of the methodology used in collecting and reducing crowd-sourced data from Galaxy Zoo in the local Universe (Chapter 2) and introduces a new technique for debiasing high-redshift GZ classifications using data from simulated galaxies (Chapter 3). First, this Introduction will describe the typical components of a galaxy resulting from its formation, then give a brief summary of morphological types as have been defined historically, as well as the current evidence linking morphology to galaxies' past histories.

1.1 Galaxy Formation

Galaxies are believed to have initially formed from primordial density fluctuations shortly after the Big Bang, as predicted by the ΛCDM model of Cosmology (Peebles et al., 1994; Ryden & Ryden, 2016; Conselice, 2012; Silk et al., 2013). In this model, fluctuations δ can be characterized as the contrast of the local density in a region ρ as compared to the mean density of the Universe, $\bar{\rho}$: $\delta = \frac{\rho - \bar{\rho}}{\bar{\rho}}$. Gravitational instabilities will cause even small perturbations ($\delta << 1$) to grow exponentially with time; as $\delta \rightarrow 1$, the region collapses and breaks off from the expanding universe, becoming a self-gravitating structure.

The collapse of these protogalactic regions of overdensity triggered the formation of the first stars and galaxies around $z \sim 11$, about 400 thousand years after the big

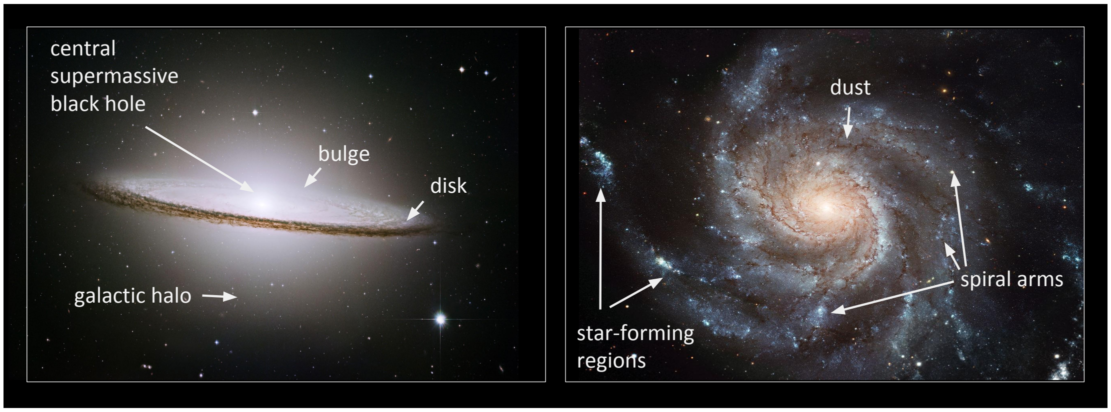

Figure 1.1 A side-on (left) and face-on (right) view of typical spiral galaxies. The edge-on view gives a clear visual of the disk, bulge, and galactic halo components. The face-on view reveals the detailed spiral structure within the disk. **Left:** Hubble image of Sombrero galaxy, M104. Credit: European Space Agency. **Right:** Hubble image of Pinwheel galaxy, M101. Credit: European Space Agency.

bang. At this time in the early Universe's history, the only baryonic matter in existence was Hydrogen and Helium. The very first stars to form in the first proto-galaxies were thus comprised of only these two elements; for this reason they are classified as "extemely metal-poor stars" (EMPs), or Population III stars. Heavier elements formed later in the cores of EMPs, allowing for the formation of the metal-rich stars more commonly observed in galaxies today. Different populations of stars are often classified by their metallicity, measured by the amount of heavier elements they contain relative to Hydrogen [Z/H]. Population II stars have metallcities of $[Z/H] < 0.1\%$; while they are still considered metal-poor, the presence of any metal requires that they were formed from gas generated from the deaths of the earlier Population III stars. Population I stars are the youngest observed, with metallicities $[Z/H] \sim 2 - 3\%$.

The structure and components of a typical galaxy are shown in Figure 1.1. Most galaxies are believed to form with a disk component, which is a product of the dynamics governing the initial galaxy formation. As large gas clouds cool and collapse, conservation of angular momentum causes the cloud to flatten and increase rotation speed, resulting in a disk shape. Young, Population I stars tend to form in the spiral arms of the disk, and particularly dense regions of star formation can give the arms a patchy appearance. Most galaxies are believed to contain a supermassive black hole in the center; while not observed directly, their influence on the galaxy in the form of feedback has been intensely studied (see Chapter 4 for details). Surrounding the black hole and often taking up a significant part of the galaxy is the central bulge, which tends to be comprised of older Population II stars. Both the disk and the central bulge can be destroyed as the galaxy evolves, transforming the galaxy's morphology into a purely elliptical structure. It is believed that this morphological evolution is tied to the shutting-down, or quenching, of star-formation, due to ellipticals tending to host only older stellar populations (see Chapter 6). Permeating the galaxy is the largest observable component: the galactic halo, which contains gas which fuels ongoing star-formation, and stars which extend to the outer regions of the galaxy. Last, all of the luminous components are embedded in a dark matter halo, which cannot be observed directly, but interacts with they baryonic matter gravitationally.

While the preceding described the elements of a typical galaxy, this does not begin to describe the wide range of morphological features that can be found. Disk galaxies for instance may have any number of spiral arms or no arms at all, or show evidence of rings or bars. Many galaxies do not even exhibit disk or elliptical structure to begin with; but have irregular or clumpy appearances. This next section will describe in more detail the variances in the shapes of galaxies, and how the different structures are grouped into morphological classifications.

1.2 Morphological Categorization of Galaxies

The oldest and most well-known system which categorizes galaxies based on their structure was developed by Edwin Hubble, commonly known as the "Hubble Tuning-Fork" (Hubble, 1926). Using a small sample of images of nearby galaxies, Hubble identified two fundamental morphological classes: spirals, which exhibited well-defined disk structure and clear spiral arms, and ellipticals, whose light distributions were smoothed over a roughly spherical shape. Only 3% of the sample had structures which deviated from these two categories, showing no evidence of rotational symmetry about a dominating nucleus; these were grouped together and labeled "Irregular". Although Hubble's system was originally based on a mere 400 galaxies, the classifications are still used for

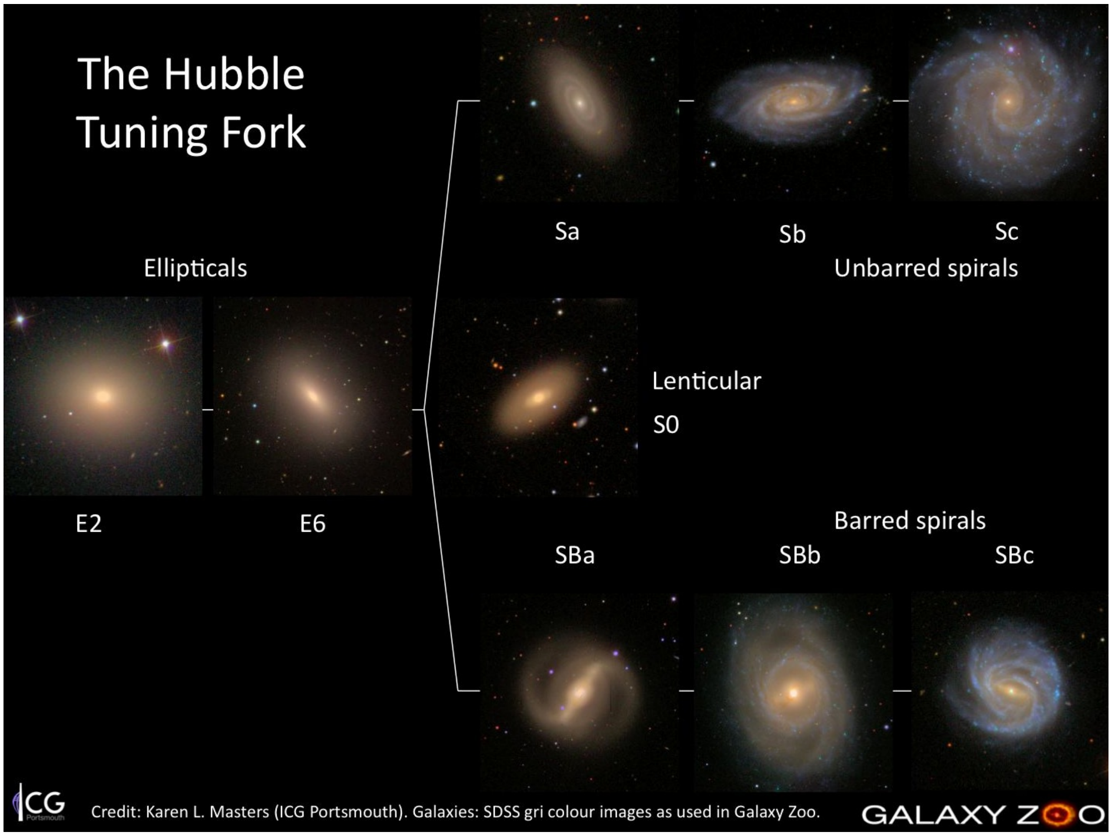

Figure 1.2 The Hubble Tuning fork with gri-composite SDSS images as examples of the various types. Credit: Karen Masters and The Sloan Digital Sky Survey (SDSS) Collaboration.

describing the morphologies of the millions of galaxies identifiable today (albeit with some modications, ie. DeVaucouleur's revised system (de Vaucouleurs, 1963)).

An example of Hubble's Tuning Fork is shown in Figure 1.2. The classifications defined on the Tuning Fork are as follows:

1.2.1 Ellipticals

The left side of the tuning fork contains elliptical galaxies, labeled "E". These were originally identified as circular through flattened ellipses whose luminosity faded smoothly from the center to "indefinite edges." The only other structural feature evident to subdivide this class were their ellipticities, defined in the traditional way $e = (a - b)/a$. A number is added to the label that represents the ellipticity, with the decimal omitted, whereby E0 would represent a purely spherical elliptical ($e = 0$), and E7 being the most elongated ($e = 0.7$). Hubble assumed that any galaxy with an ellipticity higher than 0.7 was no longer an elliptical, but more likely a highly-inclined spiral. It should be noted that these labels only classify the *projected* appearance; since ellipticals are tri-axial structures, this classification system is very dependent on the orientation angle of any ellipticals which are not perfectly spherical.

1.2.2 Spirals

The right side of the fork contains the various types of spiral galaxies. These all share the feature of having a flattened disk-shape, and often have a spherical bulge of stars in the center with spiral arms extending outward. Spirals whos arms originate from the central bulge follow the top of the fork, labeled "S", while those whose arms originate at the ends of a central galactic bar follow the bottom, labeled "SB". Both types are further classified based on the relative size of the central bulge and tightness of the arms. Those with large bulges and tighter arms are designated with an "a" attached to the spiral symbols, or "b"-"d" for decreasing bulge sizes and looser appearance of arms.

1.2.3 Lenticulars/S0s

Lenticular galaxies are placed at the center of the tuning fork, originally thought to be a transition stage to link the elliptical and spiral types. They exhibit the same overall disk-shape as the spirals, but have a smooth appearance rather than defined arms (which can make them difficult to distinguish from true ellipticals). They may or may not contain a galactic bar, giving them Hubble-type classifications of S0 (unbarred) or S0B (barred).

Hubble originally referred to the galaxies toward the left and right on the fork as "early" or "late"-type, respectively, simply for convenience in describing their relative positions on the sequence. While it is noted in his 1926 paper that any temporal connotation should be disregarded, the terms remain misleading in that it is now well-known that the early types tend to have older stellar populations, and late-types tend to be very young in their evolution. Nevertheless, “early-type” and “late-type” are still today used interchangeably when referring to ellipticals/S0s and disks.

1.3 Morphology as a tracer of galaxy evolution

The previous section described the most common morphological types of galaxies observed in the Universe. At this point it may be relevant to question why are there different types at all? Do the different shapes exhibit different evolutionary pathways, or is the snapshot we see of the distributions simply showing different stages of a track that all galaxies eventually follow? The answers to these questions aren’t fully known; however, examining the relationships between the different morphological types and their dynamics can provide strong insights to the full picture. This section will provide some examples of well-known links between morphology and galaxies’ evolutionary histories.

1.3.1 Color-Morphology Bimodality

The color of a galaxy is a strong indicator of its recent star formation history. In general, photometrically blue galaxies are in the process of forming new stars, emitting high energy blue light that is detected abundantly in short-wavelength filters. In contrast, galaxies which have ceased forming stars sometime in the past contribute most of their flux to long-wavelength filters, resulting in redder colors. Perhaps surprisingly, there is also a strong correlation between the color of a galaxy and its morphology. The majority of galaxies ($\sim 80\%$) have been shown out to $z \sim 1$ to follow this relationship: blue galaxies tend to be late-type spirals, and red galaxies tend to be early-type/elliptical (Tully, R.B., Mould, J.R., Aaronson, 1982; Strateva et al., 2001; Baldry et al., 2004; Conselice, 2006; Martin et al., 2007a; Mignoli et al., 2009). An example is shown in Figure 1.3.1. The vertical axis tracks the $u-r$ color, such that higher values are “redder” and smaller values are “bluer”. The horizontal axis tracks the absolute magnitude: more luminous galaxies towards the left, and dimmer towards the right. Bluer galaxies tend to have more featured morphologies; spiral arms appear more flocculant and clumps of star formation are apparent, generating irregular shapes in the extreme cases. Redder galaxies begin to have a much more smoothed-out and symmettric appearance, encompassing both ellipticals and bulge-dominated lenticulars. Color has long been considered such a strong indicator of morphology that it has been often used as a proxy for morphology when large-scale visual inspection has not been practical (Cooray, 2005; Lee & Pen, 2007; Salimbeni et al., 2008; Simon et al., 2009). This link is strong evidence that the processes which drive both morphology and the cessation of star formation are related in some way (Masters et al., 2010; Buta, 2013). This topic is explored in greater detail in Chapter 6.

1.3.2 Morphology and Stellar populations

At the most basic level, morphology is simply a tracer of the observed distribution of light in the galaxy, which in turn traces the distribution of stars, gas, and dust. All light is not emitted equally, however: gas and younger, Population I stars will emit more light in optical and UV wavelengths, while older Population II stars emit more strongly in the infrared. Since these populations may have very different light distributions, there is inherently some dependence on morphology with the wavelengths within which it's observed.

Morphologies observed in optical bands are sensitive to pockets of star-formation regions, but other features can be obscured due to dust extinction, particularly those comprised of older stellar populations (such as bars); this can give galaxies an overall "patchy" appearance. In contrast, they appear smoother in the near-IR, where the effects of dust extinction are reduced and the older stellar populations dominate. An interesting effect occurs as the observation wavelength moves into the mid-IR: here, dust tends to re-radiate the light absorbed from star-formation regions, re-creating the appearance of the optical-band morphology. There has been debate as to whether the optical and near-IR morphologies are de-coupled to the extent that two classification schemes, one for each wavelength range, is justified (e.g. Block & Puerari (1999)). Chapter 5 will examine the optical and near-IR morphologies measured by Galaxy Zoo to add to this debate, as well as investigate whether bars are in fact easier to identify in the near-IR.

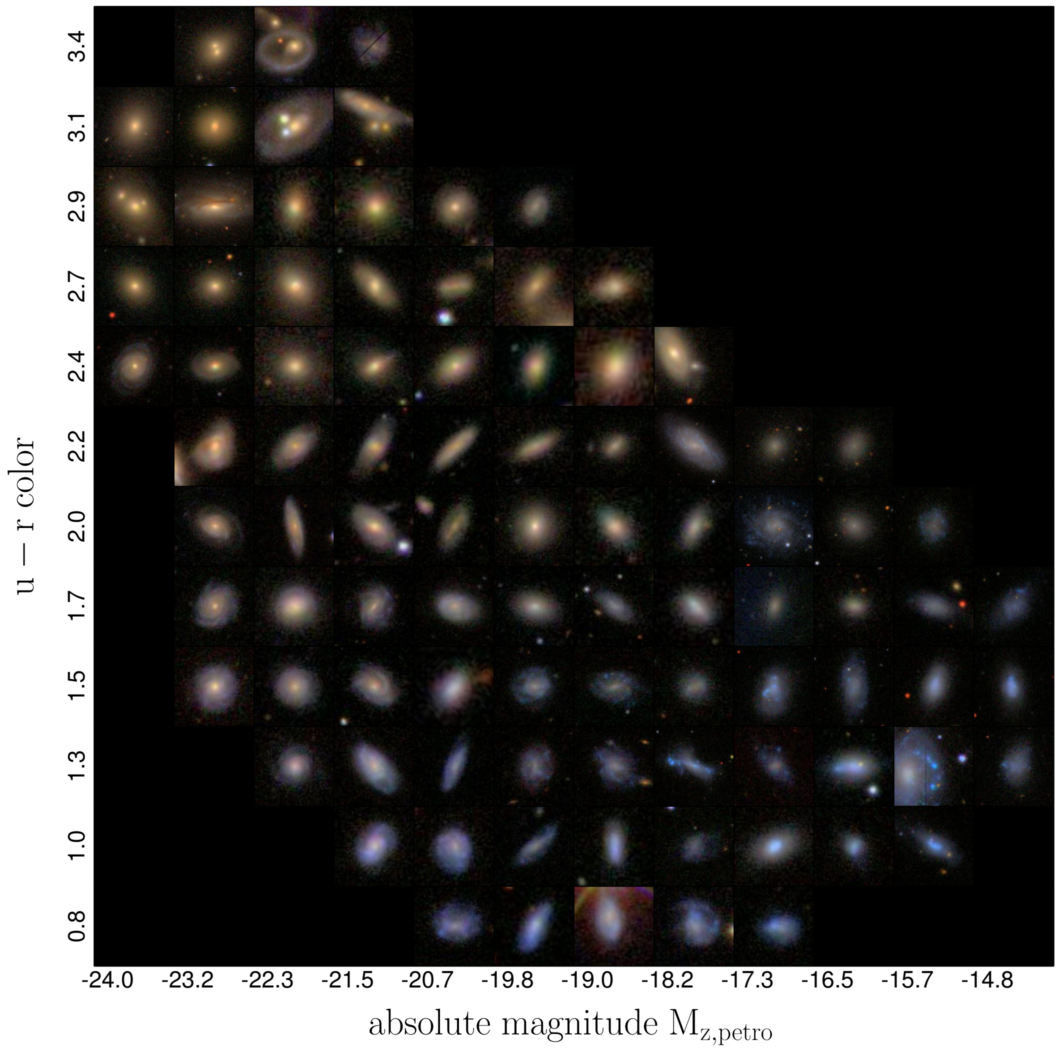

Figure 1.3 Color vs. Absolute Magntitude Diagram, illustrated using SDSS galaxies. In each color-magnitude bin, a random galaxy was selected meeting the criteria defined by that bin. The bottom-left and upper-right regions contain very few or zero galaxies, a consequence of typical galaxy evolution. As galaxies age and continue forming stars, they build up more stellar mass, increasing their total luminosity. Hence the most luminous galaxies tend to be older and more massive, and unlikely to be dominated by younger stellar populations. This results in a dearth of luminous blue galaxies (bottom left) or faint red galaxies (upper right).

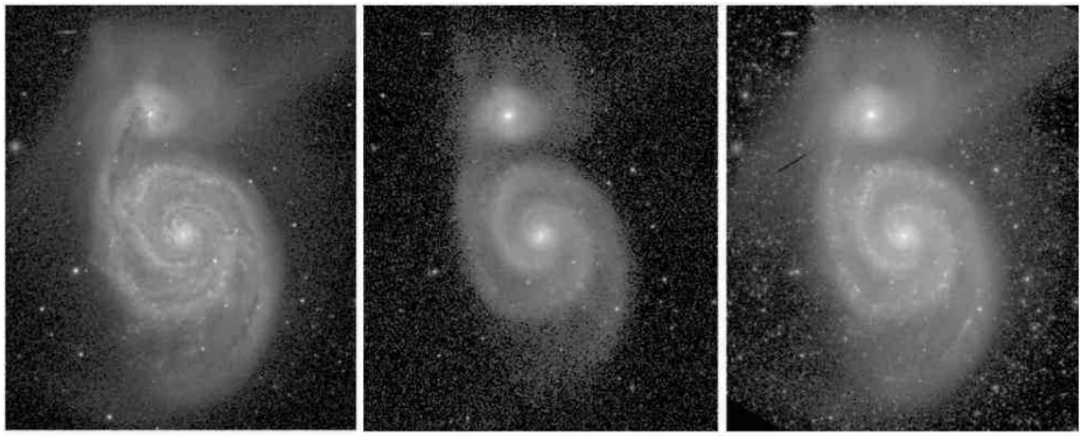

Figure 1.4 Credit: Buta (2013), Figure 2.51. Spiral galaxy M51 observed in optical B-band (left), near-IR (middle), and mid-IR (right). Visible in the B-band image are patchy regions of star-formation and dust lanes, which become invisible in the near-IR, giving an overall smoother appearance. The mid-IR image shows regions where the dust re-radiates light absorbed from star-forming regions, giving a similar appearance to the optical image.

1.3.3 Morphology and Environment

A galaxy's environment can also be a predictor of its morphology. The morphology-density relationship, first quantified by Dressler (1980), observes an abundance of elliptical/ early-type morphologies in denser environments (de Souza et al., 1982; Postman, M. Geller, 1984). Since the merger rate correlates with environment density, it could be suggested that early-types are often the by-products of mergers, as opposed to a stage of isolated secular evolution.

There is also evidence of an environmental impact on morphology even in the absence of direct merging. For example, ram pressure (Gunn & Gott, 1972) exerted by the local intracluster medium can severely distort the gas distribution in a galaxy, resulting in asymmetries in the disk (ex. NGC 4402; see also Chapter 6).

1.3.4 Bars

Buta (2013) describes barred galaxies as "the ultimate in galaxy morphology." His reasoning is simple: just by observing an image of a bar, it is easy to identify it as a major perturbation in an otherwise stable system. There is a great deal of truth in this; such a disruption will no doubt have significant effects on the fate of its host galaxy. In this way, bars are arguably one of the most important structural features that can shape a galaxy's evolution.

A key feature of bars is their ability to drive gas from the outer regions of the galaxy to the center (Athanassoula, 1992; Friedli & Benz, 1993; Sellwood & Wilkinson, 1993; Shlosman et al., 1989; Ann & Thakur, 2005), which can affect the galaxy's evolution in numerous ways. One such consequence is the formation of a pseudo-bulge (Kormendy & Kennicutt, 2004; Sheth et al., 2005). While this is seen in simulations, this theory is difficult to confirm observationally, as the bar may or not be destroyed by this process (Athanassoula et al., 2005), causing difficulty in identifying a correlation between populations of galaxies with both bars and bulges.

An increased inflow of gas to the center may also increase central star-formation. Several studies have reported an increase in star-formation rates in the central region of barred galaxies vs. their unbarred counterparts (Hawarden et al., 1986; Ho et al., 1997), although this may only be true for strong bars. Martinet & Friedli (1997) and Zhou et al. (2014) find low rates of star-formation in galaxies with weak bars, suggesting they are unable to trigger significant star formation. Strong bars, however, show both the highest and lowest rates of star-formation. (Sheth et al., 2005) found a significant portion of barred galaxies with no molecular gas detected in the nuclear region, which may suggest that for these galaxies, the bar has already driven most of the gas to the nuclear region, where it was consumed by star-formation. Bars, then, seem to play two important roles in the star formation history of their host galaxies - both by increasing star formation, and subsequently driving the quenching process.

Bars also may be one of the mechanisms which enable the fueling of an active galactic nucleus (AGN), whose evolution is believed to be strongly linked to that of their host galaxies (Schawinski et al., 2007, 2010; Antonini et al., 2015; Yang et al., 2017; Zubovas & Bourne, 2017) (and Heckman & Best (2014) for a comprehensive review). The requirements for onset of accretion onto the central SMBH are still unclear, but Moles et al. (1995) argues that non-axisymmetric components of the gravitational potential may be a necessary condition; a requirement which bars easily satisfy. While simulations have shown bars to provide the necessary inflow to ultimately fuel an AGN (Athanassoula, 1992; Friedli & Benz, 1993), observations have shown mixed results. Many have found an excess of AGN in barred samples of galaxies (Knapen et al., 2000; Oh et al., 2012), while others find no difference (Ho et al., 1997; Mulchaey & Regan, 1997; Cheung et al., 2015). A discussion of the discrepencies between these results, along with my own investigation of this topic, is the subject of Chapter 4.

The examples listed are only a few of the well-known relationships between the evolution of galaxies and their morphologies. There is little doubt amongst astronomers that morphology and galactic evolution are linked; however, as evident in these examples, some links are still inconclusive and the research of these relationships is still ongoing. Results are becoming more defined now, as methods to classify galaxies according to their morphologies are consantly improving. Some of the results listed from previous decades suffered from low-sample statistics, where it was only feasible to visually classify handfuls of galaxies in a single study. Today, more robust methods are able to categorize galaxies morphologically in a fraction of the time once required. The next section will explore the evolution of classification methods used to obtain galaxy morphologies for such studies.

1.4 Methods for morphological classification

Historically, morphological classification been done by visual inspection of small samples of images (e.g. Hubble (1926); Sandage (1961); de Vaucouleurs (1963); Block et al. (1994); Eskridge et al. (2002); Buta et al. (2010)), by either a single person or handful of experts. This method is becoming obsolete as we enter a new era of large data, with surveys such as the Sloan Digital Sky Survey (SDSS) and HST-Legacy, and upcoming James Webb Space Telescope and the Large Synoptic Survey Telescope, producing high-quality images of hundreds of thousands of galaxies. To date, the largest morphological catalogs created by visual inspection from a small group of experts includes the Nair and Abraham catalog (Nair & Abraham, 2010) with $\sim$ 14,000 galaxies, RC3 Catalog (de Vaucouleurs, 1991) with $\sim$ 23,000 galaxies, and MOSES (Schawinski et al., 2007) with 50,000 galaxies. Even these catalogs, while successful, do not compare in size to the newly incoming data, and so more powerful and robust efforts are required to obtain morphological information on these scales.

An ideal method for handling the large amounts of data would be an automated classification scheme. Several such algorithms have been developed, with some success (Odewahn et al., 2002; Peng et al., 2002; Conselice, 2003; Scarlata et al., 2007) by using the stellar light distribution of the galaxy to assign it a morphological class. These approaches tend to be limited to identifying the global morphologies (ie, spiral or elliptical), and lack the precision to accurately identify finer, detailed features (such as bars or the number of spiral arms) (Beck et al. 2017). Further, they tend to incorporate proxies such as color as their input, which are often not accurate as previously noted. Much more promising techniques are currently being tested which incorporate the use of machine-learning algorithms and neural networks (Dieleman et al., 2015; Huertas-Company et al., 2015),(Beck et al. 2017), but these require massive and accurate training-sets to perform properly. One alternative to direct visual classification of morphologies is the use of proxies such as color, mass, surface brightness profile, or some combination of several. Color is commonly used as a proxy because of its mostly-tight relationship global morphology, in that spirals tend to be red and ellipticals tend to be blue. This type of morphological classification will always suffer from a high degree of inaccuracy, as there is no perfect physical measurement that is 100% correlated with shape. The morphology of a galaxy typically traces the dynamical history, whereas proxies such as color trace stellar growth; these two properties thus reveal different evolutionary histories on possibly very different timescales (Fortson et al., 2012). Last, while there are several proxies which correlate somewhat with the probability of a galaxy being spiral or elliptical, very few could be used to identify finer substructures or more detailed morphological features within the overall shape.

A best-of-both-worlds approach uses the power of crowdsourcing, which uses the input of tens of thousands of individuals to visually classify galaxies in a fraction of the time achievable by a handful of experts; such a method was developed by Galaxy Zoo, the data from which is used throughout this thesis. The Galaxy Zoo project uses a simple online interface whereby images of galaxies are visually inspected by volunteers, which allows the identification of intricate morphological features to a higher degree of accuracy than computer algorithms today can achieve. Addionally, with a required 40+ independent classifications per galaxy, the resulting classifications carry a greater statistical significance than those generated from one or a few experts. The next chapter will describe how Galaxy Zoo collects data from volunteer citizen scientists, how the data is reduced and debiased, and finally how the data is used to assign morphological classifications to large samples of galaxies.

Chapter 2

Methodology

2.1 A Brief History of Galaxy Zoo

The increasing accessibility of the Internet in the last few decades has allowed scientists to "outsource" tasks online using citizen science, with huge success. The project Seti@Home [1] (Anderson, 2002), launched in May 1999, was one of the first projects that revealed the massive number of people willing and excited to help contribute to science. Since launch, over 5 million participants donated idle time on their computers to assist SETI in analyzing radio telescope data to help in the search for extraterrestrial life. Citizen scientists were also extemely interested in taking in an even more active role in research, as seen in a later project Stardust@Home [2] , in which volunteers searched for dust grains in data via a web interface. This project engaged over 20,000 volunteers, and those who discovered dust grains were invited to become co-authors on the announcement papers. Early citizen science projects such as these inspired the launch of Galaxy Zoo.

The real need for a faster method of obtaining galaxy morphologies for large samples was realized in 2007 by graduate student Kevin Schawinski, who was studying populations of elliptical galaxies as work for his PhD thesis at Oxford University. At the time, the accepted and fastest method for identifying early-type galaxies (in large quantities) was to select based on SDSS-measured spectra (Bernardi et al., 2003). He

[1] http://setiathome.berkeley.edu/
[2] http://stardustathome.ssl.berkeley.edu/

knew, however, that this sort of method would exclude potential star-forming ellipticals (as well as potentially include passive spirals), due to the non-perfect correlation between morphology and color, as mentioned in the previous Chapter. So, realizing that a visual inspection of the direct appearance of the galaxies was necessary to create a complete sample of ellipticals independent of color, Schawinski devoted an entire week to classifying 50,000 galaxies by eye (MOSES, Schawinski et al. (2007)).

The grueling task of classifying only a small fraction of the SDSS main sample ($\sim$ 900,000 galaxies) made it apparent that a better method for visual classification was becoming neccessary. Inspired by the 20,000 volunteers who participated in the Stardust@Home project, Schawinski and Oxford colleague Chris Lintott realized that it would only take a few years to classify the entire SDSS main sample, assuming a similar participation response as StarDust. This led to the launch of Galaxy Zoo in July, 2007. This first phase (known now as Galaxy Zoo 1, or GZ1), included the brightest (Petrosian magnitude $r < 17.77$ AB mag) 893,212 images from SDSS Data Release 6 (Strauss et al., 2002; AdelmanMcCarthy et al., 2008). In this project users were asked to indentify simple features of a given galaxy, including whether it was elliptical or spiral, clockwise or anticlockwise, a merger, or star/other (the original interface with options is shown in Figure 2.1).

In just the first day of the site being live, 70,000 classifications were coming in each hour - a rate much faster than the developers had ever expected. In less than a year, the entire SDSS main sample was classified by an average of 38 volunteers per galaxy. Following the GZ1 data release paper published in April, 2008 (Lintott et al., 2008), over a dozen scienific publications were released which made use of the GZ1 morphological classifications [3] . Significant results included the discovery of a large population of passive red spirals in the local universe (Masters et al., 2010), the existance of star-forming blue ellipticals (Schawinski et al., 2009), "green peas," a new class of galaxies exhibiting extremely high specific star formation rates (Cardamone et al., 2009), and "Hanny's Voorwerp," the first example of AGN-photoionized clouds detected near galaxies no longer actively hosting AGN (Lintott et al., 2009).

Galaxy Zoo continued hosting additional sets of galaxy images for crowdsourced classification following the success of GZ1. The immediate successor, Galaxy Zoo 2

[3] https://www.zooniverse.org/about/publications

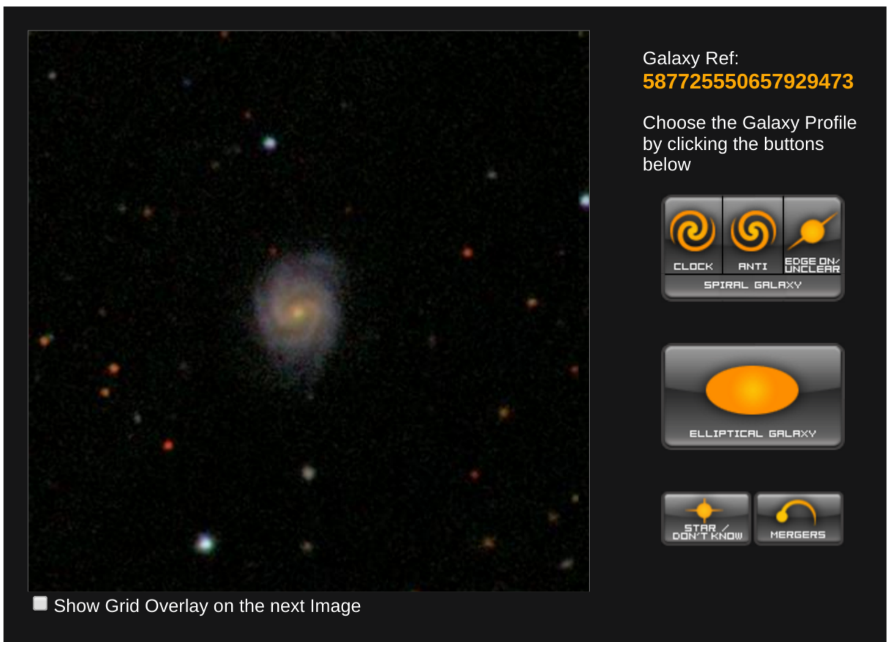

Figure 2.1 Example of the interface seen by users of Galaxy Zoo 1. On the left is an image of a galaxy from the SDSS main sample. On the right are possible features the user may identify about the galaxy by clicking the relevant option(s). Once complete, they are shown another galaxy.

(GZ2) was a subset of GZ1, consisting of the brightest 25% of the SDSS main sample, and was the first to implement the decision tree structure (Figures 2.2 and 2.1). Later projects introduced a variety of imaging types, including infrared (GZ:UKIDSS), high-redshift (GZ:Hubble, GZ:CANDELS), and even simulated images (Ferengi (artificially redshifting), GZ:Hubble (color-inversion and simulated AGN), Illustris). A summary of all major projects is given in Table 2.1.

It is also worth highlighting the educational impact of a citizen science approach to data collection. Science education research has shown that active participation is a critical component in scientific learning. S. Michaels, A. W. Shouse (2008) define four "strands" of skills that students must obtain to be considered scientifically proficient, the fourth being "participating productively in science." Citizen science provides both students and the general public the opportunity to actively participate in science without having to already be experts in the field, and it has been obvious so far that the volunteers are enthusiastic to do so. Raddick et al. (2010) investigated the motivations driving the participation of GZ users through surveys and interviews, and found the desire to contribute significantly to important research was one of the primary examples (other motivations including enjoying the beauty of the galaxy images and a general interest in astronomy).

The remainder of this Chapter will outline the common practices used to turn Galaxy Zoo data "from clicks to classifications," through the use of consistency-weighting the user votes and adjusting vote fractions for redshift bias.

2.2 Galaxy Zoo Data Reduction

2.2.1 User weighting by consistency

A typical Galaxy Zoo project collects classifications from over 10,000 unique volunteers. With such large numbers of classifiers, there exists the possibility that some fraction of these are "unreliable", that is, their votes are consistent with random clicking. To ensure that all votes collected represent real classifications, a weighting technique is implemented to detect and down-weight unreliable votes.

The weighting scheme used for all GZ projects represented in this thesis (GZ2, GZ:UKIDSS, and GZ:Hubble) evaluates the consistency of each user by how often their

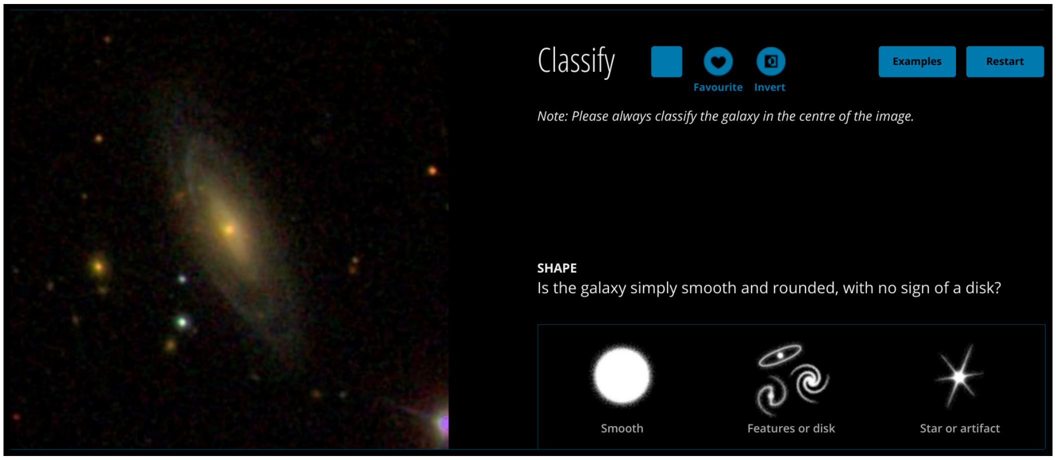

Figure 2.2 Example of the interface seen by users of Galaxy Zoo 2. On the left is an image of a galaxy, on the right are possible features the user may identify about the galaxy by clicking the relevant option. Unlike GZ1, subsequent questions appear about the same galaxy depending on their answers to the preceding questions, following a decistion tree format (see Figure 2.1 for a visual of all possible pathways.)

Table 2.1 List of major completed Galaxy Zoo projects since 08/2017. N_{images} refers to the number of *subjects* classified in the project, which may include duplicate unique galaxies (see data release publications for details). $N_{classifications}$ refers to the sum of classifications recieved for each subject, not the number of *clicks* a subject received (so a user answering 3 questions for a single galaxy would count as 1 classification, not 3). *Surveys included in HST Legacy are AEGIS, COSMOS, GEMS, GOODS-N and GOODS-S single and 5-epoch.

	dates active	source	N_{images}	$N_{classifications}$
GZ1	7/07 - 2/09	SDSS DR6 main sample	893,212	34,617,406
GZ2	2/09 - 4/10	SDSS DR7 $r < 17$ + stripe-82	366,178	16,340,298
GZ:Hubble	4/10 - 9/12	HST Legacy* + SDSS stripe-82	182,525	10,349,357
GZ: CANDELS	9/12 - 11/13	CANDELS	52,073	2,149,206
Ferengi	10/13 - 1/14	SDSS, artificially redshifted	6,624	265,092
GZ:UKIDSS	10/13 - 5/14	UKIDSS	70,977	2,749,010
DECaLS	9/15 -	DECaLS	94,024	4,192,479
Illustris	9/15 -	Illustris, simulation	63,640	1,174,018
Ferengi 2	12/16 - 2/17	SDSS, artificially redshifted	7,488	300,890
GAMA	1/17 -	GAMA-KiDS	19,605	533,671
Totals			1,756,346	72,671,427

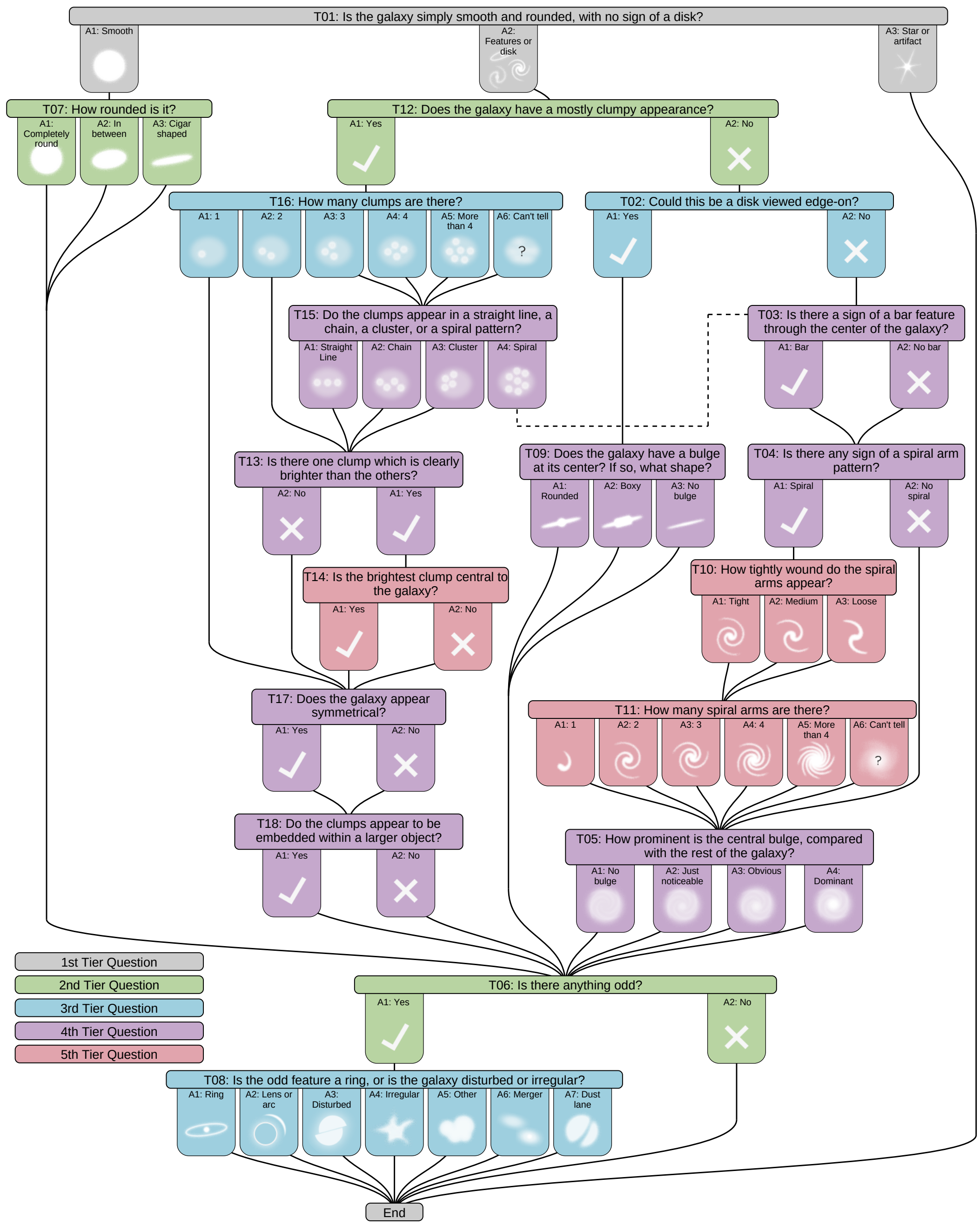

Figure 2.3 Decision tree used in the Galaxy Zoo:Hubble project. The colors indicate the "Tier" level of the question. Gray represents 1st-Tier; these are asked of all users. Green are 2nd-Tier; these are only asked after responding to a 1st-Tier question, and so on. This tree is identical to GZ2 and UKIDSS, except for the addition of the clumpy questions T12-T18.

votes agree with the majority for each task in the decision tree. The consistency rating κ for a single task is defined as:

$$\kappa = \frac{1}{N_r} \sum_{i=1}^{N_r} \kappa_i \tag{2.1}$$

N_r represents the total number of responses to the task, $\kappa_i = f_r$ if the user's vote corresponds to response i, and $\kappa_i = (1 - f_r)$ if it does not, where f_r is the vote fraction for each response in the task. In this system, κ is then high if the vote agrees with the majority, and low if it does not.

The mean consistency computed for each response given is defined as the user's overall consistency $\bar{\kappa}$, summed over all tasks. The user is then assigned a weight w defined as:

$$w = \min(1.0, (\bar{\kappa}/0.6)^{8.5}) \tag{2.2}$$

All votes are then recalculated using the user weights, and the process is repeated as many as three times to ensure convergence. It can be seen in Equation 2.2 that a user's weight value is always less than or equal to one; in other words, users are only downweighted in cases of noticeable inconsistency, and never upweighted. Willett et al. (2013) show that most users with low consistencies tend to only have contributed a handful of classifications, which could either indicate that users become more accurate as they classify more galaxies, or that inconsistent users are inherently less likely to be interested in the project.

2.2.2 Classification bias in the local Universe

For samples of galaxies limited to the local universe ($z \lesssim 0.2$), there is no expected redshift dependence on the morphological classifications. Therefore, we would expect vote fractions representing different morphological features to be constant with respect to redshift. However, this is not the case - the average vote fraction for features, bars, spirals, and several others actually tend to *decrease* with redshift. Since we assume such features should be equally prevalent at any redshift in this small range, some bias unrelated to any true morphological evolution must be affecting the vote fractions.

The source of this bias comes from the apparent size and brightness of the images of the galaxies being classified, which are strongly affected by redshift. Images of more distant galaxies appear smaller and dimmer, and therefore finer features are simply more difficult to detect. This sort of classification bias is a problem with any morphological classification, whether it be expert classifiers, automated dection, or crowd-sourced visual inpsection.

This section will describe the methods used to correct this type of classification bias for galaxies in the local Universe, where no true morphological evolution is a factor. Beyond the local Universe this assumption is no longer valid, so techniques implimenting classifications of artificially-redshifted galaxies are used for calibration; these are described in detail in Chapter 3.

Debiasing Galaxy Zoo 2: W13 method

The first technique for debiasing Galaxy Zoo classifications was developed by Bamford et al. (2009). This method was used again for the GZ2 classifications, with slight modifications to account for 1) the GZ2 classifications were derived from votes through a decision tree, rather than a single response per galaxy, and 2) answers to tasks in GZ2 are not all binary as they were with GZ1. This section will describe the technique in the context of GZ2, noting that the physical assumptions used are the same in both methods. It will hereafter be refered to as the W13 method (to differentiate from the methods in subsequent sections).

The debiasing technique used in GZ2 assumed firstly that galaxies with similar brightnesses and sizes should, on average, share similar mixes of morphologies at any redshift in the small range of this sample $0 < z < 0.25$. Using this assumption, galaxies were grouped into bins of absolute magnitude M_r, Petrosian effective radius R_{50}, and redshift. For each task in the GZ2 decision tree, the vote fractions for each response in any size/magnitude bin were adjusted so that their average matched the average vote fraction of its lowest-redshift bin. This method is described in detail in Willett et al. (2013), but the main approach is as follows:

For a given size/magnitude bin, the ratio of vote fractions for a pair of responses i and j for a single task can be written as f_i/f_j. Due to the classification bias described above, this ratio may not reflect the “true” ratio for this size/magnitude range, but can

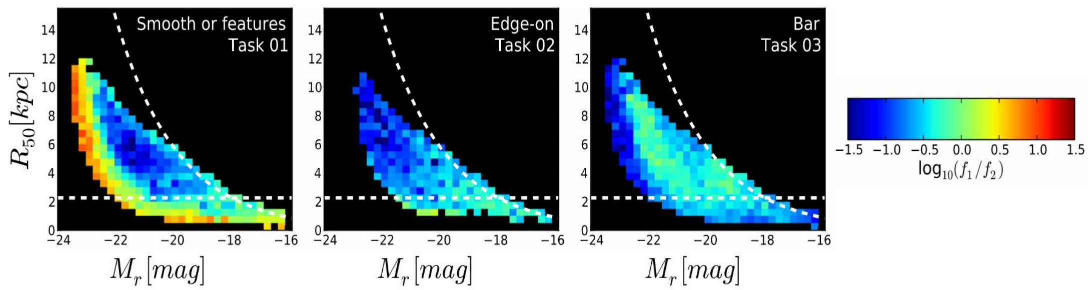

Figure 2.4 Local ratios of morphologies for the first three tasks in the GZ2 decision tree, used to derive debiased votes for the GZ2 sample. The full figure which includes baseline ratios for all tasks in the GZ2 decision tree is shown in Willett et al. (2013), Figure 5.

be written in terms of the true ratio with a multiplicitave constant $K_{i,j}$:

$$\left(\frac{f_i}{f_j}\right)_{z=z'} = \left(\frac{f_i}{f_j}\right)_{z=0} \times K_{i,j} \tag{2.3}$$

Where $(f_i/f_j)_{z=z'}$ represents the ratio measured in a size/magnitude bin at $z = z'$, and $(f_i/f_j)_{z=0}$ is the "true," or intrinsic ratio of vote fractions, defined as the ratio measured in the lowest redshift bin.

Figure 2.4 shows the local ($z = 0$) ratios of f_i/f_j for the first two responses i and j for the first three tasks of the GZ2 decision tree, which are used to calculate the debiased vote fractions as outlined above. For Task 01, f_i/f_j corresponds to $f_{smooth}/f_{features}$, for Task 02 $f_{edgeon}/f_{not\ edgeon}$, and for Task 03 $f_{bar}/f_{no\ bar}$. The figure demonstrates the size and magnitude dependence of the most local morphological populations: for example, in Task 01, the largest and brightest galaxies tend to have more votes for "smooth" than "featured", which is consistent with our current understanding that ellipticals tend to be larger and more massive than spirals.

The results of this method for the first three Tasks in the GZ2 decision tree are shown in Figure 2.5. For each response in each Task, the average vote fraction is calculated as a function of redshift. Solid lines represent the weighted/non-debiased votes and the dotted lines are the debiased votes using this method (hereafter W13). The redshift dependence on vote fraction is very evident in the downward trend of the solid lines corresponding to responses which detect features, such as $f_{features}$ and f_{bar}

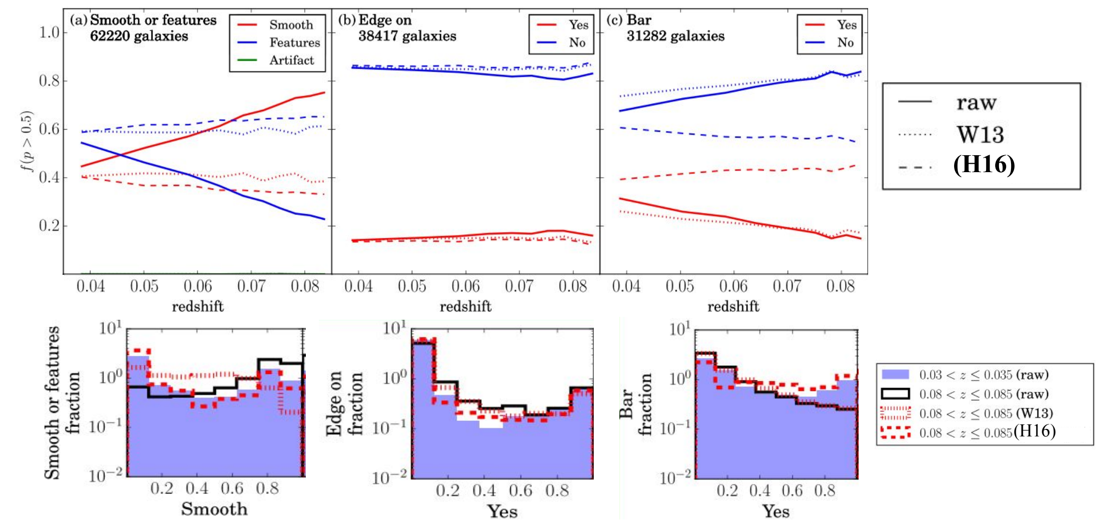

Figure 2.5 Credit: Hart et al. (2016), Figures 8 and 9. **Top**: Plotted are the fraction of galaxies with vote fractions greater than 0.5 for each reponse to the first 3 tasks, where the solid lines are the raw vote fractions, dotted are the W13 debiased vote fractions, and dashed-dotted lines are the debiased with the H16 method. As an example of the effect of the debiasing, see panel (a): without the debiasing, the number of galaxies with a "smooth" majority vote fraction increashes sharply from $z = 0.04$ to $z = 0.8$, a range assumed to be local enough such that no true morphological evolution should be observed. Both debiasing methods work to keep the fractions constant over this redshift range, although the H16 method is more effective at higher-tier questions. **Bottom**: Distributions of vote fractions for the first answer to the first 3 tasks, for the low-redshift raw data (solid blue), higher redshift raw data (black solid line), W13 debiased (red thin-dashed line), and H16 debiased (red thick-dashed line). Both methods are successful at shifting the high-redshift distributions to match the low-redshift distribution, with H16 being slightly more effective at matching the shape of the distributions.

in this example. The dashed lines show the effect of the debiasing which attempts to flatten out the distribution. Full figures showing the results for all Tasks in the tree are available in Willett et al. (2013) (Figure 3) and Hart et al. (2016) (Figure 8). From 2013-2017, the debiased vote fractions calculated in this method were used in the majority of published Galaxy Zoo papers, and are used in the study described by Chapter 4.

Debiasing GZ2 and UKIDSS: H16 method

The W13 debiasing method is successful at adjusting the vote fractions to more accurately resemble the "true" distribution of morphologies at low redshift, but has two primary limitations. First, the rectangular binning of all three parameters (size, magnitude, and redshift) is only effective when the parent sample is large enough that sufficient data per bin remains available after the three dimentional binning. (For example, to requre 10 bins in each parameter with at least 50 galaxies per bin, a parent sample must contain at minimum N=10x10x10x50=50,000 galaxies, assuming a perfectly even distribution of values in each parameter). GZ2 is not so affected by this limitation, with a parent sample size of $\sim$ 250,000 galaxies. However, this is only true when considering the debiasing of the first Task, which is asked of every galaxy. After this Task, the parent sample for computing a correction term decreases as not all Tasks are asked of every galaxy; for example, the Tier 4 Task which asks for the number of spiral arms is only seen by the majority of volunteers in 33,000 galaxies of the full GZ2 sample. Thus debiasing this Task would require a smaller limit on the number of bins per dimension or the number of galaxies per bin, both of which decrease the robustness of the method. Even with a large parent sample for any Task, the rectangular binning is also limited by the inability to account for data which lie on the outer edges of the parameter space, as there tends to be insufficient data in the outer bins.

A new debiasing technique (hereafter H16) was developed by Galaxy Zoo member Ross Hart (Hart et al., 2016) which substitutes Voronoi binning for the rectangular method. Voronoi binning optimizes the shape and location of bins based on the desired signal for each bin; in this case, the number of galaxies per bin is set initially, and the bins are drawn to fulfill that requirement. In this way, the number of galaxies available for measuring the change in vote fractions for each bin is maximized. Thus, this method is more effective at debiasing smaller samples (such as GZ:UKIDSS which contains only ∼70,000 galaxies; see Chapter 5), where the three dimensional binning preserves the signal in each bin. An example of Voronoi binning GZ2 data in size and magnitude is shown in the left panel of Figure 2.6. Each size and magnitude bin is then Voronoi-binned by redshift.

The second limitation of the W13 method is that while it effectively corrects the vote fractions for any Task so that the average morphology is constant as a function of redshift, it does not account for the *distribution* of morphologies at low redshift. This produces reasonable results when the corrected values are used for population studies, where the percentage of galaxies exhibiting a particular morphology are desired, but may not always reproduce accurate *individual* vote fractions. The H16 method instead corrects the high redshift vote fractions based on the change in distribution of vote fractions observed at low redshift, rather than comparing to only the average values. The first step of this method is shown in the right panel of Figure 2.6. For the low redshift bin of a given task, the cumulative distribution of vote fractions for each response is fit with a continuous function, which is used as the baseline distribution (similar to the baseline average votes in the W13 method.) The vote fractions making up the cumulative distributions at higher redshifts are then adjusted as needed to match the low redshift distribution as closely as possible.

Results of this method are shown and compared to W13 in Figure 2.5. Plotted on the top panel are the fraction of galaxies with vote fractions greater than 0.5 for each reponse to the first three tasks, where the solid lines are the raw vote fractions, dotted are the W13 debiased vote fractions, and dashed-dotted lines are the debiased with the H16 method. Both methods are succesful in stabilizing the average morphologies over this local redshift range. The bottom panel shows the distribution of vote fractions of a low-redshift bin (solid blue histogram) and high redshift bin, again for the raw votes (black solid line), W13 method (light dashed red), and H16 method (solid dashed red). It can be seen here that while both methods can reproduce the average vote fractions at low redshift, the H16 method is more succesful in reproducing the distribution of votes at low redshift. In this thesis, W13 debiased vote fractions were used in Chapter 4 to conduct the study examining the relationship between bars and AGN using GZ2 data, specifically votes from the first three Tasks in the tree. Chapter 5 examines a smaller data set, the UKIDSS sample, which contains 70,000 galaxies, much smaller than GZ2.

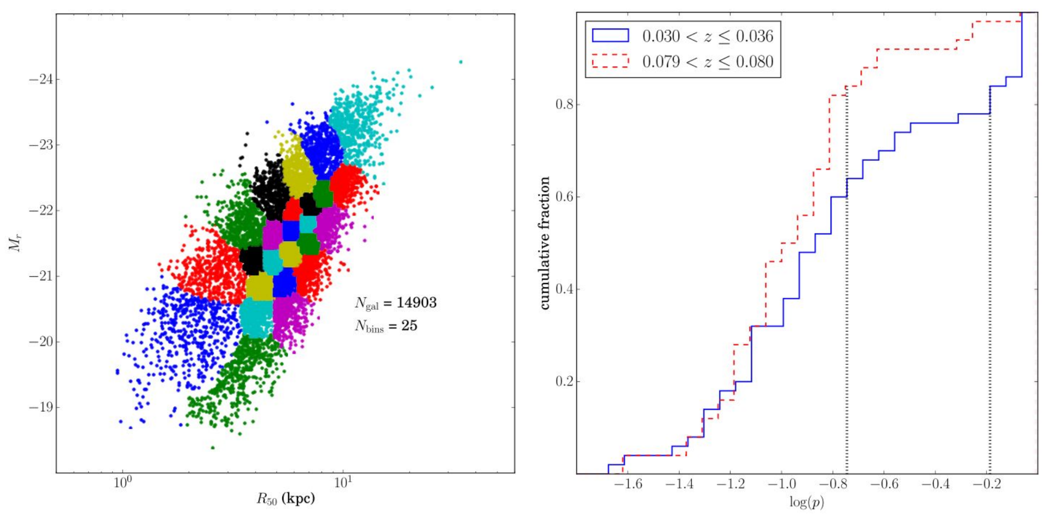

Figure 2.6 Credit: Hart et al. (2016), Figures 5 and 6. **Left:** Voronoi bin distribution for the "> 4" answer to the spiral arm question in GZ2. Each bin is further divided into Voronoi bins, such that each final $R_{50} - M_r - z$ bin contains at least 50 galaxies. **Right:** Cumulative distribution of vote fractions (in log-space) of a single $R_{50} - M_r$ bin, split between a high redshift bin (red dashed line) and a low redshift bin (blue solid line). The debiasing method adjusts the high-redshift vote fractions to match the distribution of the low-redshift distribution.

For the reasons given in this section, the H16 method was used to debiase the votes used in that study.

The science in Chapter 6 examines galaxies residing far beyond the local Universe ($0.2 \leq z \leq 1.0$), whose morphologies were classified classified in the Galaxy Zoo: Hubble project, using images from the HST-Legacy surveys. One of the key assumptions in the local-Universe debiasing techniques outlined in this chapter was that no significant morphological evolution exists in that redshift range. This is not a valid assumption for high-redshift galaxies, which are known to exhibit very different morphological populations at earlier epochs. A new debiasing technique was thus developed for the GZH data catalogue, using classifications from artificially-redshifted galaxies to quantify the effect of the redshift bias. The next Chapter will describe the creation and implementation of the simulated data set into the debiasing method applicable for high-redshift galaxies.

Chapter 3

FERENGI: debiasing beyond the local Universe

Portions of this chapter has been published in the Montly Notices of the Royal Astronomical Society with the following bibiliographic reference: Willett, K. W., Galloway, M. A., et al., 2015 ?

3.1 Intro

The GZ vote fraction f_{features} plays a crucial role in the majority of science cases that use Galaxy Zoo classifications. It represents the fraction of users who answered "feature or disk" to the first question in the decision tree, and is used to distinguish elliptical/spheroidal galaxies from those with features. Many studies aim to measure the popluation of galaxies exhibiting certain features such as bars (Masters et al., 2010, 2012; Melvin et al., 2014; Simmons et al., 2014; Cheung et al., 2015; Kruk et al., 2017), spiral arms (Willett et al., 2015; Hart et al., 2017), or bulges (Skibba et al., 2012; Simmons et al., 2012), among others. In each of these, f_{features} is necessary for creating the sample of galaxies which could potentially contain the feature in question. This is typically acheived by setting a cut, such that all galaxies with f_{features} greater than that threshold are considered to be candidates for that study.

While f_{features} is not a true probability, the measurement is intended to be consistent

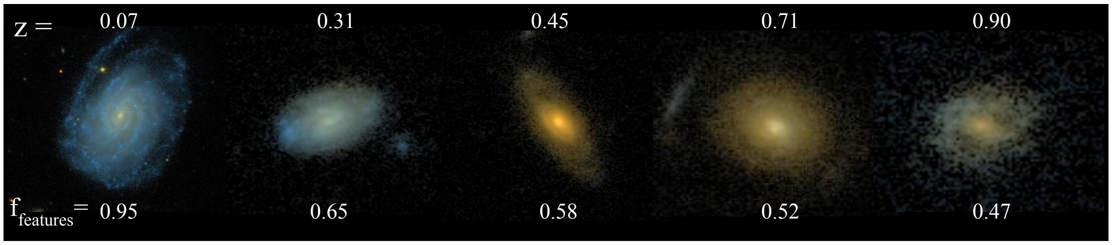

Figure 3.1 Example of the redshift-induced bias in f_{features}. Five images of disc galaxies from the GZH dataset are shown in order of increasing redshift, from left to right. Above each galaxy is its redshift and below is its f_{features} vote fraction. Although all galaxies appear to be discs with features, the vote fraction decreases steadily as redshift increases, as the details in each image become more difficult to distinguish.

among all galaxies; that is, two galaxies with similar f_{features} values should have similar likelihoods of being featured (or not featured). This has been shown to be true at low redshift by comparing the f_{features}values to expert classifications (Willett et al., 2013); there is a strong correlation between this vote fraction and whether the galaxy was expertly classified as a disk or an elliptical.

For distant galaxies, however, we observe that f_{features} is not consistant with nearby galaxies. As galaxies are observed at higher redshift, the images are inherently less resolved, and smaller features are more difficult to identify. This causes in a decrease in f_{features} than what would be expected if the galaxy had been observed at $z = 0$. Figure 3.1 shows this effect: although each of the five galaxies displayed appear to be discs with features, the fraction of users who identify the images in this way decreases with increasing redshift, as the finer features in each, while still present, become more difficult to resolve. Therefore, two intrinsically identical galaxies, but imaged at different redshifts, may have small to drastic differences in their f_{features} measurements. In order to keep f_{features} a value correlated with the likelihood of having features that is consistent for *all* galaxies, this bias must be corrected.

A method for correcting redshift bias in the GZ vote fractions was developed and implemented in early Galaxy Zoo projects GZ1 (Lintott et al., 2009) and GZ2 (Willett et al., 2013), which both contained nearby ($z < 0.2$) galaxies imaged by SDSS. A correction factor to the classification fractions measured at the higher redshifts was applied by matching the mean vote fractions of those at the lowest redshift. This technique was valid under the assumption that, within this redshift range, there would be no cosmological evolution of galaxies, and therefore any change in the mean vote fraction for any morphology with redshift was purely due to this observational bias, and not due to a genuine difference in morphological populations. For a full description, see Chapter 2.

In GZH, the redshift range is large enough that cosmological evolution of the morphologies of galaxies is expected, and therefore the previous method of correcting redshift-bias will not work. Instead, a new method was developed of measuring the change in f_{features} as a function of redshift using a set of simulated FERENGI images of galaxies, described in the next section. These images have been classified by volunteers in Galaxy Zoo in the same way as the GZH sample. This chapter will describe how a correction factor for f_{features} is measured using these data as a function of redshift at fixed surface brightness, and subsequently used to debias to the GZH sample.

3.1.1 The FERENGI code

The Full and Efficient Redshifting of Ensembles of Nearby Galaxy Images code (FERENGI, Barden et al. (2008)) is an IDL procedure that generates simulated images of nearby galaxies viewed at higher redshifts, taking into account cosmological effects such as surface brightness dimming and bandpass shifting. Artificially redshifted samples of galaxies, for which the intrinsic morphologies are already known from low-redshift observations, are useful for studying the imact these effects have on observed galaxy morphologies. For Galaxy Zoo, such images are particularly useful for measuring the effects of redshift on the volunteer classifications. Through classifications made on a set of artificially redshifted galaxies, any dependence they might have as a function of redshift can be measured, allowing a correction to be applied to classifications on images of real, high-redshift galaxies. The details of this type of debiasing technique will be described in Section 3.3. This section will first provide a breif summary of how the FERENGI code performs the artificial redshifting.

To create realistic images that mimic the seeing and resolution of HST ACS, the FERENGI redshifting procedure consists of three primary steps (explained in detail in Barden et al. (2008), but here a simplified outline):

i: Modify angular size and surface brightness

FERENGI first rescales the input image by computing the angular size transformation of the galaxy from its input redshift z_i to output reshift z_o. The angular size a of a distant object is proportional to $a \propto d/(1+z)^2$ (using $\tan(a)=a$ for small angles), where d is the luminosity distance to the object. In units of pixels, the transformation from input angular size n_i to output n_o can be expressed as:

$$\frac{n_o}{n_i} = \frac{d_i/(1+z_i)^2}{d_o/(1+z_o)^2}\frac{p_i}{p_o} \tag{3.1}$$

with an input pixel scale p_i (in this thesis $p_i = 0.396''$/pix corresponding to SDSS) and p_o (0.03"/pix, corresponding to ACS). From here a transformation between the observed fluxes is computed, assuming the absolute magnitude is conserved at both redshifts.

FERENGI also offers an option to apply an evolutionary correction to the absolute magnitude, which is helpful for a fair comparison of real and artificial high redshift morphologies. Artificially redshifted galaxies will appear much dimmer than their low redshift counterparts if absolute magnitude is conserved. Since galaxies intrinsically tend to be brighter at high redshift, visual classification of real galaxies cannot be compared as accurately to dimmer, simulated galaxies. To brighten galaxies in a similar way to real galaxies, a magnitude correction e can be input using a linear function:

$$M_{evo} = e \times z + M \tag{3.2}$$

where e represents the magnitude difference between two redshifts separated by $\Delta z = 1$.

ii: Account for bandpass shifting

As a consequence of cosmological expansion, the flux from a source measured using a broadband filter will not, in general, perfectly correspond to the rest-frame flux emitted at the target wavelength range of the filter. Rather, since observed wavelengths are redder than emitted wavelengths as a function of redshift ($\lambda_{obs} = \lambda_{rest-frame}(1+z)$), filters will tend to pick up light that is bluer (in the galaxy's rest-frame) than its target wavelength; this effect is known as *bandpass shifting*. In order to produce fluxes that mimic those measured by ACS at high redshifts, FERENGI simulates the bandpass shifting effects by applying a correction to the output flux calculated via the IDL routine KCORRECT, which incorporates spectral template models from Bruzual & Charlot (2003), to measure the expected shifts in flux for a given output filter.

iii: Point Spread Function and noise

In order to best mimic the HST ACS resolution, the image is then convolved with a PSF created to be as close as possible in shape and width to the ACS PSF. This is done by deconvolving a typical ACS PSF with the input SDSS PSF for each galaxy. This technique works well in general but has limitations - mainly, the widths of the in- and output PSFs must be sufficiently different. If they are comparable, the convolving function can become too narrow. In these cases, the image will be introduced to noise which results in ringing patterns and other oddities (examples of images with this effect are shown in Section 3.4.1). Since the difference in PSF widths increases with redshift, this imposes a minimum redshift at which FERENGI can successfuly create images for any given galaxy (discussed more in Section 3.2). Last, Poissonian noise is added to each pixel.

3.2 The FERENGI sample

To generate an artificially redshifted sample of galaxies to be used in debiasing the Galaxy Zoo: Hubble catalog, a source sample was generated [1] consisting of 288 galaxies from SDSS, all of which were previously classified in GZ2. These galaxies were chosen to span a wide range of morphologies, surface brightnesses, and redshifts. Seven morphological classes were considered: spiral galaxies, edge-on disks without a bulge, edge-on disks with a bulge, face-on disks with a bulge, galaxies with any features, galaxies undergoing mergers, and barred galaxies. For each of these categories, galaxies were chosen with from three "strength" bins, defined using the GZ2 vote fractions. Weak strengths were defined as having $f_{class} < 0.2$, intermediate as $0.2 < f_{class} < 0.8$, and strong as $f_{class} > 0.8$. In each strength bin, galaxies were also chosen to represent three different surface brightnesses: $\mu_r > 21.5$, $20.5 < \mu_r < 21.5$, and $\mu_r < 20.5$. Finally, from each morphological class, strength, and surface brightness bin, one galaxy was chosen for four redshift bins: $z < 0.013$, $0.013 < z < 0.02$, $0.02 < z < 0.025$, and $z > 0.025$,

[1] The source sample for FERENGI was created by the Galaxy Zoo science team in 2012.

with the exception of the bar class, in which two galaxies were chosen for each redshift bin, doubling the sample size for that class.

The 288 SDSS galaxies were processed with the FERENGI code to mimic *HST* imaging parameters [2] , in order to ultimately measure and correct any redshift-dependant biases in the classifications of the real *HST* images. I-814 and V-606 images, chosen to match the *HST* ACS AEGIS imaging, were output for each subject at a range of redshifts and with a range of applied evolution factors. The range of simulated redshifts possible for any galaxy is dependent on the intrinsic redshift and size of the source galaxy, since the simulated images cannot be resampled at better angular resolution than the original SDSS data. This imposes a minimum simulated "target" redshift that can be achieved for each galaxy. For the lowest redshift bin in the source sample ($z < 0.013$), galaxies could be redshifted the full range of $0.3 < z < 1.0$, in increments of $dz = 0.1$. For the second lowest redshift bin, galaxies could only be redshifted in the range $0.5 < z < 1.0$, for the third, galaxies could be redshifted in the range $0.8 < z < 1.0$, and for the highest redshift bin, galaxies were only redshifted in FERENGI to $z = 1.0$. Only galaxies which were redshifted the full range were considered in the debiasing procedure outlined in the next section (3.3.1), because the method calibrates galaxies to a low redshift of $z = 0.3$, data for which is not available for galaxies in the remaining three redshift bins. Last, for each simulated redshift, a range of evolution factors was applied from $0 < e < 3$ in increments of $de = 0.5$.

The final FERENGI sample totals 6,624 simulated images which were classified as part of GZ4, using the same decision tree as used in GZH. The debiasing technique described next (Section 3.3) used only the 4,446 images corresponding to the 72 galaxies which were redshifted the full $0.3 < z < 1.0$ range. Because the debiasing method takes into account surface brightness as a parameter, photometry was measured for all images using SEXTRACTOR [3] . The mean surface brighness μ within effective radius (R_e) was calculated as:

$$\mu = m + 2.5 * \log_{10}(2 \times (b/a) \times \pi R_e^2) \tag{3.3}$$

[2] This work was done by Edmond Cheung, a Galaxy Zoo science team member.

[3] SEXTRACTOR measurements for the original FERENGI sample were done by Tom Melvin, a former Galaxy Zoo science team member.

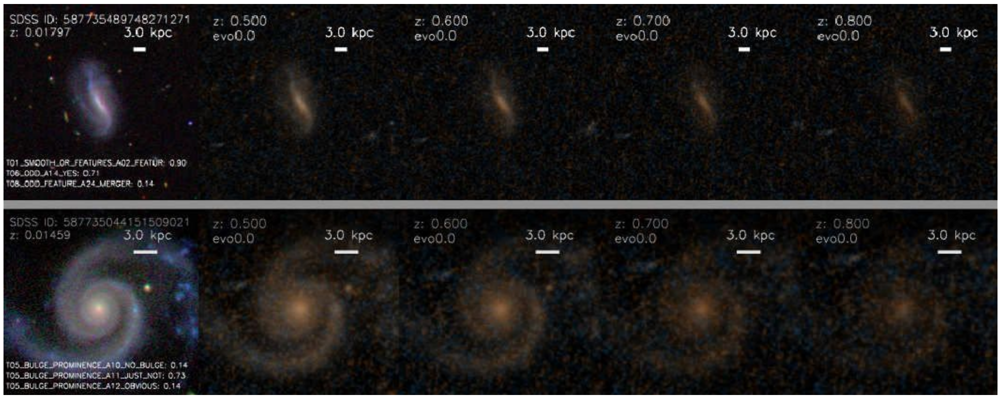

Figure 3.2 Examples of two SDSS galaxies which have been run through the FERENGI code to produce simulated *HST* images. The measured value of f_{features} from GZH for the images in each panel are (1) Top row: $f_{\text{features}} = (0.900, 0.625, 0.350, 0.350, 0.225)$ and (2) Bottom row: $f_{\text{features}} = (1.000, 0.875, 0.875, 0.625, 0.375)$.

where m is `MAG_AUTO` in the I_{814W} band, (b/a) is the galaxy ellipticity (the profile RMS along the semi-major and -minor axes), and R_e is the 50% `FLUX_RADIUS` converted into arcsec.

3.3 Measuring the dependence z and μ on f_{features} using the FERENGI classifications

3.3.1 Identifying "correctable" and "lower limit" samples.

The objective is to use the simulated data from FERENGI to predict, for a galaxy imaged at a redshift z, and with a measured $f_{\text{features},z}$ value, what its f_{features} value *would have been* if it had been viewed at $z = 0.3$. This predicted value is defined as the "debiased' vote fraction $f_{\text{features,debiased}}$, and is calculated by applying a correction to the measured value of f_{features}.

The amount that a galaxy's f_{features} vote fraction must be corrected is assumed to primarily depend on the apparent size and brightness of the galaxy. As described in 3.1, these factors will affect the overall clarity of the image viewed by the GZ volunteers, which in turn affects the likelihood of being able to identify distinct feature. The apparent size and brightness are controlled by both instrinsic parameters (absolute size and luminosity), and extrinsic (distance to the galaxy). The change in f_{features} then is measured as a function of redshift (z, an extrinsic freature, measuring distance to the galaxy), and surface brightness (μ, an intrinsic feature, taking into account both brightness and size).

Figure 3.3 shows the change in f_{features} for FERENGI galaxies in bins of redshift and surface brightness. Points in each z, μ represent individual FERENGI galaxies. On the x-axis of each bin is the value of f_{features} measured in that galaxy's $z = 0.3$ image (the lowest redshift of the simulated images). On the y-axis of each bin is the value of f_{features} measured in that galaxy's $z = z$ image, where z corresponds to the redshift associated with that bin. As predicted, the value of f_{features} measured at a higher redshift, z, is, in general, *lower* than the value measured at lower redshift, $z = 0.3$, *for the same galaxy.* This effect is strongest as redshift increases (to the right in Figure 3.3) and as surface brightness decreases (upwards in Figure 3.3).

A reliable predicted value can be obtained so long as the relationship between $f_{\text{features},z}$ and $f_{\text{features},z=0.3}$ is single-valued; that is, for a given $f_{\text{features},z}$, there is exactly one corresponding value of f_{features} at $z = 0.3$. Unfortunately, this is *not* always the case. Figure 3.4 shows f_{features} measured at $z = 1$ vs f_{features} measured at $z = 0.3$ for FERENGI galaxies with average surface brightnesses $< \mu >= 20.8$ (a zoomed-in version of the dark outlined bin in Figure 3.3). This figure shows that if the value of f_{features} measured for a galaxy at $z = 1$ is particularly low, there is a wide range that f_{features} could have been if measured at $z = 0.3$. Therefore, a low measured value of f_{features} at high redshift could represent two morphological types of galaxies: 1) The galaxy has no distinguishable features and may be classified as a smooth elliptical, or 2) the galaxy *does* have features, but these have become blurred and too difficult to detect at high redshift.

It is important to identify such regions of surface brightness/redshift/f_{features} space since vote fractions cannot be confidentely corrected to a single value for galaxies in these regions. The criteria for determining whether a region of this space is single-valued, and therefore correctable, is as follows: In each surface brightness and redshift bin, the relationship between $f_{\text{features},z}$ and $f_{\text{features},z=0.3}$ is modelled by fitting the data with polynomials of degress n=3,2, and 1, and using the best formal fit out of the three as measured by the sum of the residuals. These fits are shown as the dashed black

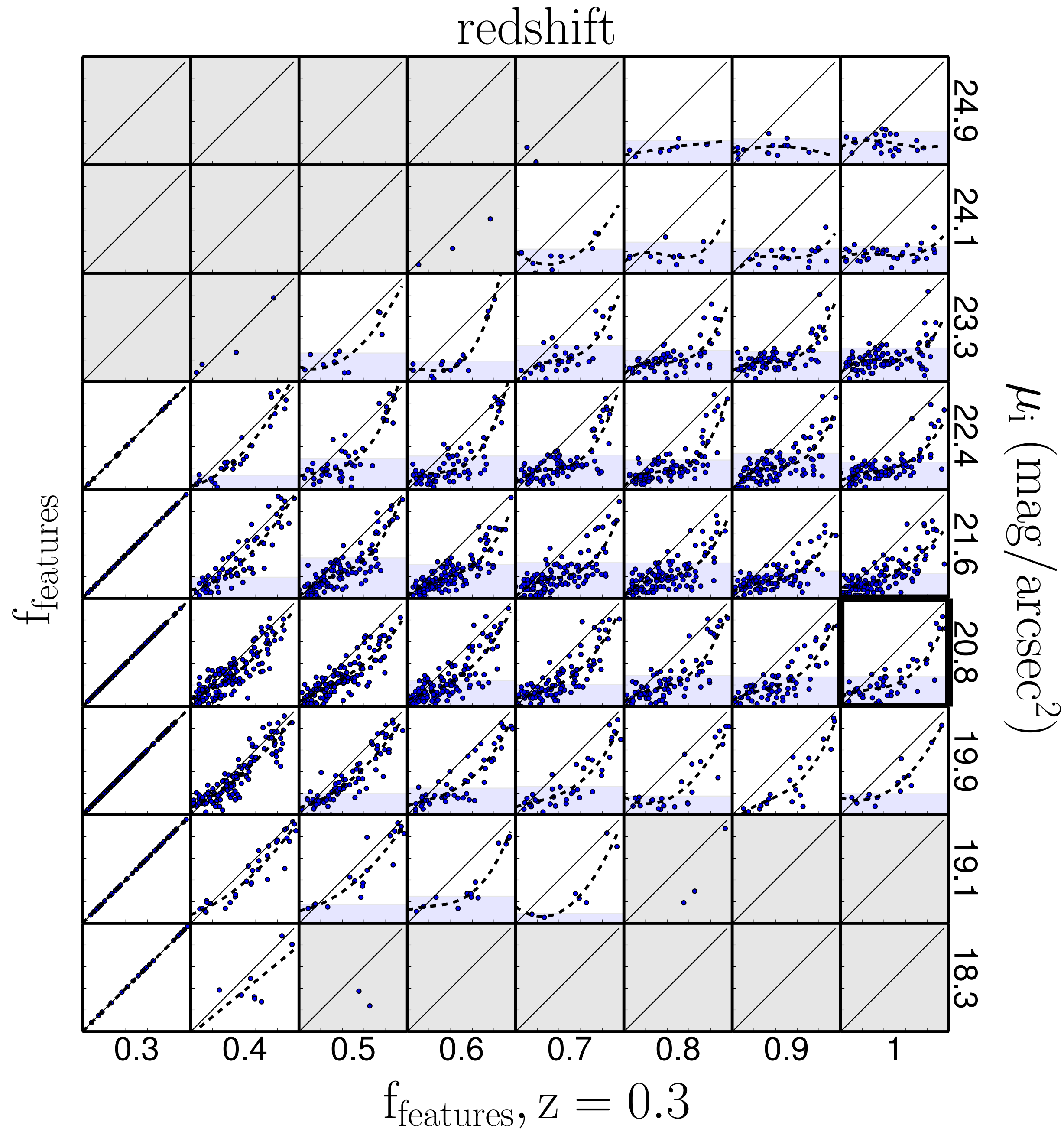

Figure 3.3 Effects of redshift bias in 3,449 images in the FERENGI sample. Each point *in a given redshift and surface brightness bin* represents a unique galaxy. On the y-axis in each bin is the f_{features} value of the image of that galaxy redshifted to the value corresponding to that redshift bin. On the x-axis is the f_{features} value of the image of the same galaxy redshifted to $z = 0.3$. The dashed black lines represent the best-fit polynomials to the data in each square. The solid black line represents $f_{\text{features},z}$=$f_{\text{features},z=0.3}$. Regions in which there is a single-valued relationship between f_{features} at high redshift and at $z = 0.3$ are white; those in which there is not are blue, and those with not enough data ($N < 5$) are grey. A larger version of the bin outlined at $z = 1.0$ and $20.3 < \mu < 21.0$ (mag/arcsec^2) is shown in Figure 3.4.

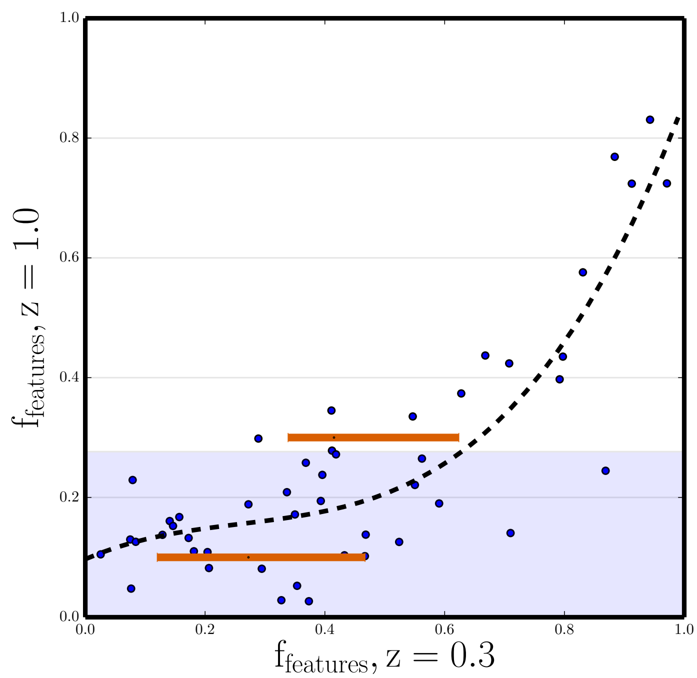

Figure 3.4 A larger version of the dark-outlined square in Figure 3.3, containing FERENGI galaxies that have been artificially redshifted to $z = 1.0$ and have surface brightnesses between $20.3 < \mu < 21.0$ (mag/arcsec^2). The orange bars represent the inner 68% (1σ) of the uncorrectable f_{features} quantiles, which are used to compute the limits on the range of debiased values.

lines in Figures 3.3 and 3.4. Flat regions of the bins are areas in which there is *not* a clear single-valued relationship between $f_{\text{features},z}$ and $f_{\text{features},z=0.3}$. This is quantified by measuring the slope of the best-fit polynomial to the vote fractions; regions of the bins with a slope less than 0.4 are considered *not* one-to-one, and therefore $f_{\text{features},z}$ cannot be boosted to its $f_{\text{features},z=0.3}$ value. These are colored blue in Figure 3.3 and are referred to as the *lower limit* sample, because the most stringent correction available is that the weighted f_{features} is a lower limit to the true value.

Correctable and lower-limit regions of $z - \mu$ space can only be identified in bins where there exists a sufficient number of FERENGI galaxies to model a polynomial. Bins with fewer than 5 points were not considered sufficiently populated to derive a relationship, and are represented by the gray shaded bins in Figure 3.3. Galaxies in the GZH sample whose z, μ did not correspond to unshaded regions shown in the Figure were assigned to the "not enough information," or "NEI" sample, because there were not enough FERENGI galaxies to quantify the bias in f_{features} in that parameter space. Figure 3.5 displays the overlap of z, μ bivariate distributions of the GZH and FERENGI samples. Ideally, the FERENGI space would overlap the GZH parameter space as close as possible. However, the unfortunate consequence of the simulated set being derived from galaxies in the local Universe puts an upper limit on the maximum surface brightness achievable for the FERENGI set. The earlier Universe simply has many more galaxies at the high surface brightness end, which were reproduced as best as possible by applying the magnitude correction, but ultimately can only result in a distribution that spans, but not completely reproduces, the bivariate distribution of the real data. The mismatch should not affect the overall calibration accuracy of the debiasing method, since only galaxies in particular $z - \mu$ bins are being corrected. It was stressed in the data release (Willett et al., 2016) however that due to this limitation in parameter space, all corrected values should be used with caution when using them for population studies.

The unshaded regions of Figure3.4 thus define descrete ranges of redshift, surface brightness, and f_{features} within which a galaxy must lie in order for the debiased vote fraction to be confidentely applied. While the appropriate correctable regions were defined as discrete bins, the true correctable region is assumed to be a smooth function of z, μ, and f_{features}. To define this smooth space, a convex hull was calculated to enclose the correctable and lower-limit FERENGI galaxies in the $z - \mu - f_{\text{features}}$ space

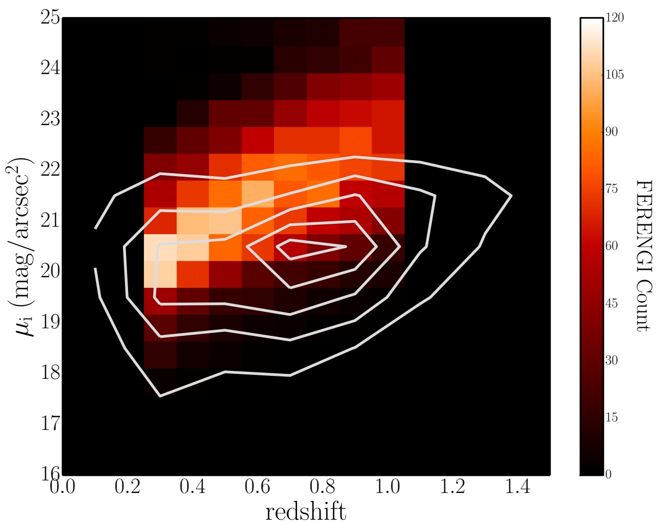

Figure 3.5 Surface brightness as a function of redshift for 3,449 FERENGI images and the 102,548 `main` galaxies with measured μ and z values. The colour histogram shows the number of FERENGI images as a function of μ and z_{sim}. White contours show counts for the galaxies in the `main` sample, with the outermost contour starting at $N = 1500$ and separated by intervals of 1500.

Table 3.1 Number of correctable galaxies for the top-level task in GZH, split by *HST* survey.

	Correction type	AEGIS	COSMOS	GEMS	GOODS-N 5-epoch	GOODS-S 5-epoch	Total
correctable	0	2,908	21,169	2,802	1,459	1,189	29,527
lower-limit	1	833	5,169	1,021	1,377	1,267	9,667
$z \leq 0.3$	2	955	10,870	1,175	415	400	13,815
NEI	3	2,677	43,058	3,559	2,077	2,184	53,555
no z info	4	1,134	4,688	530	687	102	7,141
total		8,507	84,954	9,087	6,015	5,142	113,705

(see Figure 3.6). The space defined by this hull was used to ultimately separate the GZH galaxies into correctable samples (those for which a correction to f_{features} can confidentely be applied, see next section) and lower-limit samples (those for which a single-valued correction cannot be applied). The final categorization of the GZH sample, split by imaging survey, is shown in Table 3.1.

For the "lower limit" galaxies, since a single debiased f_{features} value cannot be confidentely assigned, a *range* of debiased values is estimated. In each z, μ bin in Figure 3.3, the spread of intrinsic values of $f_{\mathrm{features},z=0.3}$ for five quantiles of observed f_{features} is computed - these are denoted by the gray lines in the close-up Figure 3.4. The range of intrinsic values of f_{features} is defined by the upper and lower 1 σ limits, enclosing the inner 68% of the data; this is represented by the orange bars in Figure 3.4. For any galaxy which cannot be directly debiased, these ranges are used to denote the upper and lower limits on the expected values $f_{\mathrm{features},z=0.3}$ as a function of the observed f_{features}.

3.3.2 The ζ equation

For the "correctable" sample of simulated FERENGI galaxies, an equation was derived to model the dropoff in f_{features} with redshift for each galaxy. Such a model is assumed to have the following criteria: (1) For a given galaxy, f_{features} should decrease relative to its $f_{\mathrm{features},z=0.3}$ as redshift increases. (2) The corrected f_{features} value must be contained within 0 and 1, since it is a fraction. (3) The degree of dropoff may depend on the surface brightness of the galaxy. Given these three assumptions, a simple exponential

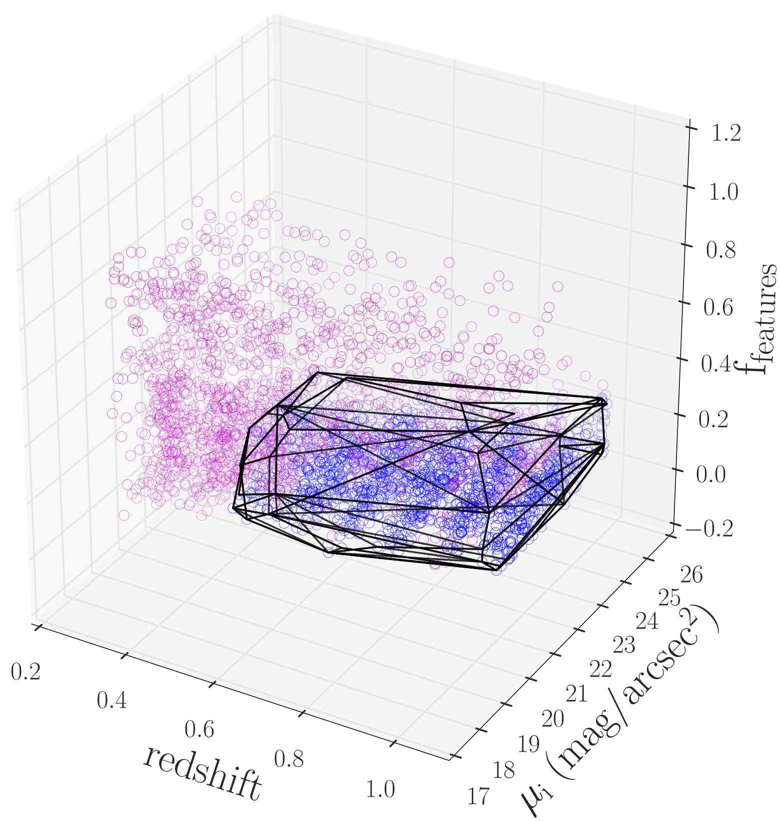

Figure 3.6 The final separation of the correctable and lower-limit samples in redshift/surface brightness/f_{features} space.**Pink** points are all FERENGI galaxies in the **unshaded** regions of Figure 3.3. **Blue** points are all FERENGI galaxies in the **blue shaded** regions of Figure 3.3. The solid black line is the convex hull which encloses the uncorrectable points and defines the region of the lower-limit sample.

function was derived:

$$f_{\mu,z} = 1 - (1 - f_{\mu,z=0.3})e^{\frac{z-z_0}{\zeta}} \tag{3.4}$$

where $f_{\mu,z=0.3}$ is the vote fraction at the lowest redshift in the artificially-redshifted FERENGI sample ($z_0 = 0.3$). ζ is a parameter that controls the rate at which f_{features} decreases with redshift.

Equation 3.4 was then fit to each galaxy in the "correctable" FERENGI sample, and ζ is measured for each. Figure 3.7 shows the best fit equations for 16 galaxies, and the ζ corresponding to the best fit is displayed with each galaxy. As it was assumed that surface brightness likely plays a role in the level of dropoff in f_{features}, and hence the value of ζ which controls this dropoff, it is assumed that ζ follows a simple linear dependence with surface brightness:

$$\log_{10}(\hat{\zeta}) = \zeta_0 + (\zeta_1 \times \mu), \tag{3.5}$$

where $\hat{\zeta}$ is the correction factor applied to each galaxy. Figure 3.8 shows the relationship between the derived ζ values and the surface brightness μ of the FERENGI galaxies, which is fit with equation 3.5. The best-fit parameters to this linear fit from least-squares optimization are $\zeta_0 = 0.50$, $\zeta_1 = -0.03$. Interestingly, only a very weak surface brightness dependence is detected. It is difficult to determine from these data whether the weak detection is due to a true lack of dependence, or insufficient data (only 28 galaxies had sufficient data to accurately measure ζ).

Using the ζ parameters measured in the FERENGI sample, a final debiased correction equation is derived to correct the f_{features} vote fractions in the HST data:

$$f_{\mathrm{features,debiased}} = 1 - (1 - f_{\mathrm{features,weighted}})e^{\frac{-(z-z_0)}{\hat{\zeta}}} \tag{3.6}$$

where $f_{\mathrm{features,weighted}}$ is the weighted vote fraction, and $f_{\mathrm{features,debiased}}$ is bounded between $f_{\mathrm{features,weighted}}$ and 1.

3.3.3 Debiasing results and limitations of the ferengi simulated data

Figure 3.9 shows the results of the ζ correction for the correctable sample. Plotted on the left panel is the corrected ($\hat{f}_{features}$) vs the raw (f_{features}) fractions. Galaxies with

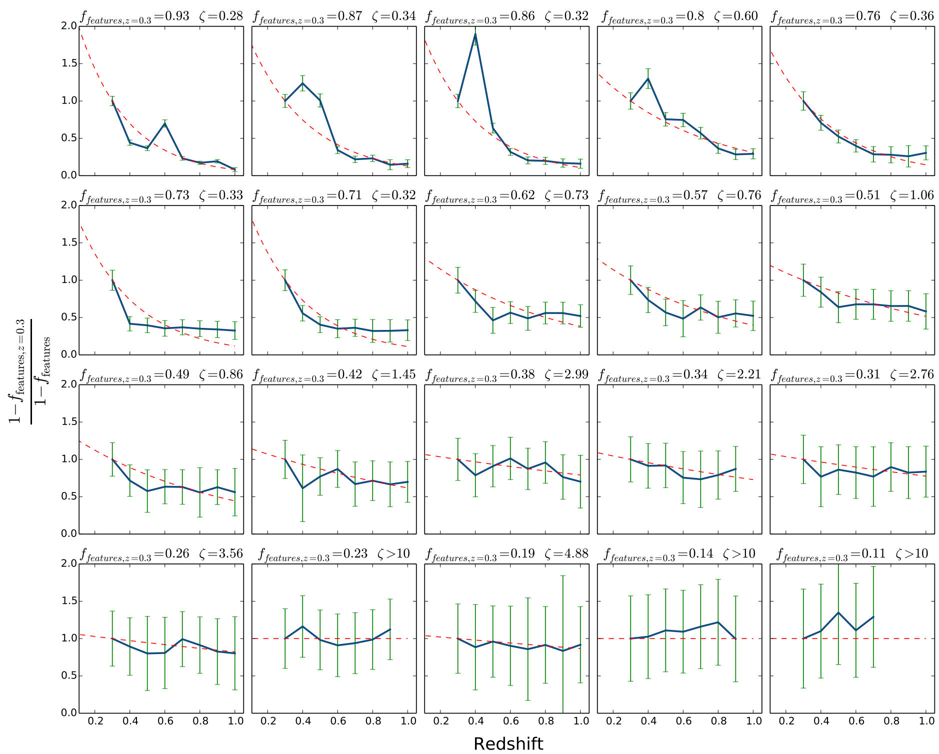

Figure 3.7 Behavior of the normalised, weighted vote fractions of features visible in a galaxy (f_{features}) as a function of redshift in the artificial FERENGI images. Galaxies in this plot were randomly selected from a distribution with evolutionary correction $e = 0$ and at least three detectable images in redshift bins of $z \geq 0.3$. The displayed bins are sorted by $f_{\mathrm{features},z=0.3}$, labeled above each plot. Measured vote fractions (blue solid line) are fit with an exponential function (red dashed line; Equation 3.4); the best-fit parameter for ζ is given above each plot.

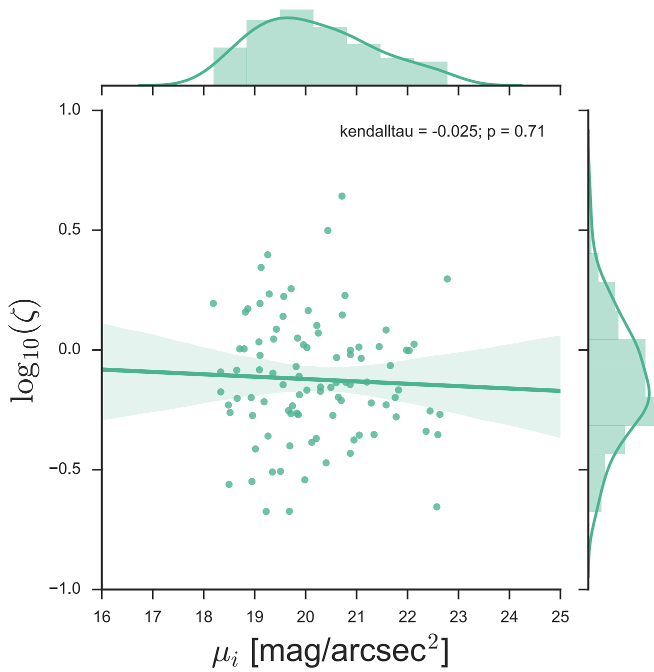

Figure 3.8 All fits for the FERENGI galaxies of the vote fraction dropoff parameter ζ for f_{features} as a function of surface brightness. This includes only the simulated galaxies with a bounded range on the dropoff ($-10 < \zeta < 10$) and sufficient points to fit each function (28 original galaxies, each with varying images artificially redshifted in one to eight bins over a range from $0.3 \lesssim z_{\text{sim}} \lesssim 1.0$).

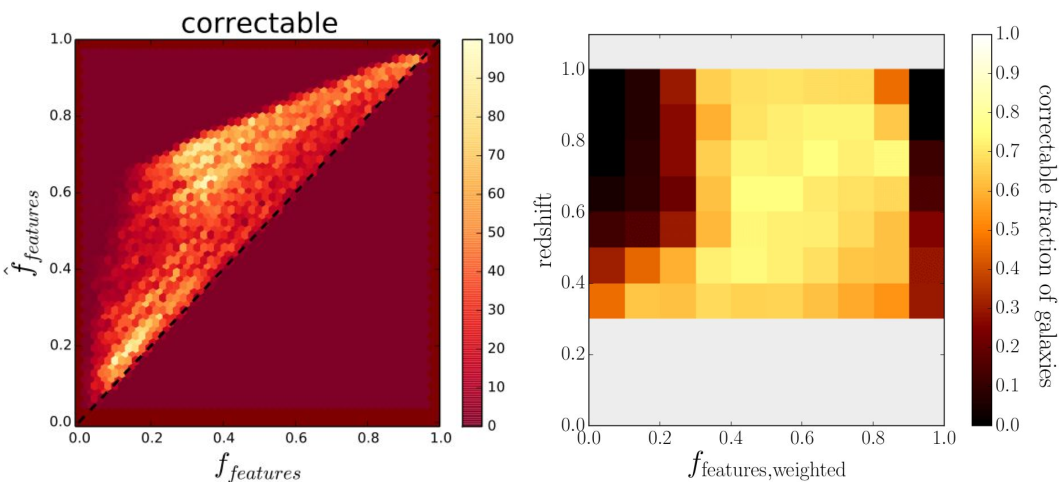

Figure 3.9 **Left**: Debiased vs raw vote fractions for the GZH correctable sample. **Right**: Histogram showing the fraction of galaxies that have a finite correction for the debiased vote fractions $f_{\mathrm{features,debiased}}$ as a function of f_{features} and redshift. The parameter space for corrections is limited to $0.3 \leq z \leq 1.0$ due to the sampling of the parent SDSS galaxies and detectability in the FERENGI images.

low ($f_{features} < 0.2$) may be corrected to as high as ~ 0.6, while fractions already large require no additional boost. Using the corrected values will aid in the identification of featured galaxies in future studies. The limitations of the process can be seen in the right panel of the figure. Displayed is the fraction of galaxies in the correctable sample as a function of redshift and initial f_{features}. At the low end of f_{features}, only galaxies also with low redshifts tend to be a part of the sample; this is due to the effect desribed above wherein the low resolution of the high-redshift images reaching a point where smooth-appearing featured galaxies are completely indiscernable from ellipticals, and it is not possible to be certain that a boost is necessary. This limitation is unavoidable given the limited sensitivity of any instrument, however this effect will be lessened as imaging technology continues to improve.

The FERENGI sample was successful in identifying and correcting the vote fractions of the GZH sample to aid in identifying featured galaxies, albeit with several limitations. Inspired by the utility of the simulated galaxy classifications, a second set was created for a very specific purpose of measuring the incompleteness in disk *fraction* (as opposed to incompleteness in individual vote fractions). The second half of this Chapter will explain the motivations behind and the generation of this second simulated set.

3.4 Ferengi 2: using simulated images to measure incompleteness in disk fraction

In the previous section I described how we used the simulted FERENGI images to measure the redshift/surface brightness dependence on f_{features}, and applied the measurements towards a correction factor to the vote fractions directly. In this section I will describe the motivation, selection, and application of a second set of FERENGI images used to measure and correct for the incompleteness in *number* of disks detected as a function of redshift and surface brightness, used in the work described in Chapter 6.

3.4.1 The Ferengi 2 Sample

The creation of a second set of FERENGI images was motivated by the scientific goal of measuring the redshift evolution of the fraction of red disk galaxies using the Galaxy Zoo: Hubble dataset. This project is described in full in Chapter 6, but the reasons requiring a new set of simulated images will be described briefly here. First, as described in the previous section, the analysis of the first FERENGI set revealed that, for a large area of z-μ parameter space, galaxies with low measured values of f_{features} could not be corrected to a point that could clearly distingush them as disks with washed-out features or ellipticals. Due to this limitation, any measurement of the number of disk galaxies in a given redshift interval can only be reported as a *lower-limit* to the true value. The difference in the measured lower-limit and the true number of disks is what we will refer to as the *incompleteness* in number of disks detected.

It is possible, then, to use the FERENGI images to measure this incompleteness by measuring the number of disks detected at a given redshift, and comparing to the number of disks detected out of the same galaxies at the lowest redshift (this would be considred the true, or intrinsic, number of disks.) The details of this approach will be described in the next section. A complication specific to this project is that the number of disks will be ultimitely used to compute the *red disk fraction*, that is, the ratio of the number of red disks to all disks, as a function of redshift. It is then necessary to measure the level of incompleteness for both red and blue galaxies separately, to calculate this fraction most accurately.

The color separation method for the *HST* galaxies in Chapter 6 uses NUV, r, and J magnitudes. To separate the FERENGI sample of galaxies into red and blue samples in the same way, these magnitudes are required. In the first set, however, only 44 of the 288 galaxies had these data available, which were not enough to properly measure any incompleteness, especially after binning the data further in surface brightness and redshift. So, a larger set of galaxies to be artificially redshifted, all which had the aforementioned data necessary to separate by color, was required.

This set of new galaxies to be put through the FERENGI code, hereafter refered to as the FERENGI 2 sample, was selected as follows: All candidates were pulled from a parent sample of all SDSS galaxies which had previously been classified in GZ2. As discussed in Section 3.2, only galaxies with redshifts below $z < 0.013$ were able to be redshifted the full simulated redshift range $0.3 < z < 1.0$, so a redshift cut was implemented of $z < 0.013$. These galaxies were cross-matched with catalogs from GALEX (Martin et al., 2005) for NUV magnitudes and 2MASS (Skrutskie et al., 2006) for J magnitudes. 1,435 galaxies fit these criteria.

Bulk SDSS u, g, r, i, and z-band fits images were then downloaded for all 1,435 galaxy candidates [4] . Cutouts were made for each galaxy, using the 90% r-band petrosian radius to set the size of the cutout (PETROR90_R). The default prescription used was to define the edges as 2.5*PETROR90_R, measured from the galaxy as the center. If the galaxy was within this distance from the edge of the bulk fits image, 2.0*PETROR90_R was used. Cutouts were not made for galaxies within this distance from the edge, both to ensure the full galaxy was visible in all cutouts in the sample, and to avoid over-zooming the image. 187 galaxies were thus removed from FERENGI2; an example of such a galaxy "too close" to the edge of the edge is shown in Figure 3.10.

While all 78 $z < 0.013$ galaxies from the original FERENGI sample were successfuly simulated to a minimum redshift of $z_{sim} = 0.3$, this was not always true for the FERENGI2 candidates. Redshift of the source galaxy is the largest factor in determining the minimum possible simulated redshift, but other factors including the size of the psf and physical size of the source galaxy also come into play. All 1,248 candidates were then

[4] http://data.sdss3.org/bulkFields

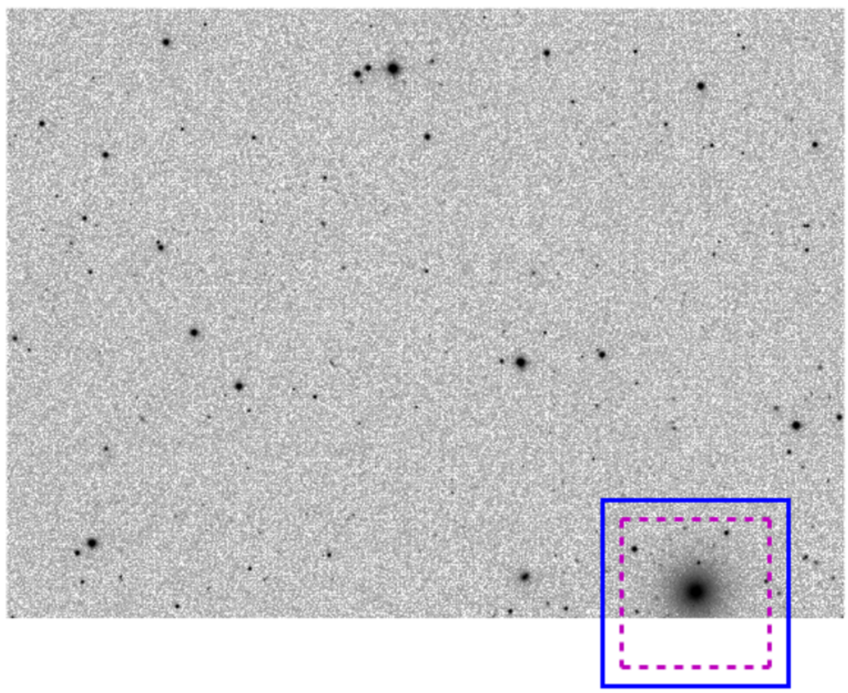

Figure 3.10 Example of a galaxy overlapping the edge of the SDSS frame. Shown is the bulk r-band fits image for SDSS DR12 run 3903, camcol 6, and field 60. The boxed-in galaxy (SDSS DR12 objid 1237662239079268544) is too close to the edge of the image to create a cutout that encloses the entire galaxy. The pink dashed box indicates a cutout size of 2*PETROR90_R, the blue solid line indicates a cutout size of 2.5*PETROR90_R.

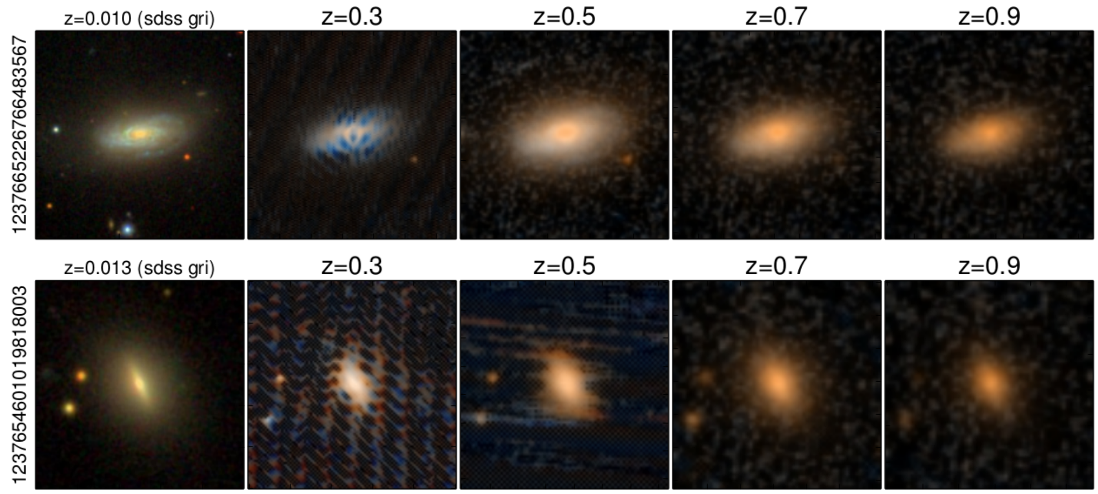

Figure 3.11 Examples of two galaxies whose minimum simulated redshifts in FERENGI were larger than $z_{sim} = 0.3$. These were detected via visual inspection and removed from the final FERENGI2 sample.

put through FERENGI at only the lowest redshift $z_{sim} = 0.3$ to begin, and each image was visualy inspected to determine whether the code succeeded. 312 "failures" were detected; two examples are shown in Figure 3.11. The remaining 936 "successes" were then artificially redshift the full range of $0.3 < z < 1.0$ in increments of $dz = 0.1$; these make up the final FERENGI2 sample of 7,488 images of 936 galaxies redshifted 8 times. A single evolution factor, rather than a range, of $e = 1$ was applied to all images. This value was chosen by analyzing the spectra template models of Brinchmann et al. (2004), which showed that the most typical galaxies evolve in brightness by one magnitude per redshift. Example images are shown in Figure 3.12

The 7,488 FERENGI2 images were then put into Galaxy Zoo for classification on December 11, 2016. The images were shown at a probability rate of 1/3, while the other 2/3 shown were images from Illustris or SDSS. Given these occurance frequencies and classification rates at the time, it was expected that the sample would require 4 months to be fully classified (that is, each image would be seen by 40 users). In an attempt to reduce this time, the Galaxy Zoo team launched a "Save Mel's Thesis" campaign, whereby details on the project and a request for help were sent to volunteers

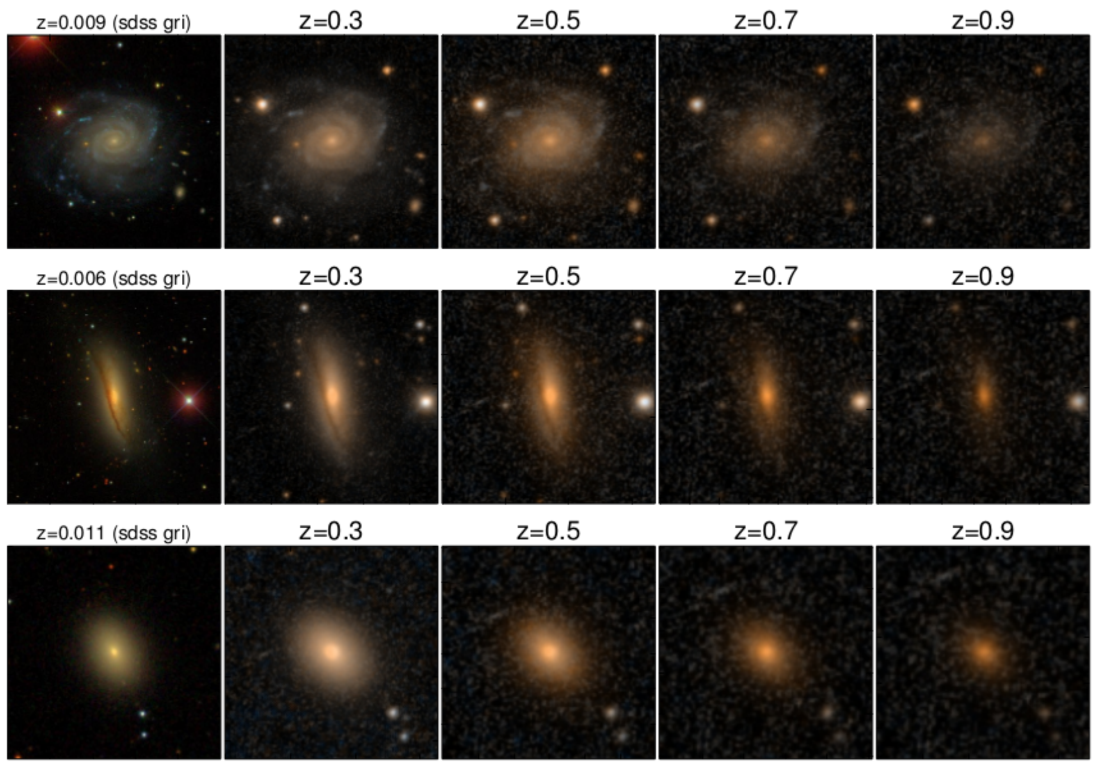

Figure 3.12 Examples of FERENGI2 galaxies. The left is the original gri-composite image of the source galaxy. Images on the right are simulated output from the FERENGI code. Only four of the eight simulated redshifts are shown in the interest of space.

via an e-mail Newsletter, blog post [5] , and a Daily Zooniverse post which was shared on social media websites Facebook and Twitter. The campaign proved effective, cutting the predicted classification time in half. Future work is needed to explore the details behind the effect of such a campaign and classification rates, which could potenitally aid other time-sensitive projects.

Following the completion of the FERENGI2 classifications, the votes were counted and weighted in the method described in Chapter 2. The technique used to measure the incompleteness in disk fraction using this set is described in Chapter 6.

[5] https://blog.galaxyzoo.org/2016/12/12/ferengi-2-images-launched/

Chapter 4

The effect of bar-driven fueling on the presence of an active galactic nucleus

This chapter has been published in the Monthly Notices of the Royal Astronomical Society with the following bibiliographic reference: Galloway, M.A., et al., 2015 ?

Supermassive black holes exist at the centres of most (if not all) massive galaxies (Kormendy & Richstone, 1995; Richstone et al., 1998; Kormendy & Gebhardt, 2001; Ghez et al., 2008). The evolution of the black hole is closely tied to that of the host galaxy; hence, understanding the conditions that drive black hole growth is key for a complete picture of galactic evolution. While most black holes are not actively growing, a small fraction are observed to accrete matter and cause the surrounding material to emit powerful pan-chromatic radiation. The central region of a galaxy which encompasses these “active” black holes, along with the surrounding accretion disk and ionized gas clouds, is an active galactic nucleus (AGN). Since the bolometric luminosity of the AGN can be comparable to (or greater than) the integrated stellar luminosity (as high as $L \sim 10^{47}$ erg s^{-1}) the black holes have an important effect on the host galaxy, controlling the amount of star formation via AGN feedback, as well as contributing toward the net reionization of the intergalactic medium (Heckman & Best, 2014). Understanding the fueling mechanism(s) for AGN is thus critical for studying galaxies, both in the nearby Universe and at higher redshifts.

The precise physics that govern the relationship between AGN and their host galaxies is an area of intense study. This includes the AGN fueling mechanism — while there is strong evidence that there is sufficient gas in the ISM to keep the accretion disc supplied with enough material to radiate at typical bolometric AGN luminosities (Shlosman et al., 1989, 1990), the dynamical mechanisms that drive the gas within the black hole's sphere of influence are difficult to observe directly, especially at extragalactic distances. In order to initiate (or continue) AGN activity, gas must lose enough angular momentum in a short timeframe to reduce its orbit from scales of kiloparsecs down to parsecs. Shlosman et al. (1989) analytically showed that while gas can lose angular momentum due to turbulent viscous processes, these are too slow to be the only mechanism involved. Later N-body simulations have shown viscous torques on the gas are negligible and do not directly initiate inflows (Bournaud et al., 2005), further arguing for an additional method of radial gas transport.

One possibility is that the presence of a large-scale bar may supplement viscous torques and further drive AGN fueling. Bars efficiently transport angular momentum within the disc (Athanassoula, 2003; Kormendy & Kennicutt, 2004), and are ubiquitous features in disc galaxies in the local Universe (Eskridge et al., 2000; Laurikainen et al., 2004; MenendezDelmestre et al., 2007a; Masters et al., 2011; Cheung et al., 2013). Simulations (Athanassoula, 1992; Friedli & Benz, 1993; Ann & Thakur, 2005) show that stellar bars, whose lengths are on the order of kiloparsecs, do drive gas into the circumnuclear region (scales of 100 pc) of galaxies; observational studies have also shown an increase in the amount of central star formation for barred galaxies (Ellison et al., 2011). This combination of simple analytical models, simulations, and observations clearly points toward galactic bars preferentially driving gas to the centres of their galaxies. It is still an open question, though, whether this gas is ultimately driven to the central $1-10$ pc scales, which theoretical models suggest are required for accretion around the central black hole of the AGN.

Theoretical models for alternate modes to bar-driven fueling also exist. Numerical simulations from Hopkins & Quataert (2010) examine several possible mechanisms behind angular momentum transport for a range of galaxy morphologies (bars, spirals, rings, clumpy and irregular shapes, mergers) at different radial scales. For each morphological type, gas transported from larger to smaller (~ 1 kpc) radii “piles up” due to decreasing efficiency in the processes that induce torque. If this pile-up of gas is sufficiently massive, it becomes self-gravitating and can efficiently transport angular momentum down to scales of ~ 10 pc. This “stuff within stuff” model is similar to the second half of Shlosman et al. (1989)’s “bars within bars” model. The difference is that the “bars within bars” model assumes that a large-scale bar is the primary mechanism that transports the gas inward to form the gaseous disc, while Hopkins & Quataert (2010) show that many large-scale morphologies are capable of producing a secondary instability and fueling an AGN, suggesting that this process may not be restricted to classic large-scale bars. n Many studies have focused on observational correlations between the presence of a galactic bar (typically identified at optical wavelengths) and that of an AGN (identified by optical line ratios or widths). Some studies (eg, Ho et al., 1997; Mulchaey & Regan, 1997; Hunt & Malkan, 1999) find similar bar fractions for both AGN and inactive galaxies and hence report no correlation. The significance of these fractions, however, is hindered by small sample sizes, typically with fewer than 100 barred AGN hosts. More recent studies (Knapen et al., 2000; Laine et al., 2002; Laurikainen et al., 2004) report increases of $20-23\%$ in the bar fractions for AGN when compared to non-AGN hosts. Despite larger numbers of AGN, the results are still only significant at the 2.5σ level. Rather than comparing the likelihood of active and inactive galaxies to host bars, as is most common among previous studies, Cisternas et al. (2013) accounted for a continuum of values by quantifying bar strength and activity level in local X-ray identified AGN. While no correlation was found, these data probe only the low-luminosity AGN regime ($L_X \sim 4 \times 10^{38}$ erg s^{-1}). In the high redshift universe, Cheung et al. (2015) find no compelling evidence that bars are more likely to lie in AGN hosts than non-AGN hosts.

Several recent studies have focused on optical identifications of bars and AGN, primarily using data from the Sloan Digital Sky Survey (SDSS). We compare these methods and results in Table 4.1. Among these studies, neither Lee et al. (2012) nor Martini et al. (2003) find any correlation between the presence of strong galactic bars and AGN, but do not rule out the possibility of smaller, nuclear bars influencing AGN activity. In contrast, Oh et al. (2012); Hao et al. (2009); Alonso et al. (2013) all find evidence of bar effects in AGN — however, they disagree on both the strength of the effect and whether it affects both black hole fueling and/or central star formation. One possible reason for the discrepancy is the lack of a consistent scheme for classifying AGN. While the BPT diagram based on optical line ratios (Baldwin et al., 1981) is among the most common methods for identifying AGN, the demarcation between star-forming and AGN host galaxies is not consistent; some use the Kewley et al. (2001) criterion that excludes composite galaxies, while others use Kauffmann et al. (2003c) and include these along with Seyferts as AGN. The inclusion of LINERs can also complicate the picture; the high line ratios in at least some LINERs are spatially extended and thus likely of a non-AGN origin (Sarzi et al., 2010; Yan & Blanton, 2012; Singh et al., 2013).

Other challenges result from the task of identifying galactic bars, which is often done by visual inspection of optical images by individuals or small groups of experts. This introduces potential complications when there is disagreement between classifiers, especially in the cases of weak or nuclear bars. With only a single (or a few) classifications per image, such disagreements are difficult to resolve. Furthermore, individual visual inspection can limit the effective sample size due to the amount of time required to inspect images one by one. Our work avoids these problems by using crowdsourced citizen science classifications to identify galactic bars, where many individuals (an average of 27 classifiers for bar detection in this study) analyze each galaxy, and the presence of a bar is quantified as a calibrated vote fraction.

This paper re-examines the relationship between bars and AGN in disc galaxies by using Galaxy Zoo morphological classifications, and by using a strict AGN classification scheme which only selects Seyfert galaxies. We use this data to consider three physical scenarios for describing the role bars may (or may not) play in AGN fueling: I) Bars are necessary to fuel AGN, II) Bars are one of several ways to fuel AGN, or III) Bars do not fuel AGN. We discuss each of these possibilities in Section 6.4 and suggest the means by which the existence barred AGN, unbarred AGN, barred non-AGN, and unbarred non-AGN may be explained within the context of each model. We then report the scenario which we find to be best supported by both our observations and current theoretical models and simulations.

In Section 4.1 we describe our sample selection. Section 4.2 includes our data, with mass and colour distributions of the different activity types, both barred and unbarred, as well as a comparison between accretion strengths of barred and unbarred AGN. Interpretations of these results are discussed in Section 6.4, and the main conclusions are outlined in Section 6.5. We adopt a ΛCDM cosmology throughout the paper of $\Omega_m = 0.27$ and $H_0 = 71$ km s^{-1} Mpc^{-1} (Planck Collaboration et al., 2013).

4.1 Data and sample selection

Our parent sample of galaxies is taken from the SDSS Data Release 7 (Abazajian et al., 2009). From the spectroscopic Main Galaxy Sample (Strauss et al., 2002), we select galaxies within the redshift interval $0.01 < z < 0.05$ — the lower limit excludes galaxies whose angular size significantly exceeds the spectroscopic fiber, and the upper limit is chosen so that a reasonable estimate of bar detection can be made by visual inspection. From this, we create a volume-limited sample by applying an additional cut of $M_{z,petro} < -19.5$ AB mag.

Within the volume-limited sample, we use morphological cuts to select only disc galaxies at low inclination angles that are candidates for the presence of galactic bars (described below). These cuts result in the final sample of 19,756 disc galaxies used in the remainder of this paper.

4.1.1 Bar classifications and Galaxy Zoo 2

To select disc galaxies and measure the presence of a bar, we use data from the online citizen science project Galaxy Zoo 2 (GZ2).[1] With the help of over 80,000 volunteers providing over 16 million classifications of over 300,000 galaxies, Galaxy Zoo 2 is the largest extant survey of detailed galaxy morphology. Volunteers are shown colour images of galaxies taken from the SDSS (Figure 4.1), and are then prompted through a decision tree in which they answer questions about the galaxy's structure. For a detailed discussion on the Galaxy Zoo 2 project and its decision tree, see Willett et al. (2013).

Since bars only appear in disc galaxies, the sample must be limited to disc galaxies in which a bar can be seen via visual inspection. We begin by selecting galaxies for

[1] zoo2.galaxyzoo.org

Table 4.1. Summary of recent studies comparing the presence of galactic bars and active galactic nuclei, including new results from this work. Martini et al. (2003) is the only study with neither uniform selection criteria for galaxies nor a volume-limited sample. AGN classifications from optical line ratios and the BPT diagram are separated by the following demarcations: Ke01 = Kewley et al. (2001); Ka03 = Kauffmann et al. (2003c); S07 = Schawinski et al. (2007).

	Martini2001	Hao2009	Lee2012
Redshift range	$z < 0.038$	$0.01 < z < 0.03$	$0.02 < z < 0.055$
Abs. magnitude range	$B_T < 13.4$	$18.5 < M_g < -22.0$	$M_r < -19.5 + 5\log(h)$
Inclination limit	$R_{25} < 0.35$	$i < 60°$	$b/a > 0.6$
AGN classification method	varied	FWHM(Hα) > 1200 km/s and Ka03	Ke01
AGN type(s)	Type 1 and 2 Seyferts, LINERs	Type 2 Seyfert, LINER, composite	Type 2 Seyfert, LINER
Bar classification method	visual inspection	ellipse fitting	visual inspection
Number of AGN in sample	28	128	1742
Fraction of AGN hosts that are barred	28.6%	47%	49%
	Oh2012	Alonso2013	This work
Redshift range	$0.01 < z < 0.05$	$z < 0.1$	$0.01 < z < 0.05$
Abs. magnitude range	$M_r < -19$	$M_g < -16.5$	$M_{z,petro} < -19.5$
Inclination limit	$b/a > 0.7$	$b/a > 0.4$	$p_{\mathrm{not\ edge-on}} > 0.6$
AGN classification method	Ka03	Ka03	S07, WISE
AGN type(s)	Type 2 Seyfert, LINER, composite	Type 2 Seyfert, LINER, composite	Type 2 Seyfert
Bar classification method	visual inspection	visual inspection	crowdsourced visual inspection
Number of AGN in sample	1397	6772	681
Fraction of AGN hosts that are barred	51%	28.5%	51.8%

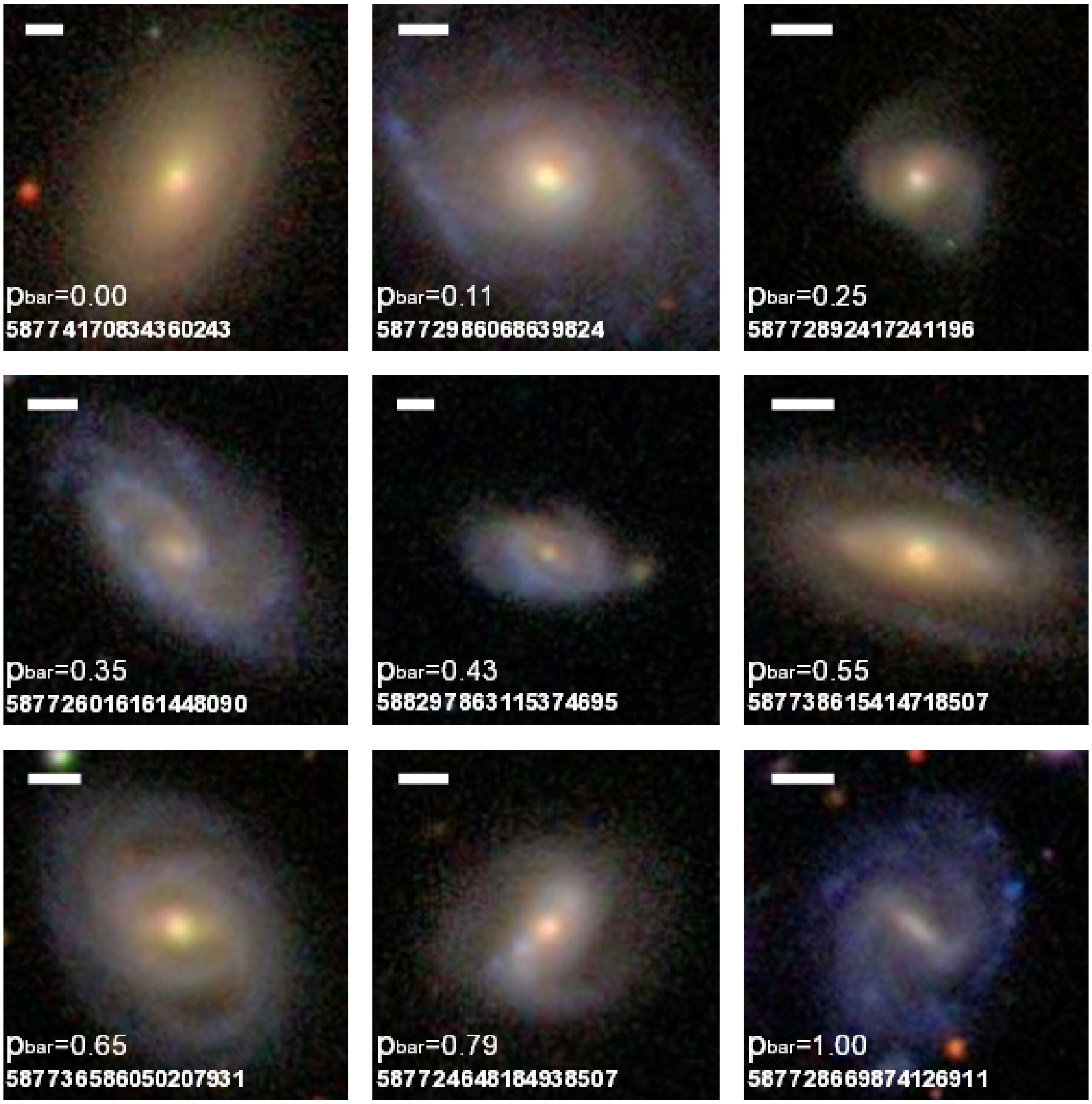

Figure 4.1 Examples of the SDSS images used in Galaxy Zoo 2, sorted by increasing $p_{\rm bar}$ (the weighted percentage of users that detected a bar in each image). All galaxies are from our final analysis sample of "not edge-on" disc galaxies. The white lines in the upper left of each image represent a physical scale of 5 kpc. We also give $p_{\rm bar}$ and the SDSS objectIDs for each galaxy. **Top row:** Galaxies with $p_{\rm bar} < 0.3$, which in this paper are designated as unbarred. **Middle and bottom rows:** Galaxies with $p_{\rm bar} \geq 0.3$, which we designate as reliably barred.

which at least 10 people answered the question, "Is there a sign of a bar feature through the centre of the galaxy?", thus rejecting vote fractions with low statistical significance. Because questions in GZ2 are implemented as part of a decision tree (Willett et al., 2013), users must have identified a galaxy as a disc and as not edge-on before answering the bar question. In this way, the cut of $N_{bar} \geq 10$ increases the likelihood that the galaxy in question is a candidate for having a bar. This cut is not complete, however, for galaxies which have a high number of total classifications. In these cases, the number of users to answer the bar fraction may still be small compared to the number of users identifying the galaxy as either not disc-like, or as an edge-on galaxy. Therefore cuts are also applied to the vote fractions relating to questions preceding the bar question. The first question of the GZ2 tree reads, "Is the galaxy simply smooth and rounded, with no sign of a disc?" Willett et al. (2013) determined the threshold fraction of "features or disc" answers required to classify the galaxy as a disc, when combined with the cut $N_{bar} \geq 10$, to be $p_{\text{features or disk}} \geq 0.227$. We emphasize that the cuts provided in Willett et al. (2013) are intended to be *minimum* values for determining well sampled galaxies. We thus chose to adopt a slightly higher value of $p_{\text{features or disk}} \geq 0.35$ to create the cleanest possible sample, based on a visual inspection of a subsample of galaxies with these cuts. To assess whether the results would be affected by this choice, we also created a sample with the original Willett et al. (2013) cuts. This choice increased the number of AGN in the sample by 24, and did not affect the final results. Therefore we present the sample using our more conservative cuts in this paper.

Following an answer of "features or disc" for the first question, the volunteer is then asked "Could this be a disc viewed edge-on?" Bars become increasingly difficult to detect in galaxies at high inclination angles, and are nearly impossible to detect in edge-on galaxies without careful isophotal mapping. The threshold vote fraction determined by Willett et al. (2013) of a "No" answer to this question is $p_{\text{not edge-on}} \geq 0.519$. We again adopt a slightly more conservative value of $p_{\text{not edge-on}} \geq 0.6$ based on visual inspection of a subsample. The combination of feature/disc galaxies that are not edge-on for these two thresholds results in the final sample size of 19,756 galaxies used in this paper.

As a check that our selection of "not edge-on" disc galaxies can be reliably used to identify a bar, we examine the inclination angle of the sample, which is approximated by the ratio of the best fit of the semi-major and -minor axes $i = \cos^{-1}(a/b)$ as measured in r-band by the SDSS pipeline. Figure 4.2 shows the strong correlation between i and $p_{\text{not edge−on}}$, with a sharp cutoff near $i = 70°$. Our cutoff of $p_{\text{not edge−on}} \geq 0.6$ effectively limits the sample to inclination angles of $i < 67°$. In Figure 4.2 we also show the dependence of the GZ2 bar fraction on $p_{\text{not edge−on}}$. The bar fraction remains roughly constant (± 0.1) between $0.3 < p_{\text{not edge−on}} < 1.0$ and drops to zero at $p_{\text{not edge−on}} < 0.1$. Since the *true* bar fraction is expected to be independent of i (a purely geometrical effect assumed to have a random distribution), any change in the bar fraction would reflect the ability of visual inspection to detect a bar in a highly inclined disc. The constant bar fraction out to our limit of $p_{\text{not edge−on}} \geq 0.6$ (and well beyond) is a necessary requirement for an unbiased selection of barred galaxies; as a result, we are confident that the crowdsourced bar classifications in this sample are reliable.

Finally, if the volunteer answers “No” to the edge-on question, they are asked “Is there a sign of a bar feature through the centre of the galaxy?” Possible answers to this question are either “Bar” or “No bar”. Willett et al. (2013) compared expert classifications of barred galaxies from both Nair & Abraham (2010) and Baillard et al. (2011) to Galaxy Zoo 2 data, and show that a threshold of $p_{\text{bar}} \geq 0.3$ is the most reliable separator of the barred from unbarred population (see their Figure 10). We adopt the same threshold of $p_{\text{bar}} \geq 0.3$ for determining whether a galaxy has a bar (see Figure 4.1 for images of galaxies with different values of p_{bar}).

We compare our morphology cuts to those used by Masters et al. (2011), who used an early release of GZ2 data to identify barred galaxies. Their study also required $N_{bar} \geq 10$ and claim that this cut alone is sufficient to restrict the sample to disc galaxies without applying an additional cut on $p_{\text{features or disk}}$. This assumption was reasonable at the time since the Galaxy Zoo 2 project was still collecting data, and the number of classifications per galaxy was lower than in the final catalog. The median number of classifications per galaxy is roughly 30% higher, and so our data is more susceptible to contamination by non-disc galaxies with high classification counts. This makes an additional cut on $p_{\text{features or disk}}$necessary. To remove edge-on discs, Masters et al. (2011) set an inclination limit of $\log(a/b) < 0.3$, or $i \sim 60°$; this is comparable to our $p_{\text{not edge−on}}$cut, which corresponds to roughly $i \sim 67°$. To select barred galaxies, a majority vote fraction of $p_{\text{bar}} > 0.5$ was required, higher than our value of $p_{\text{bar}} \geq 0.3$. We

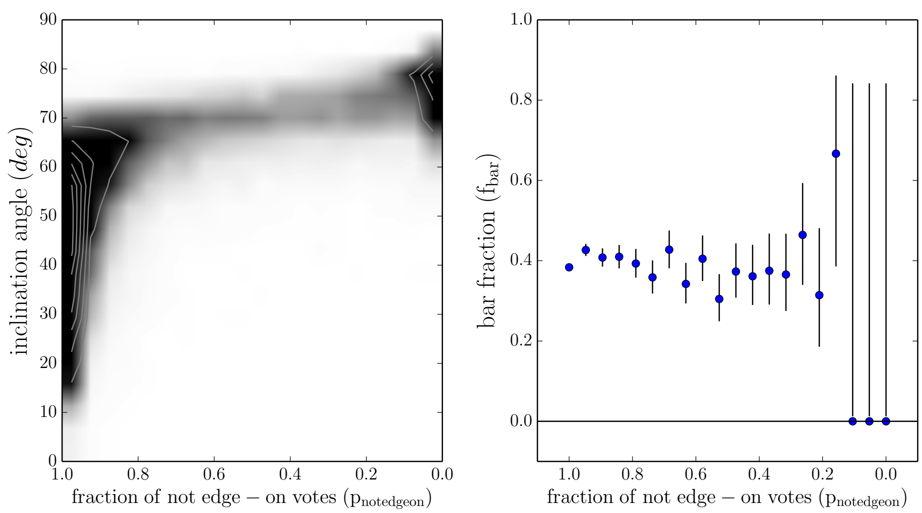

Figure 4.2 Left: Fraction of "not-edge-on" votes vs. inclination angle ($i = \cos^{-1}[a/b]$) for the disc galaxies in our GZ2 sample. An angle of 0° means the galaxy is completely face-on, while 90° is completely edge-on. GZ2 users consider a galaxy as "not edge-on" if the inclination angle is less than $i \sim 70°$. Right: Fraction of barred galaxies vs. fraction of "not edge-on" galaxies. The bar fraction is independent of the edge-on degree of the galaxies (above $p_{notedgeon} \sim 0.3$); the ability of users to detect bars does not decrease with inclination until $p_{notedgeon} \sim 0.3$, or $i \sim 70°$. Error bars are 95% Bayesian binomial confidence intervals (Cameron, 2013). This demonstrates that GZ2 data can reliably identify bars even in moderately-inclined disc galaxies.

are nevertheless confident in our threshold which was determined by the more recent and detailed analysis of the GZ2 data by Willett et al. (2013) as described above. Additionally, the data released at the time of Masters et al. (2011) had not yet been reduced via weighting and debiasing; these differences in vote fractions also contribute to the different cuts used in our study.

4.1.2 Activity type classification

We use flux measurements from the 2012 release of the Oh2011 catalogue (Oh et al., 2011) to classify disc galaxies as either star-forming, composite, AGN, LINER, or quiescent (also known as "undetermined"). This method employs ratios of ionOiii/Hβ fluxes as a function of ionNii, ionSii, or ionOi over Hα according to the BPT diagnostics. Our method for selecting AGN is the same as used by Schawinski et al. (2007, 2010). First, we use the ionNii/Hα ratio (Figure 4.3a). Any galaxy that does not have S/N > 3 for any of the four lines is unclassifiable via this method (possibly due to being gas-poor) and labeled "undetermined." Next, any galaxy which falls below the Kewley et al. (2001) extreme starburst line is classified as star-forming, and those that fall between this and the Kauffmann et al. (2003c) empirical starburst line are classified as composite. We note that some of these composite galaxies may be potential AGN, but we cannot cleanly separate the AGN contribution from star formation and thus exclude them from our sample (Schawinski et al., 2010).

Next, we identify the remaining galaxies (above the extreme starburst line) as either Seyfert AGNs or LINERs. Kewley et al. (2006) showed that both ionOi/Hα and ionSii/Hα diagrams are better-suited to distinguish AGN from LINERs; we thus use diagram (c) in Figure 4.3 if these galaxies also have S/N > 3 in ionOi. For galaxies which do not have S/N > 3 in ionOi, but do in ionSii, we use diagram (b). In both cases, we use the AGN-LINER division line of Kewley et al. (2006). For the remaining galaxies, we use diagram (a) and implement the AGN-LINER division line of Schawinski et al. (2007).

Finally, to detect any AGN that may have been optically mis-classified due to obscuration, we identify AGN based on their infrared continuum shape using data from the Wide-field Infrared Survey Explorer (Wright et al., 2010, WISE). We identify as an AGN any galaxy with $(W1 - W2) \geq 0.8$ (Stern et al., 2012). Based on infrared data, we

Activity type	All discs		Barred discs	
	Number	f_{total}(%)	Number	f_{bar}(%)
star-forming	11282	57.1 ±+0.7−0.7	4183	37.1 ±+0.9−0.9
composite	2853	14.4 ±+0.6−0.4	1301	45.6 ±+1.8−1.8
AGN	681	3.4 ±+0.3−0.2	353	51.8 ±+3.8−3.7
LINER	1321	6.7 ±+0.4−0.4	695	52.6 ±+2.7−2.7
undetermined	3619	18.3 ±+0.6−0.5	1654	45.7 ±+1.6−1.6
total	19756	100	8186	41.4 ±+0.7−0.7

Table 4.2 Results of activity classification for our sample of 19,756 not edge-on disc galaxies. f_{total} is the percentage of the total sample represented by each activity (number of galaxies of that type / total number of galaxies). f_{bar} is the percentage of each subsample that are barred (number of galaxies of that type that are barred / total number of galaxies in that type). Errors are 95% Bayesian binomial confidence intervals (Cameron, 2013).

re-classified fourteen galaxies (originally classified optically as three star-forming, ten composites, and one LINER) as AGN.

We show the results of the activity type and morphological classifications in Table 4.2. The numbers and fractions of each activity type with respect to the full sample are shown, as well as the numbers and fractions of barred galaxies within each activity type. These results are discussed in Section 4.2.

4.2 Results

To determine whether a correlation exists between galaxies that host an AGN and those that contain large-scale stellar bars, we examine the fractions of barred and unbarred AGN with respect to mass, colour, and AGN strength. We use stellar masses from the `AVERAGE` values in the MPA-JHU DR7 catalogue (Kauffmann et al., 2003a). Colours are $^{0.0}(u-r)$ values from SDSS DR7, which have been both de-reddened for Galactic extinction and k-corrected to redshift $z = 0.0$ (Csabai et al., 2003). Stellar velocity dispersions are taken from Oh et al. (2011).

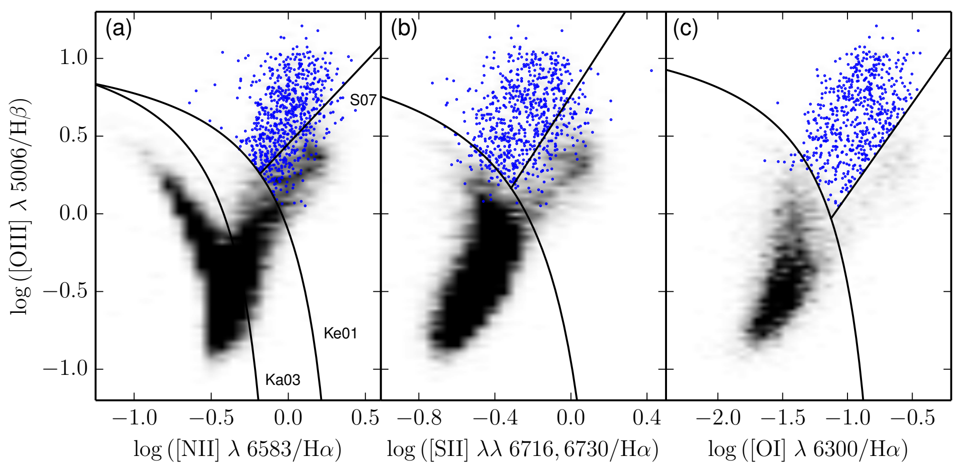

Figure 4.3 Optical line diagnostics for activity types of 19,756 disc galaxies. Any galaxy with S/N $<$ 3 for ionOiii, Hβ, ionNii, or Hα is unclassifiable using this method and labeled as "undetermined". The 3,619 undetermined galaxies do not appear on the diagram above. The remaining 16,137 galaxies were categorized according to the above diagrams in the following order, based on the method of Schawinski et al. (2007). First, diagram (a) was used to identify star-forming and composite galaxies. Any galaxy below the Ka03 line was classified as star-forming, while those that fell between the Ka03 and Ke01 lines were classified as composite. Next, to distinguish AGN from LINERs, we use diagrams (b) and (c). If a galaxy had $S/N > 3$ for ionOi, diagram (c) was used. If a galaxy did not have $S/N > 3$ for ionOi, but did for ionSii, diagram (b) was used. Last, if a galaxy did not have $S/N > 3$ for ionOi or ionSii, but did for ionNii, diagram (a) was used. In each panel, only galaxies with $S/N > 3$ for all four lines required by that diagram are shown. Galaxies designated AGN by any of the three optical line diagnostics are plotted as blue points, while the black shading represents the full sample of emission-line galaxies.

4.2.1 Barred AGN fraction at a fixed mass and colour

Figure 4.4 shows the distributions of mass and colour for AGN and star-forming activity types, split into barred and unbarred subsamples. The median AGN is more massive (by 0.6 dex) and redder (by 0.5 mag) than the median star-forming galaxy. This agrees with previous optical studies of AGN and star-forming galaxies in the local Universe (Schawinski et al., 2007; Lee et al., 2012; Oh et al., 2012; Alonso et al., 2013). Aird et al. (2012) demonstrate that this difference is primarily caused by selection effects relating to the underlying Eddington ratio distribution. The probability of a galaxy hosting an AGN is assumed to be independent of stellar mass, and thus AGN are prevalent at all masses in the range $9.5 < \log(M/M_{\odot}) < 12$, despite only being observable at higher masses. As a result, we expect higher absolute numbers of barred AGN in a flux-limited sample since barred disc galaxies are also on average redder and more massive than unbarred disc galaxies (Masters et al., 2011, 2012). We interpret this as the primary cause for the higher fraction of barred AGN (51.8%) versus barred star-forming (37.1%) galaxies in Table 4.2.

To control for this selection effect, we examine the fraction of AGN at fixed masses and colours (Figure 4.5). The total disc galaxy sample spans a mass range from $9.0 < \log(M/M_{\odot}) < 11.5$, while the colour range extends from $1.0 < (u-r) < 3.5$. AGN hosts are found throughout the disc galaxy sample, but most appear in galaxies with $\log(M) > 10^{10}\ M_{\odot}$. When examining the fraction of galaxies with an AGN as a function of mass and colour, redder and more massive galaxies have AGN fractions as high as 10%. Bins with fewer than 10 total AGN (barred AGN + unbarred AGN) are masked to minimize variance from small sample sizes. The same trend is also seen when splitting the disc galaxy sample into barred and unbarred subsamples.

To analyze the difference between the barred and unbarred AGN populations, we plot the difference in barred and unbarred AGN fractions in Figure 4.6. This quantity is defined as:

$$d_{\mathrm{B-NB}} = \text{barred AGN fraction} - \text{unbarred AGN fraction} \tag{4.1}$$

and is calculated in each of the mass/colour bins in Figure 4.5. For each bin, a positive value represents a greater fraction of barred AGN and is coloured blue; a negative value

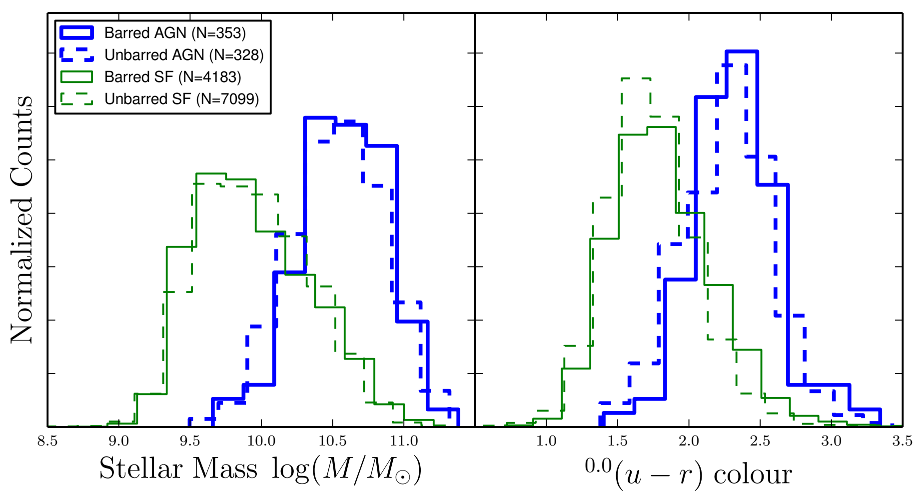

Figure 4.4 Mass and colour distributions for disc galaxies in the GZ2 sample, separated by both activity type (either AGN or star-forming as in Table 4.2) and the presence of a galactic bar. AGN (green) are on average both significantly redder and more massive than star-forming galaxies (blue). When splitting the disc galaxies into barred (solid lines) and unbarred (dashed lines), however, there is no significant difference between the two populations. Counts are normalized so that the sum of bins is equal to 1 for each sample.

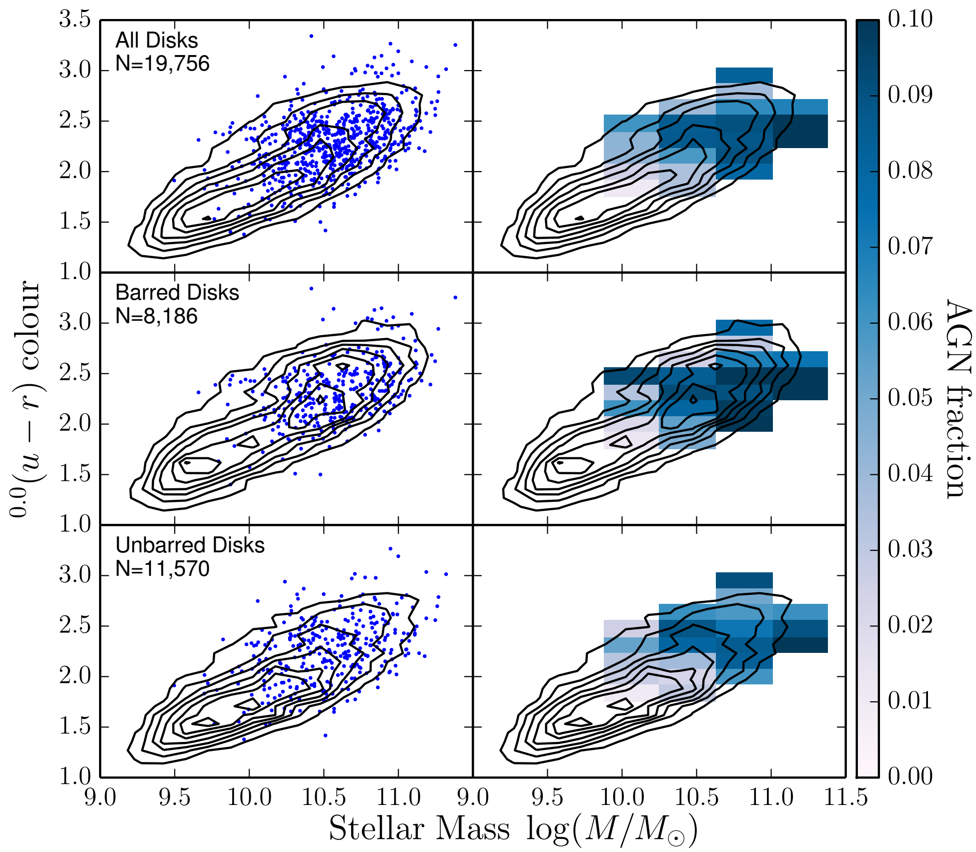

Figure 4.5 Optical colour vs. stellar mass for disc galaxies in GZ2. Black contours represent all disc galaxies (top), all barred galaxies (middle), or all unbarred galaxies (bottom). All AGN (top), barred AGN (middle), and unbarred AGN (bottom) are plotted in the left panels as blue dots; the right panels show the AGN fraction in each colour/mass bin. Bins with $N_{AGN} < 10$ are masked.

represents a greater fraction of unbarred AGN and is coloured red.

Since our AGN sample is divided into relatively small subsamples, we examine how the size and placement of the mass/colour bins affect the results of Figure 4.6. To control for this effect, we examine the average value of $d_{\mathrm{B-NB}}$ and the fraction of bins with $d_{\mathrm{B-NB}} > 0$, defined as:

$$f_{\mathrm{B>NB}} = \frac{\text{number of bins with higher barred AGN fraction}}{\text{total number of bins}}. \tag{4.2}$$

We compute $f_{\mathrm{B>NB}}$ for 400 combinations of mass and colour bin widths between $0.2 \leq \Delta\log(M/M_{\odot}) \leq 0.6$ and $0.12 \leq \Delta(u-r) \leq 0.35$. The distribution of results from all combinations is shown in Figure 4.7. Our final bin choice (as seen in Figure 4.6) has a mass width of $\Delta\log(M/M_{\odot}) = 0.375$ (16 bins) and colour width of $\Delta(u-r) = 0.16$ (22 bins). This choice lies near the peak of the distributions for both $f_{\mathrm{B>NB}}$ and $d_{\mathrm{B-NB}}$, while maximizing the total number of bins to decrease the uncertainty on statistical tests.

For the first time among recently published studies, we quantify the level of correlation between the presence of a bar and AGN through statistical analysis. We test the null hypothesis that in the absence of a causal link, the difference between barred and unbarred AGN fractions when binned by mass and colour should be centered around zero. The null hypothesis also requires that the likelihood distribution decreases symmetrically from zero in both directions; as a result, we assume a normal distribution with mean $\mu = 0$ and standard deviation σ. Other models of the null hypothesis could of course also be tested, but we adopt this as the simplest reasonable scenario that fits the constraints of the problem.

To assess the level of statistical significance, we fit the data in Figure 4.6 with a range of models with varying mean ($d_{\mathrm{B-NB}}$) and standard deviation (σ_d) and then apply an Anderson-Darling test. We selected this test because it has been empirically shown to be more powerful and reliable at testing normality than traditional χ^2 or Kolmogorov-Smirnov tests, especially with small ($n < 30$) sample sizes (Hou et al., 2009). The confidence threshold required for the model to pass at fitting the data is 95%. In Figure 4.8, we show the distribution of the Anderson-Darling statistic A^2 as a function of σ_d for two of the tested models: the null hypothesis ($d_{\mathrm{B-NB}} = 0$) and the best fit to the data ($d_{\mathrm{B-NB}} = 0.012$). The null hypothesis fails the Anderson-Darling

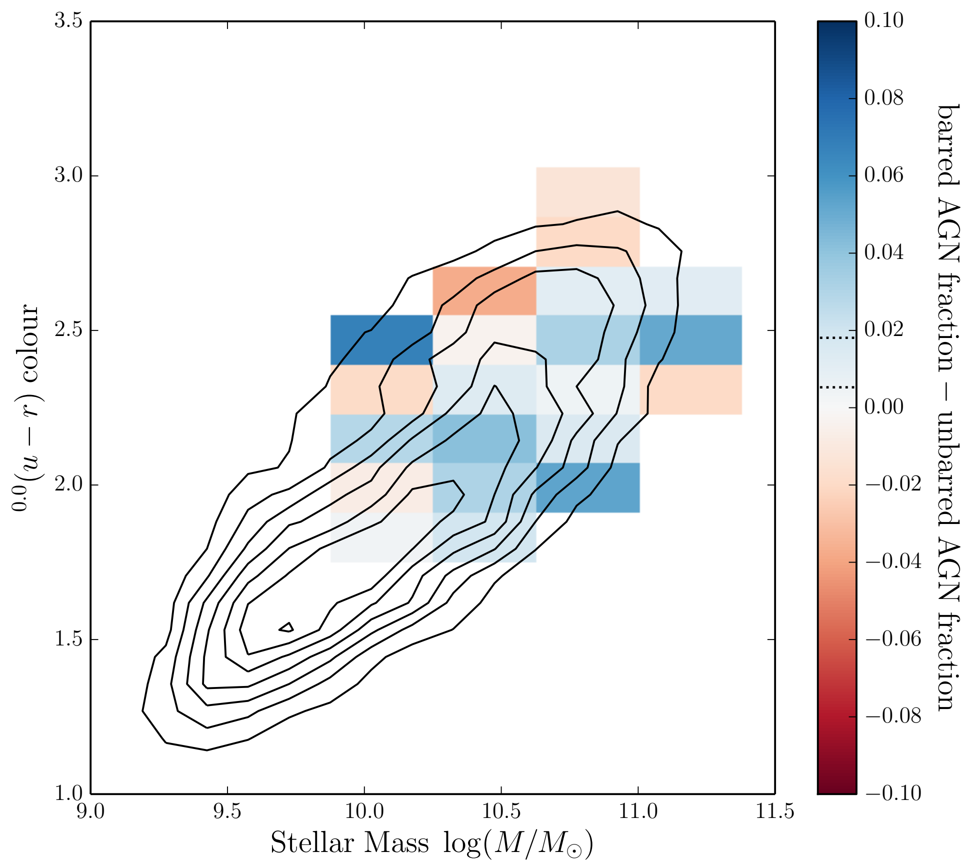

Figure 4.6 Optical colour vs. stellar mass for barred and unbarred disc galaxies in GZ2. Coloured bins show the difference between the AGN fractions for barred and unbarred galaxies. Blue bins have higher fractions of barred galaxies, red bins have more unbarred galaxies, and pale/white indicates no difference. The region on the colourbar enclosed by the dotted lines represents the mean of the data determined by the Anderson-Darling test. The colour gradient is on the same scale as Figure 4.5. Bins with $N_{AGN} < 10$ are masked. A colour version of this plot may be found in the electronic edition of the journal.

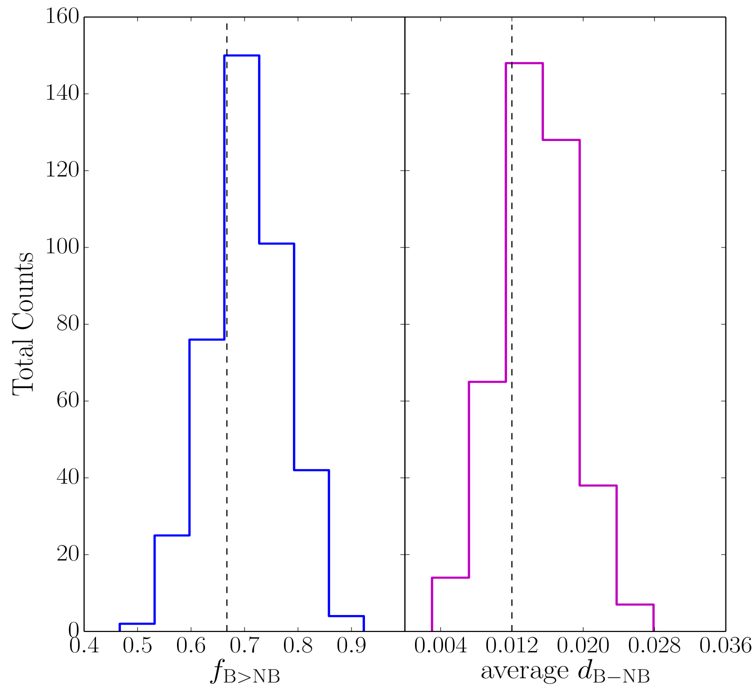

Figure 4.7 Distributions of the difference in the fraction of bins with excesses of barred AGN ($f_{\mathrm{B>NB}}$) and the average difference between barred and unbarred AGN fractions ($d_{\mathrm{B-NB}}$). Both values are computed for 400 variations in the mass and colour bin widths. *Left*: The average fraction of bins with a higher barred AGN fraction is $f_{\mathrm{B>NB}} = 0.705 \pm 0.073$. *Right*: The average difference in barred and unbarred AGN fractions is $d_{\mathrm{B-NB}} = 0.015 \pm 0.004$. Dashed black lines indicate the values of $f_{\mathrm{B>NB}}$ and average $d_{\mathrm{B-NB}}$ used in Figure 4.6 and subsequent analysis.

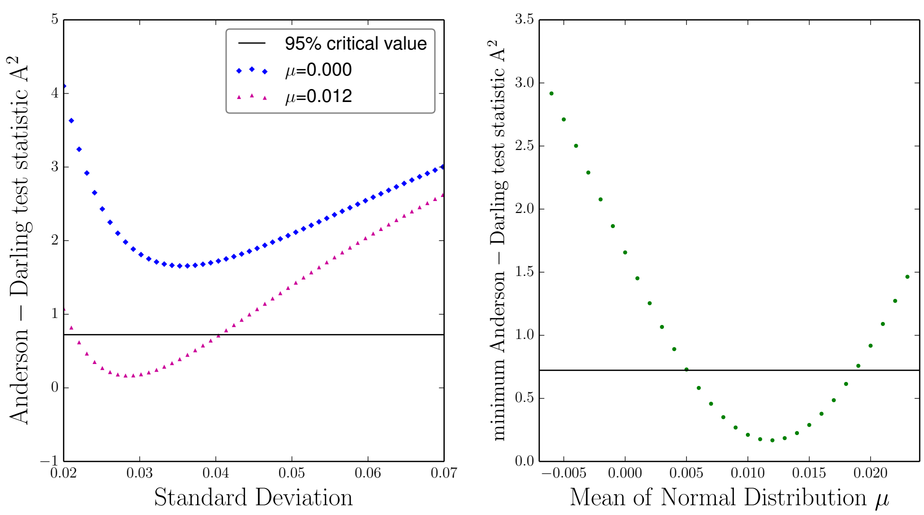

Figure 4.8 Fits of the binned fraction of barred vs. unbarred AGN fractions to a normal distribution. *Left:* value of the Anderson-Darling test (A^2) as a function of the standard deviation of the normal distribution being fit (σ_d). The horizontal black line shows the critical value of A^2 corresponding to 95%; a model must fall below this line to be considered an acceptable fit at this level of confidence. Two models are shown: the null hypothesis (blue diamonds) and the best fit to the data in Figure 4.6 (purple triangles). *Right*: Plot of the minimum A^2 for the full range of means ($d_{\mathrm{B-NB}}$) tested for the data. This shows that acceptable fits can be found for $0.005 < d_{\mathrm{B-NB}} < 0.019$, but that the null hypothesis is ruled out at 95% confidence.

test for all values of σ_d, indicating that the 66.7%pm+16.1%−21.6% fraction of bins that have a higher barred than unbarred AGN fraction is statistically significant. The best fit to the data, by contrast, has a mean of $d_{\mathrm{B-NB}} = 0.012 pm{+0.007}{-0.007}$ and $\sigma_d = 0.028$. The positive value of $d_{\mathrm{B-NB}}$ indicates an increase in the AGN fraction for barred galaxies, consistent with the hypothesis that at least some fraction of AGN activity is triggered or sustained by bar-driven fueling.

4.2.2 Comparing barred and unbarred AGN accretion strengths

If the presence of a bar does contribute to AGN fueling, one possible result would be an increase in the accretion rate for barred AGN hosts vs. those that are unbarred. To assess this, we compare relative accretion strengths using the quantity $R = L_{[\mathrm{O\ III}]}/M_{\mathrm{BH}}$, with $L_{[\mathrm{O\ III}]}$ as a proxy for the AGN bolometric luminosity. ionOiii luminosities were calculated using fluxes from Oh et al. (2011), and black hole masses estimated using the M_{BH}-σ relation:

$$\log\left(\frac{M_{\mathrm{BH}}}{M_{\odot}}\right) = \alpha + \beta \log\left(\frac{\sigma}{200\ \mathrm{km\ s^{-1}}}\right). \tag{4.3}$$

Here α and β are empirical values determined from the observed relationship between black hole mass and velocity dispersion σ. We adopt the parameters measured by Gültekin et al. (2009) of $(\alpha, \beta) = (8.12 \pm 0.08, 4.24 \pm 0.41)$.

It has been demonstrated for smaller samples of galaxies that the parameters α and β vary as a function of morphological type (Graham et al., 2011; Gültekin et al., 2009; Brown et al., 2013), including differences between barred and unbarred galaxies. We choose not to use (α, β) parameters where (α, β) are derived from separate subsamples for two reasons. First, since the M_{BH}-σ relation is calibrated from small samples of nearby galaxies, the statistical error on the parameters increases as galaxies are divided into smaller sub-groups. The calibration of Gültekin et al. (2009), for instance, is based on measurements of only eight barred galaxies. The error in β for the barred M_{BH}-σ relation is $\sigma_\beta = \pm 0.751$, almost twice the error obtained by fitting to the full sample of disc galaxies. Second, while different studies report consistent values for α and β when all disc galaxies are considered, the values can vary significantly when splitting by morphological type. Lee et al. (2012) and Alonso et al. (2013) use separate values for (α, β) and report conflicting levels of agreement, depending on which parameters are used. This raises the possibility that differences in AGN strength are simply due to differences in calibration parameters, and not in the true distribution of accretion efficiencies.

Figure 4.9 shows the relative accretion strengths R for our sample as a function of mass and colour for both barred and unbarred AGN; these values are inversely correlated with both mass and $(u-r)$ colour. This trend is likely driven by the same selection effects described in §4.2.1 (Aird et al., 2012). At a fixed $L_{[\mathrm{O~III}]}/M_{\mathrm{BH}}$ ratio, AGN with lower mass black holes are less likely to be detected due to the signal to noise requirements on their spectral lines. This biases the distribution of R toward higher mass black holes. Since stellar mass is strongly correlated with black hole mass (Hring & Rix, 2004; Gültekin et al., 2009; Merloni et al., 2010), and stellar mass correlates with optical colour (Kauffmann et al., 2003a), this explains the trend seen in both parameters for an uncorrected sample.

Since these observationally-driven selection effects are likely to affect barred and unbarred galaxies equally, we compare the values of R of both groups without any corrections. A two-sided KS-test yields a p-value of $p = 0.127$ for the two distributions. This is consistent with both the barred and unbarred galaxies being drawn from the same distribution. We thus conclude that there is no strong evidence for a difference in accretion strength between barred and unbarred AGN.

This result contradicts Alonso et al. (2013), who found an excess of barred AGN with high values of R. We conjecture that this may be the result of their sample selection, which excluded galaxies with $M_\star < 10^{10} M_\odot$ in favor of a higher redshift limit of $z = 0.1$. However, low mass galaxies have higher $L_{[\mathrm{O~III}]}/M_{\mathrm{BH}}$ ratios and are more likely to be unbarred than their higher mass counterparts (Lee et al., 2012). If this effect is real, it appears to be limited to high-mass galaxies (which themselves are subject to selection effects due to the methods used to measure R). Additionally, Alonso et al. (2013) include composites and LINERs in their sample of AGN. If the activity from these galaxies is not primarily from black hole accretion, R is not a true proxy for accretion strength, and comparisons between barred and unbarred galaxies do not accurately probe differences between the two populations. To test this, we compare R distributions for barred and unbarred composite + AGN + LINER galaxies with $M_\star > 10^{10} M_\odot$. For these

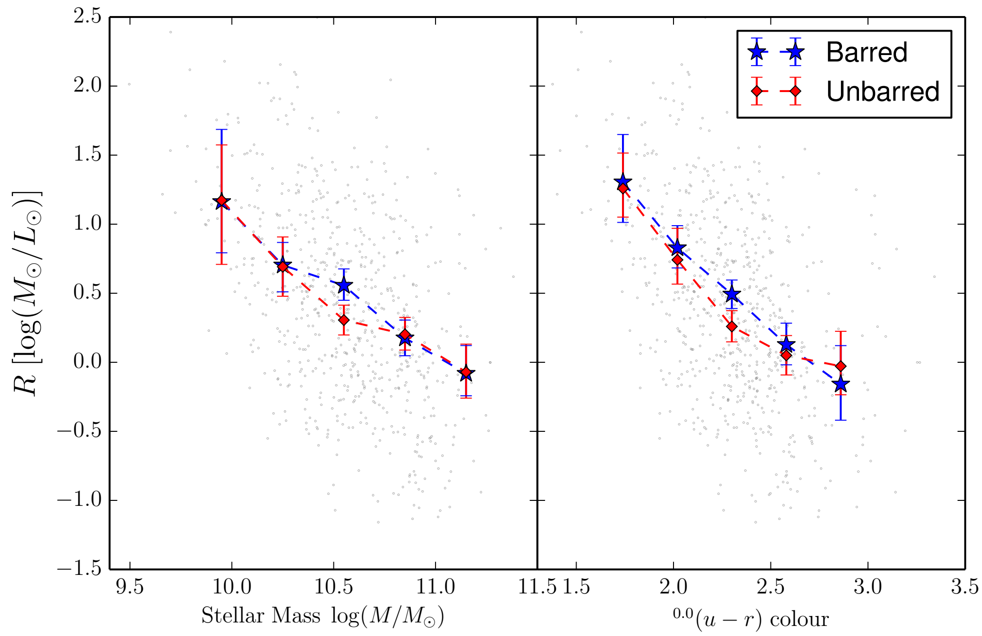

Figure 4.9 **Left:** Relative accretion strength R vs stellar mass for barred (blue) and unbarred (red) AGN in our sample. R is plotted as the mean of values within five equal-width bins in the range $9.8 < \log(M/M_\odot) < 11.3$, which includes 98% of the AGN sample. Points are drawn at the midpoint of each bin. **Right:** R vs colour for barred and unbarred AGN. R is plotted as the mean of values within five equal width bins in the colour range $1.6 < (u-r) < 3.0$, which includes 96% of the AGN sample. Error bars for each plot are 95% confidence intervals, calculated by bootstrapping with 1000 times resampling. There is no significant difference in accretion strengths for barred and unbarred AGN as a function of either mass or colour.

galaxies, the difference in the average values of R for the barred and unbarred samples is 0.09 $(L_\odot/M_\odot)^{-1}$ (compared to a difference of 0.06 $(L_\odot/M_\odot)^{-1}$ when considering only AGN with no cut on stellar mass), and a KS-test for the distributions yields a p-value < 0.01, which agrees with the results of Alonso et al. (2013). We note that our results are consistent with Lee et al. (2012), who have a similar mass range to our sample of disc galaxies, and do not include composites in their sample.

4.3 Discussion

We have compared a sample of 353 barred Seyfert AGNs to 328 unbarred Seyferts and measure the potential correlation between the presence of the bar and the AGN. We find that at fixed mass and colour, AGN hosts show a small increase in the fraction of galaxies that are barred. The average difference is $d_{\mathrm{B-NB}} = 0.012$, or roughly 16.0% of the average barred AGN fraction. We find no difference in the $L_{[\mathrm{O~III}]}/M_{\mathrm{BH}}$ ratio between barred and unbarred AGN at either fixed mass or colour. We conclude that while AGN hosts have moderately higher probabilities of hosting a bar, the presence of the bar does not seem to affect either the quantity or efficiency of fueling the central black hole.

If bars are not required to initiate AGN fueling, then what is the source? There must be a process that transports angular momentum through the galactic disc and creates/maintains an accretion disc. Both theoretical models (Shlosman et al., 1989, 1990) and numerical simulations (Hopkins & Quataert, 2010) indicate that this process requires two stages. First, the gas must be driven from a radial scale of megaparsecs down to kiloparsecs. Standard viscous torques on the gas are too inefficient to initiate gas inflow by themselves Shlosman et al. (1989); Bournaud et al. (2005); therefore, some other mechanism is required. Within the central kiloparsec, a secondary instability must take over within the gaseous disc for AGN fueling to occur.

In the context of this general model, we consider three possibilities: (I) Bars are a necessary ingredient for fueling AGN, (II) Bars are one of multiple processes that fuel AGN, or (III) Bars play no role in fueling AGN. We also discuss in each scenario possible explanations for the existence of all four observed combinations: barred AGN, unbarred AGN, barred non-AGN, and unbarred non-AGN.

4.3.1 Scenario I: Bars are necessary to fuel AGN

If the presence of a stellar bar is the only mechanism by which gas can be driven to the ~ 1 kpc scale, there must be a reason both barred and unbarred AGN are observed in large numbers. One possibility is that a galactic bar *initiates* fueling of the black hole, but is subsequently destroyed in a dynamic timescale shorter than the lifetime of the AGN. These separate timescales are not currently known with certainty, but estimates place the lifetime of an AGN from 10^6 — 10^8 years (eg, Schawinski et al., 2010; Martini, 2004). The range of bar lifetimes is not yet firmly established; some models show bars to be transient features that are destroyed either due to buckling from angular momentum transport or from the build-up of a central mass concentration (CMC) (Bournaud et al., 2005; Combes, 2007). In these models, the lifetime of a bar is estimated to be $1-2$ Gyr. Kraljic et al. (2012) also found bars to be short-lived in their simulations, but only early bars (formed at $z > 1$). Bars formed later (at $z < 1$) were maintained down to $z = 0$, giving a lifetime of at least 8 Gyr.

Other simulations (Debattista et al., 2004, 2006; Athanassoula et al., 2005, 2013; Shen & Sellwood, 2004) do not observe bar destruction due to buckling. In these cases, only a sufficently massive CMC is capable of destroying the bar on Gyr timescales. The mass of the CMC required in these models is at least several percent of the total mass of the disc — this is significantly larger than the mass measured in local disc galaxies. If the CMC is insufficently large, the bar is maintained for the lifetime of the disc (up to 10 Gyr; Athanassoula et al., 2013), and thus should be observable for at least the lifetime of the AGN.

If bars are truly long-lived structures in all disc galaxies and are necessary to fuel AGN, we would expect a much higher value of the ratio of barred to unbarred AGN hosts. Since the observed numbers are nearly 1:1, we consider this scenario highly unlikely. It is possible that bars are necessary to fuel AGN, but the number of observed unbarred AGN can only be explained if the factor of ~ 10 difference between the upper end of the AGN lifetime and the lower end of the bar lifetime can be resolved. While this is possible, we consider it unlikely given the assumptions required.

4.3.2 Scenario II: Bars are one of several ways to fuel AGN

If stellar bars are only one of several ways to fuel AGN, then both barred and unbarred AGN should exist (as should both barred and unbarred star-forming galaxies). The simulations conducted by Hopkins & Quataert (2010) support this model, which show that multiple large-scale mechanisms (including a stellar bar) can be responsible for transporting gas to scales required for AGN fueling. Further, if bar-driven fueling is responsible for some fraction of the AGN, this model predicts an increase in the fraction of barred AGN, which our data supports.

While the existence of unbarred AGN is explained by this model, there is no immediate explanation for the existence of barred galaxies that do not host AGN; here we suggest several possibilities. First, a bar that initiates AGN fueling may simply outlive the AGN (see 4.3.1), which agrees with estimates of both bar and AGN lifetimes. Second, there could be a correlation between bar strength and AGN activity, where only sufficiently strong bars initiate fueling. This is consistent with Lee et al. (2012), who find a higher AGN fraction in barred galaxies where the bar length is at least 1/4 of the total disc diameter. They did not test, however, whether this relationship remains at fixed mass and colour. Finally, the emission from an AGN is expected to be highly variable with time, driven by processes such as accretion disc instabilities and/or feedback within the accreting material (Hickox et al., 2014). In this case, barred galaxies without AGN are simply observed in low parts of their duty cycle, with Eddington ratios too low to be detected at the limits of our observations.

4.3.3 Scenario III: Bars do not fuel AGN

Finally, we consider the possibility that stellar bars do not trigger AGN activity in any way. This is inconsistent (although marginally so) with the increase in barred vs. unbarred AGN fractions that we find at fixed mass and colour. One possibility is that the model used for the null hypothesis (a normal distribution centered at $d_{\mathrm{B-NB}}= 0$) does not apply. Detailed simulations of cosmological volumes that include both AGN and detailed disc morphology, such as *Illustris* (Vogelsberger et al., 2014) and EAGLE (Schaye et al., 2014) should ultimately provide more well-defined priors for this.

In addition, our test of the null hypothesis could still be consistent with a strong effect even if the total number of barred and unbarred bins were equal. For example, if bar-driven fueling is strongly mass-dependent, the $d_{\mathrm{B-NB}}$ bins could have excesses of barred AGN at high masses and deficits at low masses; this would still be consistent with a distribution centered at zero. We test the simplest cases by simply splitting the sample into two in both mass and colour (Table 4.3). Low- and high-mass disc galaxies (dividing the sample at $\log(M/M_{\odot}) = 10.625$) have nearly identical values of $f_{\mathrm{B>NB}}$ and mean $d_{\mathrm{B-NB}}$; there is no evidence of a mass-dependent effect on bar-driven AGN fueling. When splitting discs into red vs. blue (at a colour of $(u-r) = 2.22$), bluer galaxies do have significantly more bins with an excess of barred AGN ($f_{\mathrm{B>NB}}= 0.88$) than redder

	sample	$f_{\mathrm{B>NB}}$	Mean $d_{\mathrm{B-NB}}$
low mass	$\log(M/M_{\odot}) < 10.625$	0.70	0.0125
high mass	$\log(M/M_{\odot}) > 10.625$	0.64	0.0123
blue	$(u-r) < 2.22$	0.88	0.023
red	$(u-r) > 2.22$	0.54	0.006

Table 4.3 Difference between barred and unbarred AGN fractions for disc galaxies when splitting the sample in two by both mass and colour. $f_{\mathrm{B>NB}}$ is the fraction of bins that show an excess of barred AGN (compared to unbarred), while $d_{\mathrm{B-NB}}$ is the average value of the differences over all bins. Since the number of bins in each subsample is only $\sim 8-13$ when splitting by mass or colour, the uncertainty in $f_{\mathrm{B>NB}}$ is correspondingly large.

galaxies ($f_{\mathrm{B>NB}}$= 0.54). The uncertainties on $f_{\mathrm{B>NB}}$ are quite large, though, since each subsample has less than a dozen bins. Our splits by colour agree with (Oh et al., 2012), who find that bar effects on AGN are more pronounced in bluer and less massive galaxies. Lee et al. (2012), in contrast, find that $f_{\mathrm{B>NB}}$ depends on neither mass nor colour.

If bars have no impact at all on the likelihood of a disc galaxy hosting an observable AGN, this is inconsistent with both the models and simulations that demonstrate efficient gas-driven inflow by bar structures (Hopkins & Quataert, 2010). If the efficiencies of other morphologies that drive gas inflow are much higher than bars, though, this could also be consistent with our data. A lack of bar-driven fueling is consistent with the existence of both barred and unbarred AGN and star-forming galaxies, and the nearly equal numbers found in both pairs.

Given the limits on the data set (which is driven by binning the total number of disc galaxies by mass and colour), we do not completely rule out this model. However, given the small (but measurable) increase in the bar fraction from our data and the current constraints on both bar and AGN timescales, we propose that bar-driven fueling must account for at least some fraction of observed AGN activity (§4.3.2).

4.4 Conclusions

We have created a sample of 19,756 disc galaxies from SDSS DR7, using data from the Galaxy Zoo 2 project for morphological classifications of strong, large-scale bars. We studied the effects of stellar bars on 681 AGN and compared these effects to a control sample of disc galaxies both without bars and without AGN. The Galaxy Zoo 2 data provides a very large sample of disc morphologies for which the bar likelihood can be empirically quantified, based on crowdsourced visual classifications.

We find that the fraction of barred AGN (51%) is significantly greater than the fraction of barred galaxies with central star formation (37%). However, this is driven both by selection effects for detecting optically-identified AGN and by known correlations between black-hole mass and stellar mass, as well as stellar mass and optical colour. When examining the fraction of barred AGN as a function of a fixed mass and colour, we still find a small increase in the number of barred AGN hosts. The null hypothesis of no relationship between the two cannot be ruled out at the 95% confidence level. The $L_{[\mathrm{O\ III}]}/M_{\mathrm{BH}}$ ratio R (a proxy for the overall accretion rate) shows no dependence on the presence of a bar, once the same mass and colour constraints are applied.

Our results are consistent with a small relationship between the presence of a large-scale galactic bar and the presence of an AGN. We propose that while bar-driven fueling does indeed contribute to some fraction of the current observed population of growing black holes, other dynamical mechanisms, such as lopsided or eccentric stellar disk, must also contribute to the redistribution of angular momentum and thus the fueling of the accretion disk at small galactic radii.

Even with the advent of the large-scale SDSS data and the morphological classifications from Galaxy Zoo 2, this result is still constrained by the total number of galaxies in our study. Larger samples of disk galaxies with activity and morphological classifications, notably the Dark Energy Survey (DES) and the Large Synoptic Survey Telescope (LSST), should increase the sample sizes by factors of at least a few and help to confirm these results. Further development on the theoretical side is also critical — with state-of-the-art simulations now able to reproduce both the morphology distributions and the observed black hole mass function, these results can be compared to theory in a cosmological context.

Chapter 5

UKIDSS

5.1 Intro: wavelength dependence on morphology: optical and IR

Historically, visual morphological classification of galaxies has been conducted on optical images. Blue B-band images were the primary source dating back to Hubble's classic tuning-fork classification scheme (Hubble, 1926) and in the subsequent modifications by Sandage (1961) and de Vaucouleurs (1963). The more recent and larger morphological catalogs also derive their classifications from rest-frame optical images, either single-band (de Vaucouleurs (1991) (B-band), Scarlata et al. (2007) (ACS I-F814W), Fukugita et al. (2007) and Nair & Abraham (2010) (SDSS g-band)) or color-composite (Lintott et al. (2008), Willett et al. (2013) (SDSS-gri)).

In the optical regime, the flux is dominated by young, hot stars; this results in an emphasis of spiral structure in the images, but they tend to have patchy appearances due to the abundance of star-formation regions in the arms. Optical images also are impacted by extinction due to dust, which can obscure features that tend to be composed of older stellar components (such as bars and bulges). Longer wavelenths are free of these effects, making them ideal for revealing the underlying "stellar backbone" of galaxies.

It is possible, then, to consider two morphologically distinct components of a galaxy: a gas-dominated Population I disk, and a star-dominated Population II disk. The Population I disk is most easily seen in the optical, revealing HII regions, cold HI gas, and emission from young OB stars; these regions will tend to highlight flocculance in spiral structure. The Population II disk, on the other hand, traces the underlying mass distribution; consisting of the old, cooler stellar population, it is more easily seen at longer wavelengths. Block & Puerari (1999) even suggests that two separate classifications schemes should be required for all galaxies; one for the Population I disk, which can be probed in optical and ultraviolet images, and a Population II disk, for which longer wavelength images, free of dust extinction, would be required.

The extent to which the morphologies of the younger and older stellar populations are decoupled, however, is not yet clear. Early studies which directly compared optical and near-IR images found very significant differences between the two morphologies (Hackwell & Schweizer, 1983; Thronson et al., 1989; D. Block, 1991; Block et al., 1994). Block & Puerari (1999) goes as far as to pugget that there is no correlation between the two, and that the optically-definied Hubble tuning fork "does not constrain the morphology of the old stellar Population II disks." However, all of the aforementioned studies only compared morphologies of either a single galaxy, or at most a handful, so these conclusions cannot be applied generally.

The advent of larger surveys incorporating near and mid-IR detectors enabled morphological comparisons between the two wavelength regimes on a much grander scale than had previously been achieved. New results contradicted those of the previous case-studies: in general, IR morphology was found to be well-correlated with optical morphology in larger samples of galaxies. Eskridge et al. (2002) compared near-IR H-band (1.65μm) Hubble-type classifications to B-band in a sample of 205 nearby spiral galaxies from the Ohio State University Bright Spiral Galaxy Survey (OSUBSGS). Applying deVaucouler's classification system, they found an overall good correlation between the two morphologies, but on average galaxies from Sa through Scd appeared one T-type earlier in the H band than in the B band. In the IR images the bulge tended to appear more prominent and the spiral arms less knotty, which resulted in the slightly earlier classifications. For the earliest (optically S0/a and Sa) and latest-type galaxies (optically Scd through Sm), no difference in morphologies was found. This is an expected result for the earlier-types, since these have little ongoing star formation and very little dust, so it is expected that both optical and IR morphologies are dominated by old stars. This result is less intuitive for the later-type galaxies, as these are dominated by ongoing star formation. However, these galaxies are defined as having very weak or nonexistant bulges and poorly defined spiral structure. Since the main driver in the differences in morphology across wavebands was found in the intermediate spirals to be the relative prevalance of a bulge and difference in contrast and appearance of spiral arms, galaxies lacking these features should not, in fact, be expected to look different in the IR than the optical.

Buta et al. (2010) obtained similar results comparing optical and mid-IR (3.6 μm) images from the *Spitzer* Survey of Stellar Structure in Galaxies (S^{4}G, Sheth et al. (2010)) in a sample of 207 spiral galaxies. Like Eskridge et al. (2002), the optical and IR classifications were very well correlated, with the most significant differences occuring for S0/a to Sc galaxies, where the 3.6 μm were on average slightly earlier than the B-band classifications.

Infrared imaging is also often used in place of (or in addition to) optical to indentify stellar bars (e.g. Mulchaey & Regan (1997); Knapen et al. (2000); Block et al. (2004); Sheth et al. (2008)). Like bulges, bars are primarily composed of old, red stars, and therefore better traced by longer wavelengths. In fact, it is not uncommon for an infrared bar to be completely invisible in the optical. Notable examples include NGC 1566 (Hackwell & Schweizer, 1983), NGC 1068 (Thronson et al., 1989; Scoville et al., 1988), NGC 309 (D. Block, 1991), NGC 4736 (Block et al., 1994), and NGC 4303 (Figure 1, Sheth et al. (2003)). This trend is not only limited to case-studies; for example, in a larger sample of 29 galaxies classified as unbarred in the optical, *50%* of these were found to be barred in the near-IR images (Mulchaey & Regan, 1997).

The fraction of spiral galaxies which exhibit bars (defined as the bar fraction) has been measured extensively in optical images, and typically falls near 50% when bars of all strengths are considered (Sheth et al., 2008; Masters et al., 2010; Galloway et al., 2015; Consolandi et al., 2017). Since it is much more common to find an infrared bar in an optically unbarred galaxy than the reverse, it is expected that the bar fraction in the infrared will, in general, be higher than what has been measured in the optical. Some studies find a substantial increase: Seigar & James (1998) for example spectulate that "bars may always be present in disks at some level", based on finding a bar fraction of 90% when using infrared images (as compared to their optical measurement of 68%). Although their sample consisted of only 45 galaxies total, they claim this measurement should represent the general population of spirals, because their selection was not biased towards barred galaxies. Other studies report similar increases in bar fraction in the infrared, albeit not quite as large. Knapen et al. (2000) in a similar sample size of 50 galaxies find a bar fraction in the infrared of 70%, a strong increase from the optical 50%. Eskridge et al. (2000) in sample of 186 galaxies measure a bar fraction of 72% in the infrared which is *double* that of their optical measurement. While these studies report significant increases in bar fraction as a function of wavelength, they do dispute the claim by Seigar & James (1998), emphasizing that at least 30% of galaxies in their sample are truly unbarred across all wavelengths.

Other more recent studies find larger bar fractions in the infrared, not significantly so. Whyte et al. (2002) measure an increase from 72% to 79% in a sample of 72 galaxies, while Sheth et al. (2008) reports 60% for both wavelengths. MenendezDelmestre et al. (2007b) also found a slight increase from 63% to 67% in a sample of 151 galaxies, noting that although bars tended to appear stronger in the near-IR, on average they were not so weak in the optical as to become undetectable. Finally, Buta et al. (2010) also reported a similar result of 60% barred spirals, which was consistent with the fraction computed in optical RC3 classifications.

Now: segue into describing how we'll investigate these using a *much* larger sample than previously done, using GZ classifications. 2 goals: 1) investigate change in hubble-ish type in UKIDSS vs GZ2 (by looking at bulge question and arms-windyness), and 2) bar fraction, plus probably some case studies of galaxies whose morphologies change drastically.

5.2 UKIDSS sample

The UKIDSS sample is comprised of 71,052 infrared images of galaxies which had been previously optically classified in GZ2. The images were taken with the United Kingdom Infrared Telescope (UKIRT) as part of the UKIRT Infrared Deep Sky Survey (UKIDSS; Lawrence et al. (2007); Warren et al. (2007). The Large Area Survey (LAS) portion of UKIDSS covered the SDSS observations at high Galactic altitudes, allowing for full YZJHK coverage.

Morphological classifications for the UKIDSS sample were obtained via Galaxy Zoo,

UKIDSS		GZ2	
Filter	Depth (AB mag)	Filter	Depth (AB mag)
Y	21.13	g	22.2
J	20.91	r	22.2
K	20.25	i	21.3
seeing:	<1.2”	PSF width:	1.4” (median in r)
pixel scale:	0.4”	pixel scale:	0.396”

Table 5.1 Comparison of depth and resolution of the UKDISS and GZ2 images. The resolution between the two surveys is comparable, but the UKIDSS images are an average of ∼1 magnitude shallower in all bands used to create the color-composite images that where classified.

where users were shown YJK color-composite images. The classification tree used was identical to that in GZ2, allowing a direct comparison of morphologies using the same vote fractions. Raw votes were counted and weighted by user consistency in the same manner as the GZ2 sample (details of this process are given in Chapter 2).

One major challenge in comparing the UKIDSS and GZ2 morphologies is to ensure that any differences measured are mostly driven by actual morphological differences between wavebands, and not due to varying instrumental parameters. Details of the instrumentation for both samples is shown in Table 5.1. The resolution of both sets are comparible - with similar pixel size and PSF widths, the ability to resolve finer features in the images should be consistent for both. The difference in depth, however, is significant: the SDSS gri bands used to create the color-composite images in GZ2 are on average ∼1 magnitude deeper than what is achieved for the LAS YJK bands in UKIDSS. To minimize the impact the difference the difference in depth may have in comparing the two sets of images, the comparison sample is limited to the nearest and brightest galaxies. The sample is thus restricted to a volume-limit of $z < 0.06$ and $M_{r,petro} < -20.0$, which consists of 10,395 galaxies of the 54,238 with spectroscopic redshifts.

To further ensure that any observed difference in morphologies are due to physical (wavelength) dependencies, and not instrumentation, the sample is further restricted to only include galaxies for which the signal detected in the IR image extends to a

Figure 5.1 Example of a galaxy whose morphological change between optical and IR wavelengths was driven by a lack of light detectable in the IR relative to optical. This image was classified as featured and spiral in the optical using GZ2 vote factions (left), but smooth in the IR using UKIDSS vote fractions (right) (dr7objid: 587726014553587781).

significant fraction of the galaxy's total light profile. During preliminary visual inspection of side-by-side IR/optical images of the subjects, it was seen that for many of the optically-classified spirals, the arms in the IR images became so faint with respect to the bulge that there could be no fair comparison of morphologies using vote fractions. An example of this effect occured in GZ2-classified spiral galaxies which the majority voted as "smooth" in UKIDSS, due to the bulge being the only visible feature in the IR images (see Figure 5.1).

5.2.1 Method for selecting equally-sized galaxies

To identify which galaxies are sufficiently detected in both the IR and optical images, the S/N profile of the IR J-band images is compared to the r-band petrosian radius. For disk galaxies whose surface brightness distribution follows an exponential profile, 99% of the galaxy's total flux is enclosed by the Petrosian magnitude (Graham et al., 2005), which is defined as the flux measured within two Petrosian radii. Therefore, we can let $2 \times r_{petro}$ represent the radius that encloses the entire disk, which will be hereafter denoted as r^r_{2petro}. To properly compare morphologies of disk galaxies in IR and optical images, it must be ensured that a signal is detected in the J-band out to a significant fraction of that radius. This is done by computing the surface brightness profile in the J-band, and measuring the radius within which the S/N is greater than 3, which will be hereafter denoted as r_3^J. A cut is then placed on the volume-limited sample such that $r_3^J \geq 0.75 r_{2petro}^r$, which retains $\sim 60\%$, or 6,484 galaxies considered suitable for a robust morphological comparsion. The details of this process are described here.

The J-band cutouts were downloaded directly using the WFCAM Science Archive[1] . The signal to noise profiles are then computed on J-band sky-subtracted cutouts, where the sky subtraction is done using the PYTHON package PHOTUTILS BACKGROUND2D function. The noise is defined as the dispersion in the background flux, shown in the top-left panel of Figure 5.2. The background was fit to a Gaussian, and the noise was taken as the resulting standard deviation value given by the fit. The signal was computed by calculating the average flux per pixel within circular apertures of varying radii from the center of the galaxy to the edge of the cutout. From these a signal-to-noise profile was generated for each galaxy; an example is shown in the top-right panel of Figure 5.2. The radius at which the S/N profile falls below S/N=3 (or in other words, the radius within which the S/N remains greater than 3, r_3^J), is recorded for each galaxy, represented as the green dashed line. The blue dashed line is drawn at r_{2petro}^r, representing the radius containing 99% of the flux, as described above. The ratio of r_3^J to r_{2petro}^r is then used to evaluate whether the galaxy is sufficiently detectable in both wavelengths for a fair morphological comparison. The bottom row of Figure 5.2 shows the results of this method displayed on the color-composite images that are seen by GZ users. The circle on the optical image (left) shows r_{2petro}^r, and circle on the IR image (right) shows the J-band radius within which $(S/N)_J > 3$, r_3^J. In this example, $r_3^J = 0.62 \times r_{2petro}^r$, indicating that the radius at which the galaxy is detectable in the J band is only 62% that of what is visible in the r band. Given that the threshold for inclusion in the sample is $r_3^J / r_{2petro}^r \geq 0.75$, this galaxy is considered too faint in the IR with respect to the optical to fairly compare vote fractions.

Figure 5.3 shows the optical and IR images of galaxies, overlayed with circles of radii r_{2petro}^r (optical, left) and r_3^J (IR, right), sorted by the ratio r_3^J / r_{2petro}^r. For small ratios (towards top of figure) it is obvious that the IR image is much too faint with

[1] http : //wsa.roe.ac.uk : 8080/wsa/MultiGetImage_form.jsp

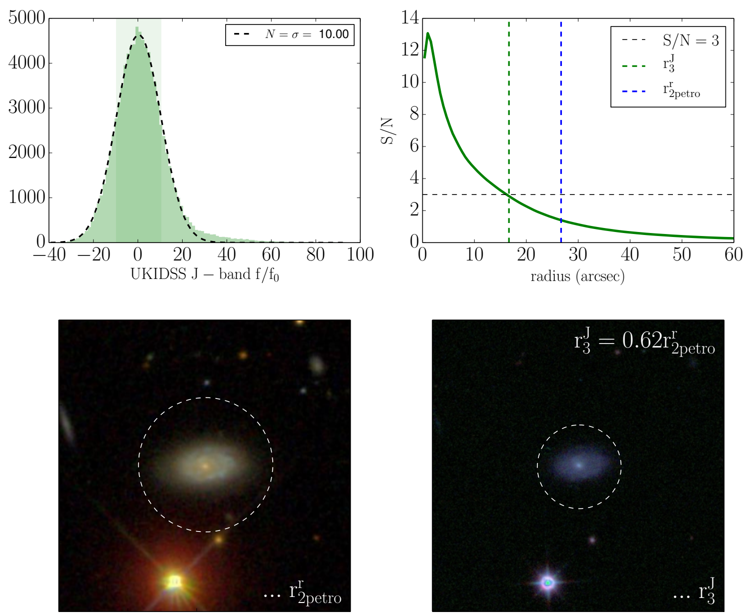

Figure 5.2 Example of the r_3^J/r_{2petro}^r calculation of one galaxy (dr7objid=587722981747392587). **Top Left**: The sky-subtracted background of the J-band images are fit to a Gaussian to derive the noise N, which is given as the standard deviation of the fit. **Top right**: The signal to noise profiles of the J-band images. The radius at which the signal-to-noise falls below three is indicated by the green dashed line, and the threshold $S/N = 3$ is indicated by the horizontal black dashed line. The blue line shows twice the r-band petrosian radius r_{2petro}^r for comparison. **Bottom**: Color-composite of the optical gri image (left) and IR YJK image (right). The dashed circles represent the radius r_{2petro}^r (left) and r_3^J (right), derived as shown in the top row. The ratio of the two radii is given, showing that for this galaxy, the light in the IR image extends to 62% of the optical image.

respect to the optical image for a fair comparison of vote fractions, while for ratios closer to unity (towards bottom of figure), the images are much more comparable. The effect of r_3^J/r_{2petro}^r on the difference in vote fractions is displayed in Figure 5.4. The left shows the distribution of the change in f_{features} vote fractions (explicitely: GZ2 f_{features} - UKIDSS f_{features}) for the optical and IR images as a funciton of r_3^J/r_{2petro}^r; the right shows the average change in f_{features} as a function of r_3^J/r_{2petro}^r. As expected, there is a much larger difference in vote fractions when the IR image does not show the full extent of the galaxy relative to the optical image (low r_3^J/r_{2petro}^r). This difference cannot be confidentely attributed to a true morphological change, but rather a limitation on the instrumentation and therefore visibility of the galaxy. Therefore we limit the comparison to galaxies where $r_3^J/r_{2petro}^r \geq 0.75$ (dashed line in Figure 5.4, right), to increase confidence that a difference in vote fraction represents a physical morphological difference between wavelengths.

5.3 Comparison of Hubble Types in Spirals

In this section the global morphologies seen in the infrared and optical are compared. As described above, the most recent studies found similar results when comparing the Hubble T-types of both wavelengths; in general, the morphologies are well-correlated, with the IR T-types being on average one T-type earlier than in the optical. The strongest difference occured for the optically intermediate-type spirals. In the most early type spirals (with very dominant bulge and very tight spiral arms), these features showed up equally well in the infrared. On the other extreme end, the very late type spirals (with almost no bulge and not well-defined arms) also showed no large change, since the relative size of the bulge and relative tightness of the arms were the main driver of the morphological differences between wavelengths. For the intermediate T-types, there was much more “wiggle room” for the bulges and arms to show more significant differences.

The first portion of this comparison will consider galaxies whose spiral arms are detected in both optical and infrared wavelengths.

As a proxy for Hubble types, the responses to the GZ Tasks related to tightness of the spiral arms and dominance of the bulge will be used, since these probe similar

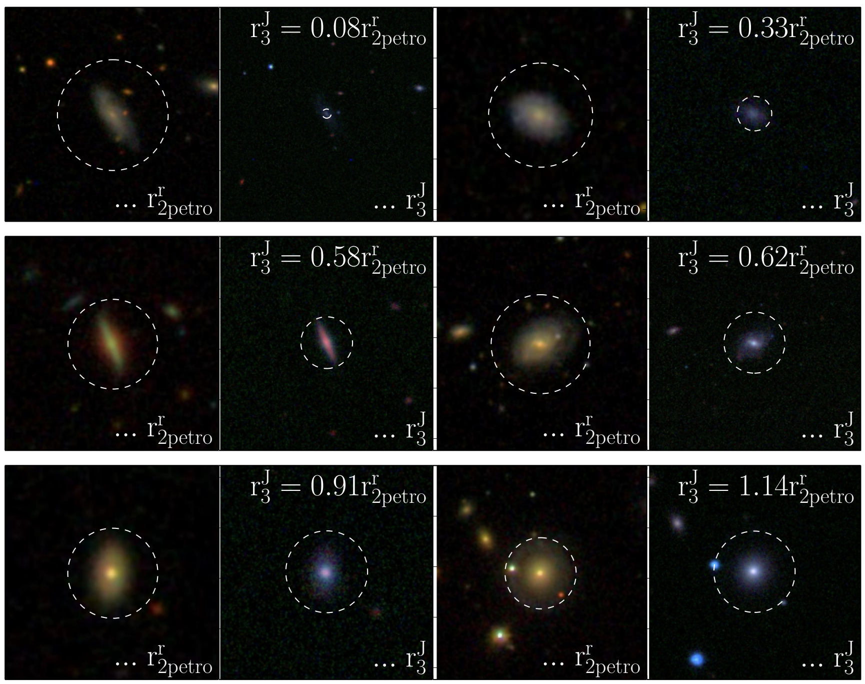

Figure 5.3 Example optical gri (left) and IR YJK (right) images of galaxies, sorted by r_3^J/r_{2petro}^r .The circle on the optical image (left) shows r_{2petro}^r, and circle on the IR image (right) shows the J-band radius within which $(S/N)_J > 3$, r_3^J.

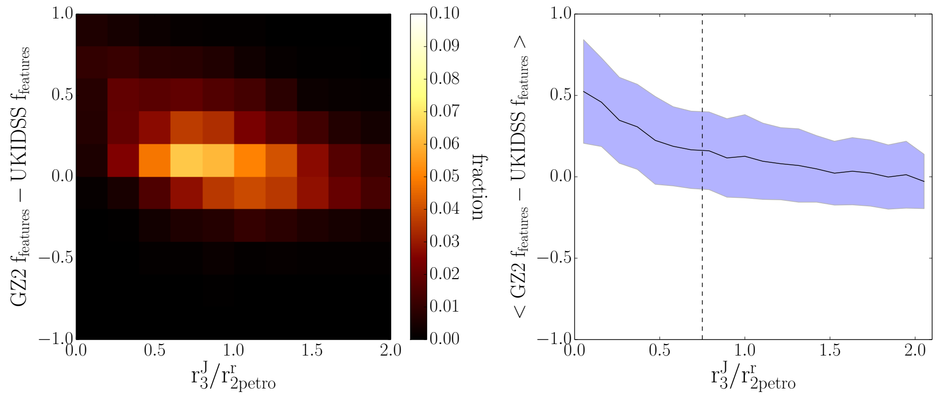

Figure 5.4 The change in GZ2 and UKIDSS vote fractions is strongest at low values of r_3^J/r_{2petro}^r, where the light detectable in the J-band extends to a significantly smaller area than than the r-band images. **Left**: Distribution of the change in $f_{\rm features}$ from GZ2 to UKIDSS as a function of r_3^J/r_{2petro}^r . **Right**: The average change in $f_{\rm features}$from GZ2 to UKIDSS as a function of r_3^J/r_{2petro}^r . The shaded region indicates the 1-σ dispersion around the mean. The dashed line at $r_3^J/r_{2petro}^r = 0.75$ indicates the threshold below which galaxies are excluded from the comparison sample, due to the coverage of light in the J-band not reaching a significant area as represented in the r-band.

features to those that influence T-type classification. The Task related to arm tightness asks, "How tightly wound do the spiral arms appear?", to which a user can choose one of three responses: "tight", "medium", or "loose". For this analysis the fraction of users who answered "tight", $f_{\rm tight\ arms}$, will be used to assess the relative appearance of the arms from optical to IR. The task related to bulge prominence asks, "How prominent is the central bulge, compared to the rest of the galaxy?" to which a user can respond "dominant," "obvious," "just noticeable," or "no bulge." For this analysis the sum of vote fractions for the first two responses $f_{\rm obv+dom}$ will be used to measure the apparent size of the bulge relative to the galaxy.

Figure 5.5 shows the difference in vote fractions for arm tightness and bulge dominance between the GZ2 optical and UKIDSS infrared classifications, as a function of optical classification. The left plot shows that on average, spiral arms have a tighter appearance in optical wavelengths: 68.7%±4.0% of spiral galaxies have lower $f_{\rm tight\ arms}$ vote fractions in the IR images. For galaxies with optically very loose arms ($f_{\rm tight\ arms} \sim 0$

or very tight arms ($f_{\mathrm{tight\ arms}} \sim 1$), the infrared classifications tend to agree. For intermediately tight optical spiral arms ($0.2 < f_{tight\ arms} < 0.8$), the UKIDSS vote fraction tends to be lower than the optical by ~ 0.3 on average. This supports the work by Eskridge et al. (2002) and Buta et al. (2010) who find slightly earlier IR classifications in intermediate-type spirals. The right panel shows the change in bulge prominance as a function of optical bulge prominence. Here the effect is even stronger: the fraction $f_{\mathrm{obv+dom}}$ is larger for the IR images in $95.8\% \pm 1.8\%$ of the galaxies, indicating the bulge is almost always more prominant in IR images than optical images. This again is in perfect agreement with studies, ie Eskridge et al. (2002), who conclude that the main drivers of the change in T-type in spirals are "the relative prevalence of the bulge and the difference in contrast and appearance of spiral arms". Here we see the same effect, and can add to the discussion that the appearance of the bulge is a stronger driver of the observed change in T-type than the spiral arm contrast. These results differ slightly than Eskridge et al. (2002) in the case of galaxies with significantly small or no bulges; in their sample, if a bulge is not detectable in one band, it generally will not be detected in the other: "Galaxies with no bulge... will not look substantially different in the near-IR than in the optical, and will thus be classified essentially the same on average." However our sample finds a small population of galaxies where this is not the case, as seen in the left-most columns of the right plot in Figure 5.5. Here little to no bulge is seen in the optical images (signified by a vote fraction $f_{\mathrm{obv+dom}} \leq 0.2$), while the IR images of the same galaxies have vote fractions up to $f_{\mathrm{obv+dom}} \sim 1$.

So far the appearance of spiral arms visible in both the optical and infrared have been compared; on average, GZ infrared morphologies are slightly earlier than the optical, a result of a looser appearance of the arms and more prominant bulges. But what of the the optically spiral galaxies whose arms disappear in the IR? Of the 959 optical spirals in the volume and S/N limited sample, 279 (29%) of these were not classified as spirals in the IR. These types will be hereafter referred to as SONIs (Spiral in Optical but Not Infrared) for convenience. The most common morphological classes of galaxies which do not exhibit spiral arms are ellipticals, S0s, and edge-on disks (which may or may not truly have spiral arms, but cannot be discerned due to orientation angle). This section will explore which of these classes SONIs tend to occupy in the IR.

Figure 5.6 shows the different pathways galaxies in the UKIDSS sample follow

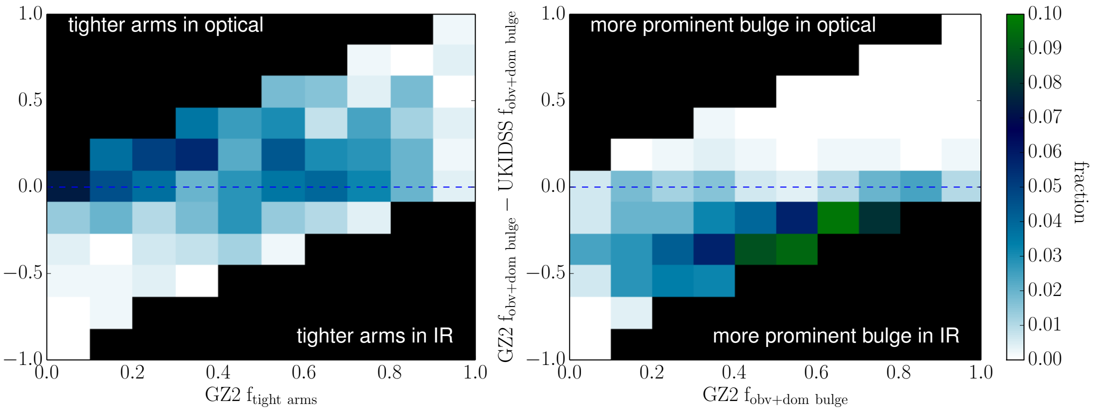

Figure 5.5 IR images of galaxies tend to have a looser appearance of arms and more prominent bulges than in optical images. Shown is the difference between optical and IR $f_{\text{tight arms}}$ as a function of optical/GZ2 $f_{\text{tight arms}}$ (**left**), and difference between optical and IR $f_{\text{obv+dom}}$ as a function of optical/GZ2 $f_{\text{obv+dom}}$ (**right**) for 502 galaxies which were classified as spiral in both IR and optical images. The colors represent the fraction of galaxies that populate any given bin, and bins which could not represent a possible difference in vote fraction ($\Delta f > f$ or $\Delta f < f - 1$) are colored black. The blue dotted line in both represents a difference in vote fraction of 0, such that galaxies above the line have larger IR vote fractions for the feature represented in each plot, respectively.

through the decision tree. The left flow diagram shows the breakdown of morphologies of all galaxies in the volume-limited sample, while the right diagram includes only the SONIs. Galaxies which follow the spiral pathway must first be classfied as featured (T00), then not edge-on (T01). At this point the not edge-on featured galaxies can follow the 'spiral' or 'not spiral' path (T03). Those marked as spirals are classified by how tight the arms appear (T09) and how many arms are present (T10). Last, both the spirals and not-spirals are classified by bulge prominence (T04). As a result of this type of decision tree, there are several pathways galaxies may take to ultimately obtain a "not spiral" classification. They may be classified from the beginning as not featured (as ellipticals or star/artifacts), or they may be featured but edge-on, or they may be featured and not edge-on, and still show no spiral arms.

The diagram on the right shows which of these paths SONIs tend to take, resulting in their ultimate classification of "not spiral" in the IR. 72% of SONIs follow the elliptical path; that is, the optically-visible spiral arms must become so faint that all that can be seen is the central bulge, which by eye becomes discernable from a full spheroidal galaxy. 19% are classified as both featured and not edge-on. One might hypothesize a majority of these exhibit stellar bars, which drives the "featured" classifications when there are no spiral arms to do so. However, there is no excess of strong bars detected; only 24% of the not edge-on featured SONIs are strongly barred, which is actually lower than that of the full sample (33%). Since the diagram flows are determined by a plurality of votes for each Task, however, the possibility of weak bars of driving the "featured" classification is not accounted for here. Therefore most of the galaxies on this path are likely either weakly barred, and/or retain evidence of both an underlying disk and a bulge, with enough contrast to keep them from being classified as purely elliptical. However it is clear that the bulge is very close to dominating the total light distribution in many of these galaxies; for SONIs, 89% are classified as having an either obvious or dominant bulge, as compared to 82% showing obvious or dominant bulges in the full sample.

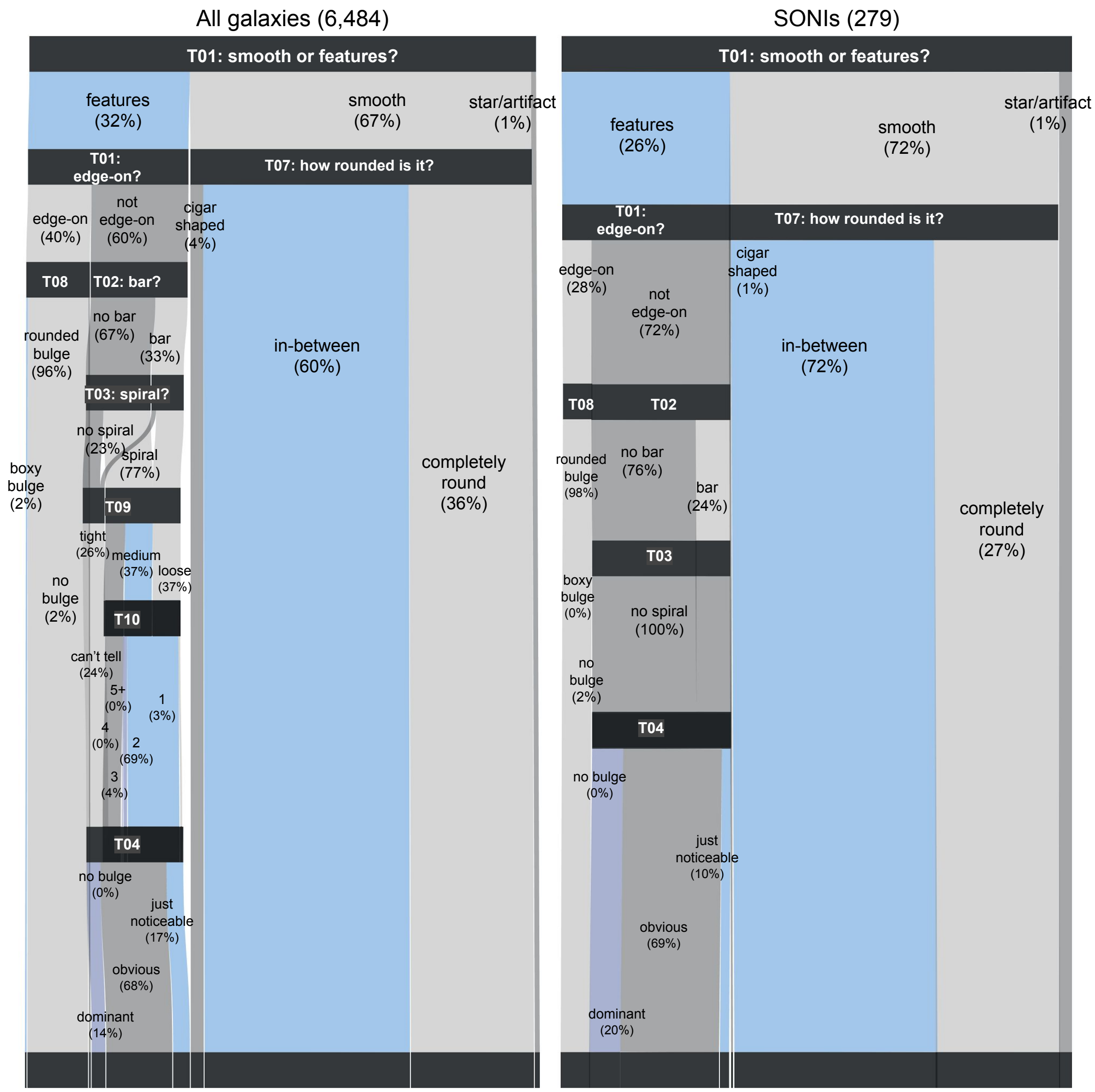

Figure 5.6 Flow diagram showing the breakdown of morphologies in the UKIDSS sample. **Left**: 15,491 galaxies in the volume-limited sample. **Right**: 2,346 SONIs: galaxies which were classified as spiral in the optical GZ2 classifications but do not follow the spiral path in the UKIDSS classifications.

Figure 5.7 Example images of galaxies which were classified as spiral in optical GZ2 classifications but followed the “smooth” path in the UKIDSS classifications.

Figure 5.8 Example images of galaxies which were classified as spiral in optical GZ2 classifications but followed the “featured, not edge-on, no spiral” path in the UKIDSS classifications.

Figure 5.9 Example images of galaxies which were classified as spiral in optical GZ2 classifications but followed the “featured, edge-on” path in the UKIDSS classifications.

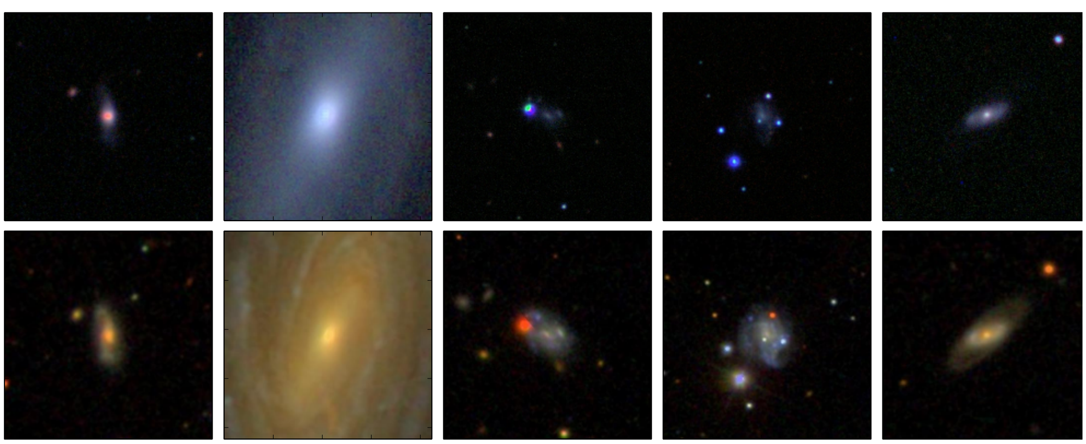

Figure 5.10 Example images of galaxies which were classified as spiral in optical GZ2 classifications but were classified as star/artifact in the UKIDSS classifications.

5.4 Bar detection

A clean separation of barred and unbarred galaxy populations is required to properly analyze the various effect bars may have on their host galaxies. If a significant portion of bars are better detected in one waveband than another, both classifications should be incorporated to improve the separation of barred and unbarred samples. This section will investigate whether this should be a necessary process for bar population studies by computing the relative numbers of bars detected in optical and infrared imaging. To avoid possible confusion in this portion of the text, two similar quanities are defined explicitely here: the *bar fraction* is defined as the ratio of barred galaxies to total galaxies in a sample, and $\mathrm{f}_{\mathrm{bar}}$ is the *bar vote fraction*, which is the fraction of users who detected a bar in an image of an *individual galaxy*.

Barred galaxies in the GZ2 and UKIDSS samples are identified using the same prescription described in Chapter 4 (Galloway et al., 2015). Cuts are placed on $f_{\mathrm{features}} \geq 0.35$ and $f_{\mathrm{notedge-on}} \geq 0.6$ to limit the sample to featured, not edge-on galaxies. An additional cut is placed on the number of people to answer the bar question $N_{\mathrm{bar}} \geq 10$ to ensure adequate statistics in calculating the bar vote fraction f_{bar}. Of the galaxies meeting these criteria, bars are then defined as present in galaxies with $f_{\mathrm{bar}} \geq 0.3$.

Figure 5.11 shows the number of barred galaxies in GZ2 and UKIDSS. Of the 1,102 total bars detected, 672 (61%) were detected in UKIDSS, and 899 (82%) were detected in GZ2. The optical data recovers a larger portion of the total bars than the IR data, yet still fails to detect 20% of them. Due to the structure of the Galaxy Zoo decision tree, there are two ways in which a galaxy would fail to achieve a bar classification: first, its bar vote fraction f_{bar} can fail to meet the threshold cut of $f_{\mathrm{bar}} \geq 0.3$; these galaxies have reached the bar question and thus are seen as face-on disks, but no bar is visible. Second, the bar question may never be asked of the galaxy in the first place if it is classified as "smooth" via the first question, or, classified as "featured" but also "edge-on" in the second. For galaxies which are classified as barred in one waveband but not the other, it may be helpful to discern via which scenerio they are changing classifications. In the first case, the images would look mostly similar in terms of the overall structure, but the bar would too weak, or perhaps even be masked, to meet the f_{bar} threshold required. In the second case, the images must transform significantly to

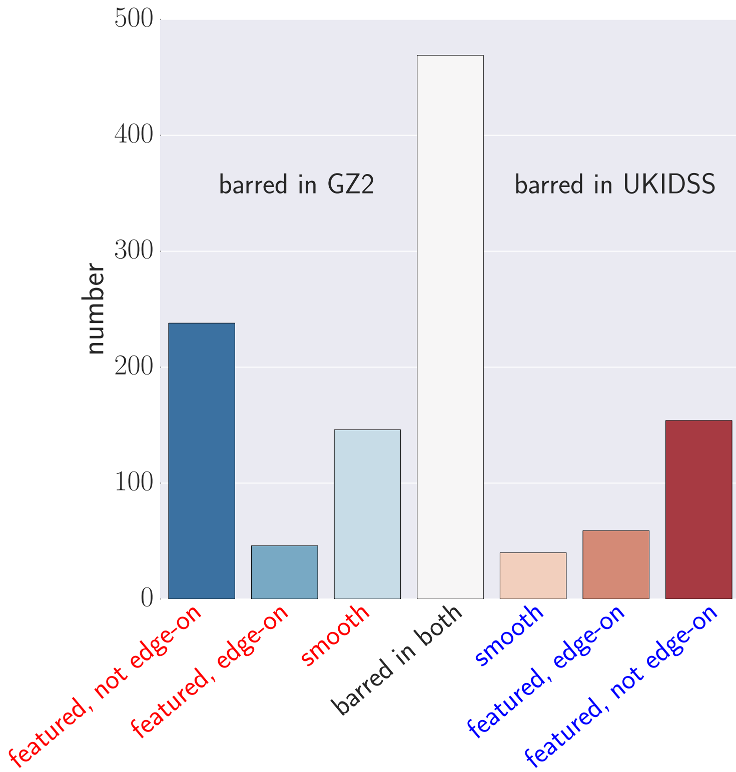

Figure 5.11 The middle bar displays the 421 galaxies which are classified as barred in both GZ2 and UKIDSS. To the left shows the number of galaxies classified as barred in GZ2 but *not* UKIDSS (blue). From left to right, these are broken down by those who changed classifications because they followed the smooth path, featured, edge-on path, and featured, not edge-on path (but with insufficient votes at the bar question to allow a barred classification), respectively. To the right shows the number of galaxies classified as barred in UKIDSS but *not* GZ2 (red). These are broken down in the same way as described for the GZ2-classified bars.

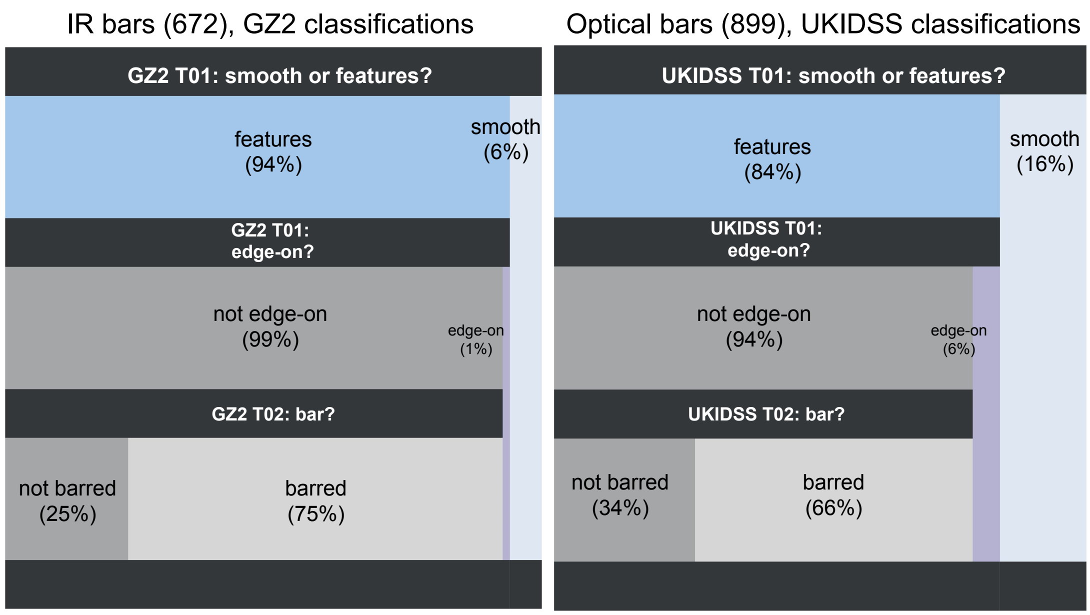

Figure 5.12 **Left**: Flow diagram of UKIDSS-barred galaxies through the first three GZ2 tasks. **Right**: Flow diagram of GZ2-barred galaxies through the first three UKIDSS tasks. Most UKIDSS-barred galaxies are classified as featured, not edge-on galaxies in GZ2. Those which change classifications to unbarred in the optical do so at the bar question; 22% of these have vote fractions lower than the threshold $f_{bar} \geq 0.3$ required for bar classification. Similar is true for GZ2-barred galaxies, although $\sim 30\%$ change classifications to unbarred in the IR because they initially follow the "smooth" path or "featured, edge-on", without making it to the bar question in the first place. Of those which reach the bar question, 25% do not achieve significant bar votes ($f_{bar} \geq 0.3$) to allow a bar classifiation.

follow entirely different paths through the tree.

Figure 5.12 shows path followed by the barred galaxies. On the left is the path of the 672 UKIDSS-barred galaxies through the GZ2 classifications, on the right is the path of the 899 GZ2-barred galaxies through the UKIDSS classifications. For the UKIDSS-barred galaxies, the majority (93%) of them maintain the same featured, not edge-on morphologies in both wavebands, but change classifications once they reach the bar question. For the GZ2-barred galaxies, a larger fraction of them change classifications earlier, with 16% of them being classified as smooth from the first question. It is also slightly more common for these galaxies to be re-classified as edge-on in the GZ2 track, but the majority (79%) are consistent in their featured, not edge-on morphologies, and 34% of these change classifications from GZ2-barred to UKIDSS-unbarred at the bar question. The numeric breakdown of these distributions is visualized in Figure 5.11, and example images for each category are shown in Figures 5.13 and 5.14.

Most galaxies which change bar classifictions do so *at* the bar question, rather than tending to follow entirely different pathways through the GZ decision tree. Here the change will be analyzed in more detail: Figure 5.15 compares f_{bar} measured in UKIDSS and GZ2 for galaxies which were consistently classified as featured and not edge-on in both samples. White dashed lines mark the threshold value for bar identification, $f_{\mathrm{bar}} \geq 0.3$. Galaxies to the right of the vertical dashed line were classified as barred in the optical images, and those above the horizontal dashed line were classified as barred in the IR images. Four regions can be defined in this way: The top right region of the plot represents galaxies classified as barred in both wavebands, the bottom right shows those which are unbarred in both, the top left shows those which are barred in the IR but not the optical, and the bottom right shows those which are barred in the optical but not IR.

The bar vote fraction f_{bar} is well-correlated in both projects. The data follow a mostly 1:1 relationship with an average scatter of $\Delta f_{\mathrm{bar}} = +/-0.1$, resulting in consistent classfications for the majority of galaxies, with 42% being barred in both and 23% being unbarred in both. 11% are barred in UKIDSS but not GZ2 (top left). These tend to not be very strongly barred in UKIDSS, with typical bar vote fractions of 0.3-0.6. Since many of these only barely pass the threshold cut, statistical error is likely a partial driver of the different classifications. 13% are barred in GZ2 but not UKIDSS; these

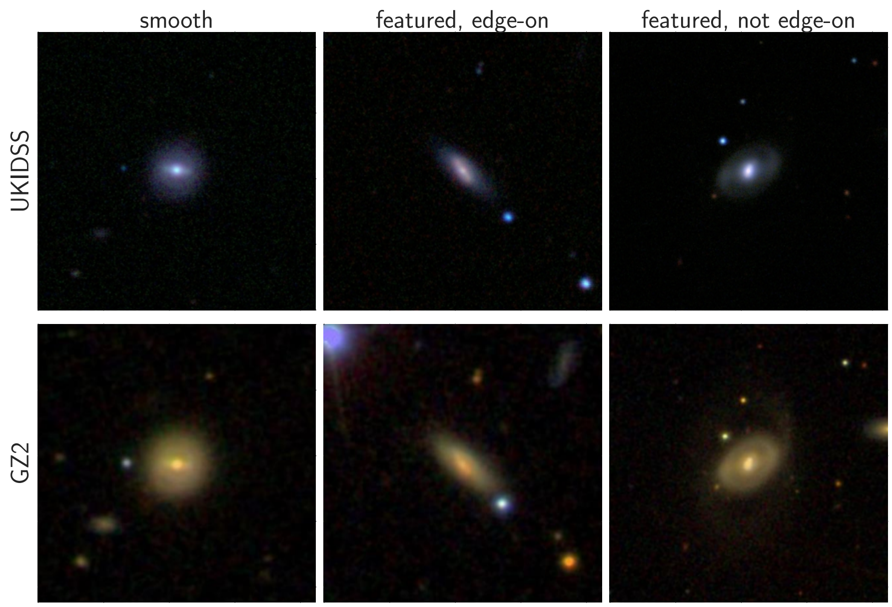

Figure 5.13 Galaxies classified as barred in UKIDSS (top row, IR images) and unbarred GZ2 (bottom row, optical images). The left column is an example of a galaxy which was not classified as barred in GZ2 because it followed the smooth GZ2 path, the middle followed the featured, edge-on path, and the right followed the featured, not edge-on path.

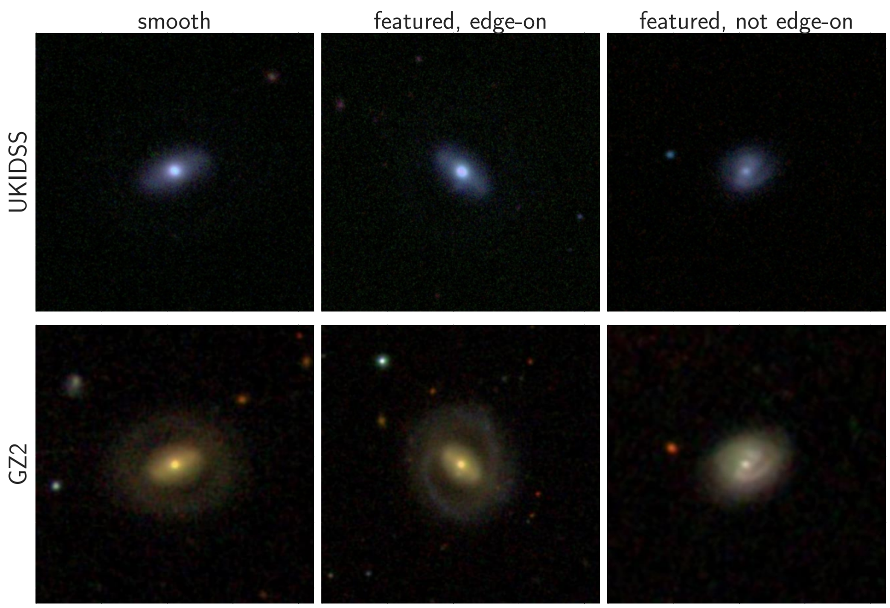

Figure 5.14 Galaxies classified as unbarred in UKIDSS (top row, IR images) and barred GZ2 (bottom row, optical images). The left column is an example of a galaxy which was not classified as barred in UKIDSS because it followed the smooth UKIDSS path, the middle followed the featured, edge-on path, and the right followed the featured, not edge-on path.

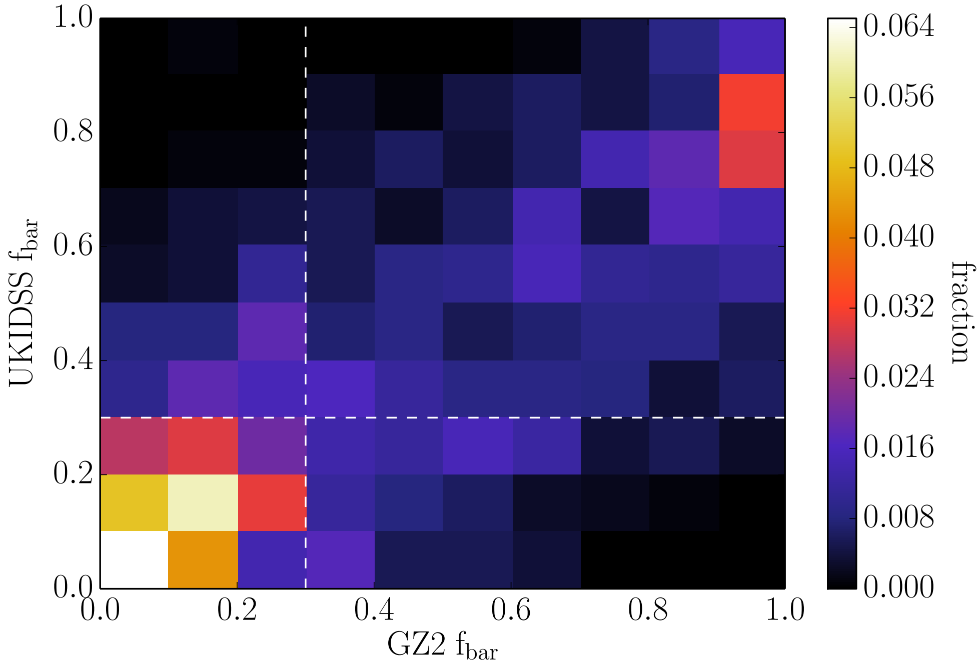

Figure 5.15 GZ2 vs UKIDSS bar strengths of 1,107 featured, not edge-on galaxies measured by f_{bar}. Galaxies shown must have 10 people answer the bar question, $f_{\mathrm{features}} \geq 0.35$ and $f_{\mathrm{not\ edge-on}} \geq 0.6$ in both samples. The dotted white lines indicate the threshold value for bar classification $f_{\mathrm{bar}} \geq 0.3$; the top-right region therefore displays the fraction of galaxies classified as barred in UKIDSS and GZ2, the bottom left are those classified as unbarred in both, the top-left are UKIDSS-barred and GZ2-unbarred, and the bottom-right are GZ2-barred and UKIDSS-unbarred. Most galaxies have consistent classifications (76% are either barred in both or barred in neither), 11% are barred in UKIDSS but not GZ2 (top left) and 13% are barred in GZ2 but not UKIDSS (bottom right).

have a wider spread of bar vote fractions in GZ2, up to $f_{\mathrm{bar,GZ2}} \sim 0.9$. This change is much more drastic, indicating that the change in classifications in these cases is more driven by a significant differences in the appearance of the images.

5.5 Discussion

This chapter has compared UKIDSS and GZ2 classifications for 6,484 bright, nearby galaxies whose J-band light profiles extended to a significant portion of those in the r-band. UKIDSS galaxies tend to have lower f_{features}, $f_{\mathrm{tight\ arms}}$, and larger $f_{\mathrm{obv+dom\ bulge}}$ vote fractions, corresponding to slightly earlier-appearing morphologies (or lower T-type). Only 43% of the total bars in the sample were detected in both GZ2 and UKIDSS; the remaining were detected in GZ2 but not UKIDSS (39%) or UKIDSS but not GZ2 (18%).

5.5.1 Changes in spiral structure

Comparisons of optical and infrared morphologies were motivated under the hypothesis that the flocculant appearance of star-forming regions and effects of dust-obscuration may mask the structure of the underlying older stellar populations. This is a reasonable assumption; morphology is a tracer of the light distribution in a galaxy, which may or may not be completely correlated with the mass distribution. Most of a galaxy's mass is encompassed by older, cooler stars. In optical imaging, the flux may be dominated by light from a smaller contribution of young, hot stars, which could skew the morphology if it differed significantly from the older population; perhaps even justifying two separate morphological classification systems for the different stellar types. Whether this difference tends to be significant has been difficult to confirm observationally, as even the largest samples for comparison have only consisted of a couple hundred galaxies (Eskridge et al., 2002; Buta et al., 2010). This comparison study has strong advantages in a sample size over an order of magnitude larger than those previously done, as well as an advantage in statistical significance for each morphology due to the crowd-consensus nature of the citizen science classifications, whereby each galaxy is seen by many volunteers. Complications are introduced, however, given the structure of the decision tree used in this type of classification (discussed in Section 5.5.3).

Galaxies with identifiable spiral structure in both samples appeared slightly earlier in Hubble type in infrared images than the optical images, which is in perfect agreement with the findings of Eskridge et al. (2002) and Buta et al. (2010). The lack of contrast provided by star-forming regions in the optical gave the infrared image a more smoothed-out appearance, which caused spiral arms present to appear looser, resulting in lower $f_{\text{tight arms}}$ fractions. Additionally, the central bulge of the disk galaxies was much more dominant in the infrared images, as expected due to the older stellar compositions.

In the case of SONIs, these features could not be compared because spiral arms were not identified at all in the infrared images. This problem was mainly driven by the structure of the decision tree - 79% of these optically-classified spirals did not even reach the question that asks to identify spiral arms (Task 03); 72% of which followed the "smooth" path from the beginning. Visual inspection of these cases showed a common contributer to this class: in these spirals, the bulge was often so dominant that the arms appeared extremely faint by comparison. While often still technically visibile, they might not have been obvious to the eye unless pointed out (see the center panel of Figure 5.7 for an example). In others, however, it seemed that the contrast provided by star-formation, as in the optical images, is necessary to identify the presence of arms within the disk. Therefore it may seem that, contrary to previously hypothesized, star formation regions aid in rather than hinder visual inspection for morphological classification.

5.5.2 Changes in bar classification

Galaxies classified as featured and not edge-on were consistent in bar vote fractions f_{bar}, with 75% agreement in bar classification. Strong bars detected in one survey were just as easily detected in the other, in agreement with Whyte et al. (2002); Sheth et al. (2008); MenendezDelmestre et al. (2007b). This study however finds many more examples of bars which are only detected in one: of the featured, not edge-on galaxies, these examples tend to be weaker bars that are only just noticeable in the images, and only just meet the threshold $f_{\text{bar}} \geq 0.3$ in the survey in which they are detected, and only just below in that which they fail. Therefore these changes of classification tend to only occur in weak bars, and likely are driven partially by minimal contrast in the images and partially by simple statistical error. A small fraction of galaxies (7%) did

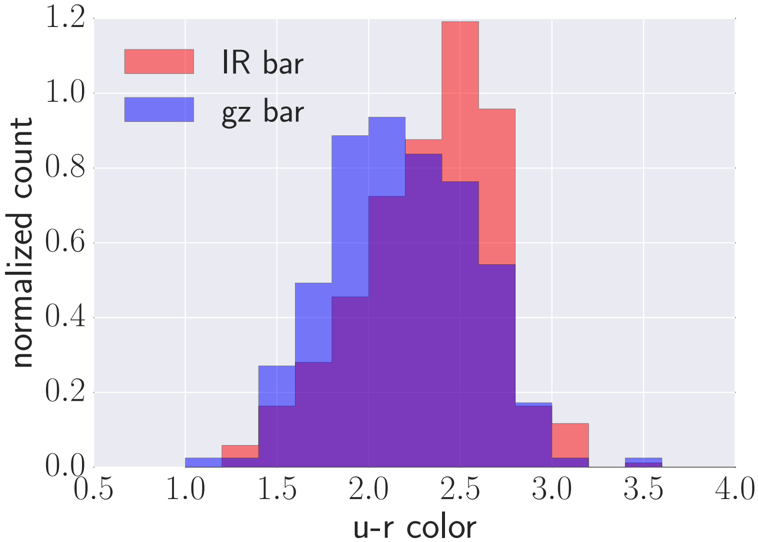

Figure 5.16 u-r colors of 203 galaxies with bars detected in UKIDSS but not GZ2 (red) and 430 galaxies with bars detected in GZ2 but not UKIDSS (blue). The bars detected in the infrared but not optical images have redder colors than those detected in optical, suggesting dust obscuration may play a role in increasing the difficulty in visually identifying bars in optical images. A two-sided KS test yielded a p-value $p < 0.01$ for the color distributions of the two categories, rejecting the null hypothesis that the samples were drawn from the same distribution.

change morphology from unbarred in UKIDSS to barred in GZ2 via a significant change in vote fraction $\Delta f_{\mathrm{bar}} > 0.3$; in these cases the bars did appear strongly in the infrared images, but their relative appearance with respect to the spiral arms was such that the bar appeared as the dominant structure in the galaxy, rather than just a component (see example in Figure 5.13, right panel). These cases were uncommon, but yet another example of the lack of contrast provided by SF regions creating difficulty in identifying substructures.

43% of the total galaxies which changed bar classifications did so because they did not reach the bar question in one survey or the other. 66% of these were barred in GZ2 and followed alternate paths in UKIDSS, while 34% were barred in UKIDSS and followed alternate paths in GZ2. Both, albeit in different ways, support the hypothesis that bars are more visible in the infrared. The latter case describes galaxies whose bars appear very strong in contrast to the disk, while in the optical the edge is less sharp, possibly due to dust obscuration, suggested by the fact that the galaxies in this category are redder on average (see Figure 5.16). Examples of these are shown in the left and middle panels of Figure 5.13. The former category, in which GZ2-barred galaxies follow the smooth or edge-on path in UKIDSS, is an example of this effect at an extreme level. Here, the bar is still strong and visible in the IR images, but overwhelmingly so, to the point that the rest of the disk and arms are no longer also visible. This produces images of isolated bars, which look like elongated smooth galaxies or edge-on disks; the difference relying on how well-defined the central bulge appears. See the left and middle panels of Figure 5.14 for examples of this effect.

5.5.3 Task 01: smooth or features

One of the primary complications of this study has been the inability to directly compare vote fractions f_{bar} and f_{spiral} because of the many galaxies which follow alternate paths through the decision tree in each project, beginning with Task 01. This question, which asks, "Is the galaxy smooth and rounded, with no sign of a disk?" was originally placed at the top of the tree to separate spheroidals from galaxies with features. This way, volunteer effort would not be wasted going through the numerous Tasks pertaining to features that are not found in ellipticals. For optical images, this question has performed adequately in separating featured from ellipticals Willett et al. (2013). For infrared images, however, everything looks "smoother" to an extent, even when features are present. This chapter has presented several examples of UKIDSS galaxies which are clearly not elliptical, but do have a rather smooth appearance. Perhaps this particular wording of the question in Task 01 is inappropriate for infrared image sets, since "smooth" encompasses a broader definition than spheroidal for these in particular. An alternative approach for classifying future infrared datasets would be to first separate the sample in advance by those which were optically classified as smooth and featured, and require that all featured questions be asked for galaxies in the optically-featured sample, even if "smooth" was chosen for Task 01. This would help ensure that higher-tier Task vote fractions could always be properly compared between the two, without completely abandoning the decision-tree format.

The strong correlation between vote fractions of the optical GZ2 and infrared UKIDSS morphologies indicate that older stellar populations trace mostly the same light distributions astheir younger counterparts; this negates the notion (Block & Puerari, 1999) that separate classification schemes are necessary when considering galaxy morphology. As to whether IR images aid in revealing the "stellar backbone" structure, this analysis suggests this is true, albeit with some caveats. While SF regions can dominate the flux in optical images and affect the overall appearance, a similar effect seems to take place in the IR. UKIDSS images were often so dominated by the flux from older populations in the bars and the bulge that the rest of the disk became hidden as a result; in these cases, the utilization of IR to find bars can be countereffective. Deeper imaging is thus crutial for future comparisons. However, there were sufficient examples in which the infrared images detected a bar where the optical images did not, but mostly for weak bars. Based on these results, it is strongly recommended that both wavebands are utilized in studies for which detecting bars of all strength is required.

5.6 Conclusions

The main findings of this analysis are as follows:

- For galaxies whose spiral arms are detected in both optical and IR images, the IR classifications are slightly earlier than the optical, driven mostly by a stronger appearance of the bulge and partly by a looser appearance of spiral arms.

- A significant fraction (29%) of galaxies were classified as having spiral arms in the optical images but not the infrared images. The majority of these (72%) instead appeared smooth, 7% appeared featured but edge-on, and 19% appeared featured and face-on.

- For galaxies which can be identified as featured and not edge-on, a majority of 76% galaxies have consistent barred or unbarred classification in optical and infrared classifications. Galaxies which were barred in UKIDSS but not GZ2 tended to be weakly so, such that statistical error is likely the driving factor between the mis-matched classifications. It is more common for bars to be detected in GZ2 but not UKIDSS due to genuine differences in the images, where separation between features were more distinct in the optical and smoothed-over in the IR.

- 57% of the total bars in the sample were found in one project but not the other; therefore it is suggested that studies analyzing the effect of bars use both wavebands for detection when possible.

Chapter 6

GZH red disk fraction

This chapter is in preparation for submission in the Monthly Notices of the Royal Astronomical Society.

Passive, red disks are an unconventional class of galaxies. They do not adhere to the standard bimodality of the color-morphology relationship, whereby most galaxies tend to exist in one of two populations: blue, late-type disks exhibiting active star formation, and red, early-type ellipticals showing little to no signs of recent star formation (Strateva et al., 2001; Baldry et al., 2004; Correa et al., 2017). The division between the two populations is particularly apparent when represented visually on a color-magnitude or color color diagram. Galaxies tend to populate in two distinct regions: the "red sequence" in the upper band, which contains predominantly early-type galaxies, and the "blue cloud" in the lower, containing mostly late-type spirals. This relationship has been shown to hold for $\sim>$ 85% of galaxies out to z $\sim$ 1 (Bell et al., 2004; Cirasuolo et al., 2007; Mignoli et al., 2009) and possibly beyond (Giallongo et al., 2005; van Dokkum et al., 2006; Franzetti et al., 2007; Cassata et al., 2008).

The relatively tight correlation between galaxy color (which traces the stellar content) and morphology (which traces dynamical history) suggests an evolutionary link between the two. In the simplest interpretation, it could be deduced that galaxies tend to begin their lives as young, star-forming disks, until some mechanism (secular or external) causes star-formation to cease while the galaxy simultaneously undergoes a morphological transformation from disk to spheroidal. The growing evidence for a significant population of galaxies which breaks this relationship, however, insists on more nuanced interpretations of this model.

The passive disk population has been a matter of interest for understanding the mechanisms driving the evolutionary link between color and morphology since their initial discovery. In one of the earliest documented reports of this class, van den Bergh (1976) identified a set of spirals in the Virgo cluster which were forming stars "much less vigorously" than the other galaxies of the same type, which were dubbed "anemic spirals". Analysis of this population suggested the possibility of "gentle" quenching mechanisms which could shut off star-formation without disrupting the morphology (in contrast to violent processes such as mergers, which are capable of destroying the disk (Bell et al., 2004; Negroponte & White, 1983; De Lucia et al., 2006; Springel et al., 2005)). The low gas content in the anemic spirals suggested that subtle environmental factors played a role in stripping the gas required to continue star-formation, a process commonly known now as ram-pressure stripping (Gunn & Gott, 1972; Steinhauser et al., 2016).

Other studies have since investigated other possible mechanisms could lead to the formation of passive disks, and how significant of a contribution this population makes to understanding the full picture of galaxy evolution. Environment is believed to play a strong role in thier formation; many studies for instance find passive spirals preferentially in high-density environments (Dressler et al., 1999; Poggianti et al., 1999; Goto et al., 2003; Deng et al., 2009; Hughes & Cortese, 2009). Moran et al. (2006) model the star-formation histories of passive spirals at $z \sim 0.4$ and find them to be consistent with models for spirals affected by gas-starvation (Larson, R.B., Tinsley, B.M. and Caldwell, 1980; Quilis et al., 2000; Bekki et al., 2002). Environment plays a significant factor in this scenerio, wherby the interaction of the galaxy with the intra-cluster medium halts the accretion of gas onto the galaxy, inhibiting star-formation and causing a quench without disrupting the morphology significantly. Their results did not argue that starvation was the only mechanism responsible for building up the population of disks in the red sequence, but do conclude that passive disks are indeed an important transition population.

Masters et al. (2010) is one of the few studies which finds no strong correlation of passive disks with environment, but do not rule out environment playing a significant contribution in their creation. They also find strong evidence for quenching via completely secular processes; given by their sample of passive disks being more massive and having a higher bar fraction than their star-forming counterparts. Massive galaxies are more likely to have been assembling for very long times, allowing sufficient time to use up all of their gas, without environment being a direct factor. This option could explain the observed correlations with density and passivity, given that higher-density regions were more likely to have been assembled at earlier times. Secondly, Masters et al. (2010) observed a significantly higher bar fraction in passive spirals (67%) than star-forming spirals (27%). Bars are known for their ability to efficiently drive gas to the centers of galaxies via a redistribution of angular momentum throughout the disk (Sellwood & Wilkinson, 1993; Shlosman et al., 1989; Ann & Thakur, 2005), which could increase central star-formation (Hawarden et al., 1986; Ho et al., 1997) or feed the central supermassive black hole (Athanassoula, 1992; Friedli & Benz, 1993). The excess of bars in passive disks then suggests that bars were responsible for quickly using up the gas in the galaxy, resulting in subsequent quenching.

Passive disks have thus far been proposed as both a final stage of galactic evolution, driven by secular and external processes capable of exhausting gas required for star-formation, and as a transition phase of galaxies toward a final evolution to red spheroidal, driven by processes which quench and morphologically transform on different timescales, or multiple separate processes acting independently. Understanding the significance of the passive disk population is therefore unquestionably an important key to understanding galaxy evolution as a whole. Bundy et al. (2010) investigates this subject by measuring the different morphological contributions to the red sequence since $z = 1$, and estimate as high as 60% of all galaxies go through a passive disk phase. It was not quantified which of these further evolve to spheroidal and which stay disks for the remainder of their lifetimes, but the decaying contribution of passive disks to $z = 0.3$ was evidence that some fraction of these did indeed transform to elliptical.

This paper will investigate the evolution of the passive disk population from $z = 1$ to $z = 0.3$ using galaxies identified in the COSMOS field with morphological classifications from Galaxy Zoo: Hubble. We will measure the fraction of disks which are passive and the fraction of the red sequence occupied by disks as functions of mass and redshift, and argue that three factors drive the evolution of these fractions: 1) the rate of blue disks quenching to form passive disks, 2) the rate of blue disks quenching and simultaneously transforming to elliptical, 3) the rate of red disks transforming to red ellipticals, and 4) the net merger rate of ellipticals. We will implement a simple toy model to simulate the evolution of the relative abundances of red disks, blue disks, and red ellipticals, in order to quantify these rate parameters. We will use the results to estimate the fraction of galaxies that enter a red disk phase, and discuss the likelihoods of the red disk phase being a transitory stage or an end-point of a typical galaxy's evolutionary path.

Section 6.1.1 will describe our methods for selecting disk galaxies and separating the sample into active / passive populations using a color-color diagnostic. In Section 6.2 we describe a new method of correcting for redshift bias in the detection of disk galaxies with Galaxy Zoo classifications using an artificially-redshifted set of images. In Section 6.3 we present our results of the fraction of disk galaxies which are red, and the fraction of red sequence galaxies that are disks, as functions of mass and redshift. Here we also explain our toy-model for measuring the dominant evolutionary pathways taken by galaxies in different bins of mass. We compare our findings with results from the literature and discuss their implications in Section 6.4. Our main conclusions are outlined in Section 6.5. We adopt a ΛCDM cosmology throughout this paper of $\Omega_m = 0.31$ and $H_0 = 68$ km s^{-1}Mpc^{-1} (Planck Collaboration et al., 2015).

6.0.1 Quenching Mechanisms

An isolated galaxy will eventually cease to form new stars as it naturally exhausts its limited supply of gas. The time-scale for complete consumption can be estimated from the amount of gas in a typical galaxy and the rate at which it is consumed through star formation: $\tau \sim M_{gas}/\dot{M}_{gas}$ (Larson, R.B., Tinsley, B.M. and Caldwell, 1980), and is expected to range from 1-3 Gyr. Most galaxies do not exist in such isolation; the exchange of matter in the galaxy due to its surroundings can disrupt and often accelerate the depletion of a galaxy's gas reservoir. Quenching is defined as any process which drives the shutting-down of star formation in this way. This section will introduce different proposed quenching mechanisms, some of which are internal (driven by the galaxy's structure or components), or external (driven by direct influence of the surrounding environment).

Ram Pressure Stripping

As a galaxy moves through the intracluster medium (ICM), it experiences ram pressure $P_{ram} = \rho_e v^2$, where ρ_e is the density of the ICM and v is the velocity of the galaxy (Gunn & Gott, 1972). The force per area required to hold gas onto the traveling galaxy is $F/A = 2\pi G \sigma_s \sigma_g$, where σ_s and σ_g are the star and gas surface densities, respecitively. If a galaxy is moving fast enough, or the ICM density is large enough, the ram pressure can exceed this force and consequently rip the gas from the galaxy; this process is known as ram pressure stripping. Evidence of this effect is seen observationally in asymmetries of the disk in spirals (a common example is NGC 4402, which has a bowed appearance and a one-sided concentration of dust, believed to be the effects of the galaxy struggling to hold onto gas on the outer regions of the disk) and truncated radial density profiles. Simulations (Steinhauser et al., 2016) show that extreme cases of ram pressure stripping can completely strip a galaxy of its cold gas, causing a rapid quenching on timescales of a few hundred Myr. More mild cases, on the other hand, can actually temporarily increase star formation, which quickly uses up the available cold gas, and eventually quenches the galaxy on timescales similar to natural isolation, ~ 1 Gyr. Fillingham et al. (2016) find a mass dependence on the efficiency of this process: they find RPS to be very efficient and rapid for galaxies $M_* = 10^{8-9} M_\odot$ for a range of halo host properties, suggesting RPS may be the dominant quenching mechanism for low-mass galaxies.

Strangulation and Harassment

Even if the ram pressure exerted by the ICM is not strong enough to completely remove all of the gas from a galaxy, it may be just strong enough to strip the outer hot gas which would have otherwise cooled and replenished the cold gas reservoir. This process is appropriately defined as strangulation, where star formation ceases after the inital cold gas is used up (Larson, R.B., Tinsley, B.M. and Caldwell, 1980). More frequent and violent encounters can increase star-formation in a similar process known as harassment (Moore et al., 1996). These can lead to a compression of the cold gas causing a temporary and intense burst of star formation, depleting it completely on a time scale of ∼1-2Gyr (Kawata & Mulchaey, 2007). Moore et al. (1999) show through simulations that harassment can be powerful enough to alter the morphology of low-mass, low-surface brightness galaxies.

AGN feedback

AGN are believed to play a strong role in the regulation of star-formation in their host galaxies via AGN *feedback*, whereby accretion onto the central SMBH generates strong outflows of energetic material and hard radiation; these AGN-driven winds may then terminate star-formation by heating the gas or expelling it completely from the galaxy. This effect was first proposed as an important quenching mechanism through the development of theoretical models aiming to reproduce the observed local-Universe luminosity function. The bright end, where there is a sharp break in the observed number density of highly luminous galaxies, tends to only be reproducable in models which incorporate AGN feedback to suppress star-formation as galaxies build up their mass (Benson et al., 2003; Di Matteo et al., 2005; Bower et al., 2006; Croton et al., 2006; Somerville et al., 2008). One of the leading observational arguments for this effect is the high fraction of AGN in the green valley (Martin et al., 2007b; Schawinski et al., 2010), suggesting that AGN may be responsible in part for transitioning galaxies from the blue cloud to the red sequence. Smethurst et al. (2016) found strong evidence for rapid and recent quenching through an analysis of star formation histories of a large population of AGN hosts, indicating that AGN-feedback can play a strong role in the quenching process.

Mergers

Mergers are a well-known driver of quenching (Peng et al., 2010), and are perhaps the dominant mechanism in particular for central galaxies Smethurst et al. (2017) whose dense environments give an increased probability of galaxy-galaxy interaction. Simulations demonstrate that these events cause a mechanical disruption of the merging disks (Pontzen et al., 2017) which triggers powerful, brief starbursts (Barnes & Hernquist, 1996; Hopkins et al., 2006), yielding star formation rates up to twice that observed for their isolated counterparts (Mihos & Hernquist, 1994), resulting in a quench after the gas required for star formation is rapidly depleted. Major (1:1 mass ratio) events have been shown to strongly disrupt the morphology of the interacting galaxies. It is hypothesized modern-day ellipticals were primarily formed from the mergers of disk galaxies (Toomre, 1977; Schweizer, 1982; Schweizer et al., 1990), which has been supported both by simulations (Mihos & Hernquist, 1996; Pontzen et al., 2017) and observations (Schweizer, 1982; Wright et al., 1990; Stanford & Bushouse, 1991), whereby recently-quenched galaxies were shown to follow $r^{1/4}$ light profiles.

6.1 Sample Selection

The parent sample of galaxies in this paper is drawn from the Galaxy Zoo: Hubble (GZH) catalog (Willett et al., 2016), which provides morphological classifications for galaxies sourced from the HST Legacy Surveys. From the main catalog we select galaxies with imaging from the Cosmic Evolution Survey (COSMOS, Scoville et al. (2007)) in the redshift range $0 < z < 1$. Rest frame NUV-r and r-J colors are taken from the UltraVISTA catalog (McCracken et al., 2012; Ilbert et al., 2013).

6.1.1 Data

We identify a sample of 14,663 disk and elliptical galaxies using the morphological classifications provided by GZH. Mergers and irregulars are excluded from the analysis by applying cuts of $\mathrm{f}_{\mathrm{irregular}} > 0.3$ and $\mathrm{f}_{\mathrm{merger}} > 0.5$ for galaxies which have at least 20 "yes" votes for the question, "Is there anything odd?". Last, we apply an inclination limit using $f_{\mathrm{not\ edge-on}} > 0.3$ and $N_{\mathrm{not\ edge-on}} > 10$. Before applying this cut, it was observed that the red sequence region of the sample was dominated by highly-inclined galaxies, shown in Figure 6.1. Given that galaxy color should be independent of the angle in which it is observed, it is clear that the inclined galaxy colors are strongly affected by dust-reddening. While we are not using dust-corrected colors in our color-color separation, inclination has shown to have an affect on colors even in those which dust-corrected has been attempted (Morselli et al., 2016; Devour & Bell, 2017). By limiting the sample to face-on galaxies, this bias should be removed (right panel of Figure 6.1).

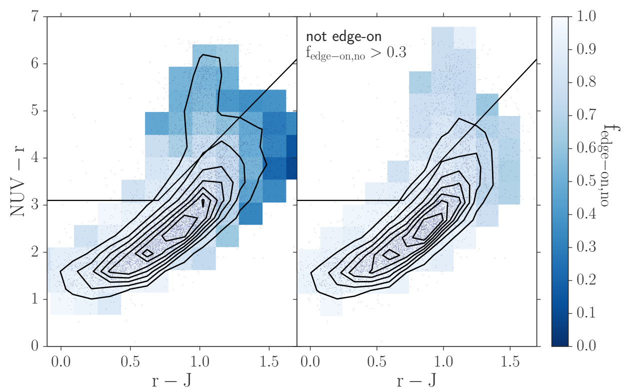

Figure 6.1 The effect of reddening for highly inclined galaxies. On the left panel is the distribution of $f_{\mathrm{edge-on,no}}$, which is the fraction of Galaxy Zoo users who voted "no" in response to the question "Could this be a galaxy viewed edge-on?". This vote correlates with inclination angle, such that low values represent highly inclined galaxies, and high values represent face-on galaxies. The bins are colored such that darker blue bins have a higher fraction of highly inclined galaxies, and white bins have high fractions of face-on galaxies. There is an obvious bias towards redder colors for galaxies with high inclination angles (low votes for $f_{\mathrm{edge-on,no}}$). We therefore implement a cut of $f_{\mathrm{edge-on,no}} > 0.3$ to ensure that observed red colors are an indicator of a lack of star-formation, and not dust-reddening.[Note: I'm not sure the right panel is particularly useful; it's really just showing the distribution is mostly smoothed out after setting the cut. Keep?]

To classify the galaxies as quiescent or star-forming, a method similar to that described by Ilbert et al. (2013) (hereafter I13) was used, which implements a rest-frame NUV-r versus r-J diagnostic. Here are some reasons these colors are great (NUV-r:) (Arnouts et al., 2007; Salim et al., 2005; Wyder et al., 2007),(Martin et al., 2007a)

The demarcation line to separate the quiescent and active populations at $z = 1$ is adopted from I13, which defines the quiescent galaxies as those which satisfy: $M_{NUV} - M_r > 3(M_r - M_J) + 1$ and $M_{NUV} - M_r > 3.1$. I13 applies this criteria to all galaxies in a range of $0.2 < z < 3$, although it performs best at separating the two populations in the redshift bin $0.7 < z < 1.2$, where $> 98\%$ of galaxies identified as quiescent exhibited star formation rates less than $log(SFR) = -11$ (see Figure 3 of I13). Therefore this work uses the I13 separation criteria at $z = 1$, and computes the evolution of the demarcation lines as a function of redshift to $z = 0$.

The evolution of $r - J$ and $NUV - r$ colors was measured using a stellar population synthesis model from Bruzual & Charlot (2003). An instantanious-burst model (ssp) was chosen from the Padova1994 track to represent the color evolution of a passively evolving galaxy, with a metallicity $Z = 0.008 = .4Z_{\odot}$, which is the typical metallicity of passive galaxies with mass $9 < log(M_*/M_{\odot}) < 10$ (Peng et al. (2015), Figure 2a), chosen to correspond to the median mass of the sample ($log(M_*/M_{\odot}) = 9.7$). A linear fit was geenerate for each color within the range $0 < z < 2$, and the slopes for each were used to redefine the demarcation lines in five redshift bins: one with central value $z = 0.007$ (used to classify the SDSS ferengi2 sample), and four with central values $z =$ [0.30,0.50,0.70,0.90] with widths $\Delta z = 0.2$. The quiescent galaxies are thus defined in these bins as those that satisfy:

$$M_{NUV} - M_r > 3.1 + a_1(z) \tag{6.1}$$

$$M_{NUV} - M_r > 3(M_r - M_J + a_2(z)) + a_1(z) + 1 \tag{6.2}$$

where $a_1(z) = [0.54, 0.38, 0.27, 0.16, 0.05]$ and $a_2(z) = [0.19, 0.14, 0.10, 0.06, 0.02]$.

We note that the evolution of the demarcation lines from $z = 1$ to $z \sim 0$ is very minimal, and our final results do not change if we perform the separation using static lines.

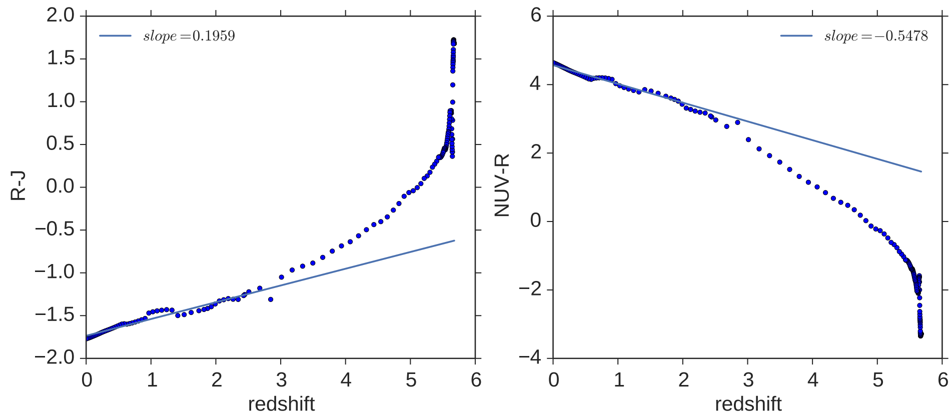

Figure 6.2 Evolution of colors using stellar population synthesis models. Galaxy was assumed to have formed at $z = 6$ for plotting purposes.

In describing our methods for separating active and passive populations using a color-color separation technique, we have used terminology such that blue/red have been used to describe colors explicitely, while active/passive have been used to describe ongoing/quenched star-formation. The remainder of this paper will assume that the color cuts described in this section adequately separated the active and passive populations, and for convenience the terms red/blue will be used interchangeably with passive/active.

6.2 Correcting for Incompleteness in Disk Detection

In this work, we study the growth of the red sequence population by evaluating the fraction of passive disks as a function of redshift, $\mathrm{N_{red\ disks}}/(\mathrm{N_{red\ disks}}+\mathrm{N_{blue\ disks}})$, as well as the fraction of disks occupying the red sequence, $\mathrm{N_{red\ disks}}/(\mathrm{N_{red\ disks}} + \mathrm{N_{red\ ellipticals}})$. To accurately measure these fractions, the number of disks populating each redshift interval must be known with confidence. To identify disk galaxies in our sample, we set a cut of $f_{\mathrm{features}} \geq 0.3$, such that galaxies meeting this criteria are considered to have distinguishable features or disk structure (additional cuts are also placed to eliminate clumpy, highly inclined, and merging galaxies; see Section **??**). However, it is known that distinguishing disk structure from spheroidal becomes increasingly challenging at high redshifts (for both experts and novice classifiers alike), where features are less resolved and more difficult to identify. Willett et al. (2016) show using a set of artificially-redshifted simulated galaxy images classified in Galaxy Zoo that vote fractions for the same galaxy can be drastically different measured at $z = 1$ from $z = 0$, often enough to change its morphological classification (we will show the same in Section 6.2.1). Therefore it is predicted that applying a f_{features} cut to identify disks will increasingly underestimate their true number at increasing redshift intervals. A set of artificially redshifted images was used to quantify and correct for this incompleteness in disk detection, described in the next section.

6.2.1 FERENGI2 set of artificially redshifted galaxy images

FERENGI2 is a set of simulated galaxy images created using the FERENGI code (Barden et al., 2008). These were created from a parent sample of 936 nearby ($z < 0.01$) SDSS galaxies, all of which had been previously classified in Galaxy Zoo 2 and were cross-matched in 2MASS (Skrutskie et al., 2006) for J magnitudes and GALEX (Martin et al., 2005) for NUV magnitudes, which were necessary to create a color-color separation using a method as similar as possible to that of the COSMOS sample. An evolution factor of $e = -1$ was applied, which brightens each galaxy linearly with redshift: $M' = M + ez$, where M' is the corrected magnitude. This correction is performed to mimic the known physical increase of galaxy magnitude with redshift (Lilly et al., 1998; Loveday et al., 2011), and the value $e = -1$ was chosen based on an analysis of spectra template models provided by Brinchmann et al. (2004), which showed that typical galaxies tend to evolve in brightness by one magnitude per redshift. Each galaxy was artificially redshifted 8 times from $z = 0.3$ to $z = 1$ in intervals of $\Delta z = 0.1$ and processed to mimic HST imaging parameters, giving a total of 7,488 images (3 examples are shown in Figure 6.3). The set was then classified in Galaxy Zoo using the same decision tree as used for Galaxy Zoo Hubble. 134 highly inclined disk galaxies were removed from the sample by excluding any with $N_{edgeon} > 20$ and $f_{not\ edge-on} >= 0.6$, using the vote fraction associated with the real galaxy image measured in GZ2. This cut was shown in Galloway et al. (2015) to correlate well with inclination angle $cos(a/b) < 67°$. This was to exclude those which may be mis-classified due to dust-reddening. Using the

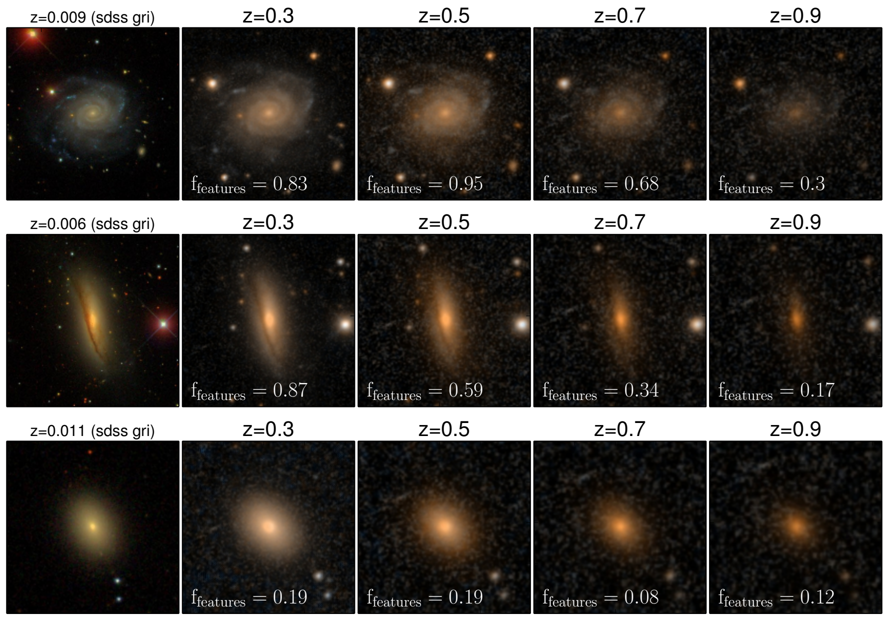

Figure 6.3 Example images of three galaxies artificially redshifted with the FERENGI code. The left image in each row is a real SDSS gri-composite image; the four to the right are images generated by FERENGI at varying redshifts, processed to mimic *HST/COSMOS* imaging. The f_{features} vote fraction for each simulated image is given; this value tends to decrease for each galaxy as it is processed to be viewed at higher redshifts.

NUV-J-R selection method described in section **??**, the remaining sample was divided into a set of red sequence galaxies (259 per redshift bin) and blue cloud (543 per each redshift bin) (see Figure 6.4).

6.2.2 Measuring ξ

The FERENGI2 set was used to measure the incompleteness in disk detection, from which a correction factor ξ was derived. This is defined as the number of disks detected divided by the true number of disks expected to exist in a given redshift interval: $\xi(\mathrm{z}) = \mathrm{N_{detected}}/\mathrm{N_{true}}$. Acknowledging that the completeness in disk detection may depend on

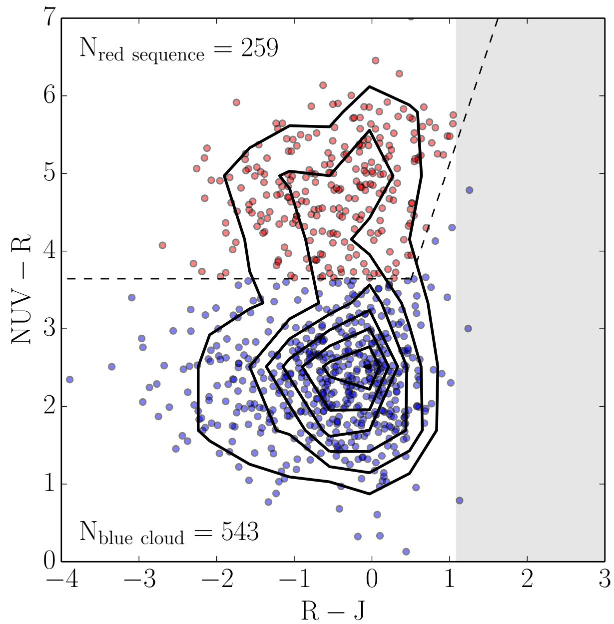

Figure 6.4 Separation of the quiescent population (red sequence) and active population (blue cloud) of the FERENGI2 sample. The gray shaded region represents the R-J limit of the sample; since FERENGI2 is a subset of GZ2, for which a limit of $r < 17$ was implemented, and the magnitude limit of 2MASS is $J < 15.91$, the FERENGI2 sample is limited to R-J < 1.1.

galaxy color, the corrected fraction of passive disks can then be calculated as:

$$f_{R|D} = \frac{N_{RD} \times \xi_{red}^{-1}}{N_{RD} \times \xi_{red}^{-1} + N_{BD} \times \xi_{blue}^{-1}} \tag{6.3}$$

If there is no color bias in disk detection, $\xi_{red} = \xi_{blue}$, and this term cancels out, leaving the fraction unchanged. If there is a bias, however, the ξ terms do not cancel, and the incompleteness in disk detection could have a large effect on the red disk fraction. Therefore a careful measurment of ξ is estimated for both red and blue disk galaxies using the FERENGI2 set of simulated images.

The completness values $\xi_{red}(z), \xi_{blue}(z)$ were then computed in varying bins of redshift for the red sequence and blue cloud galaxies separately. An example calculation of ξ_{blue} in the $z = 0.7$ bin is shown in Figure 6.5. Each point represents a FERENGI2 galaxy, where the y-axis indicates the value of $f_{\rm features}$ measured in the image redshifted to $z = 0.7$, and the x-axis indicates the value of $f_{\rm features}$ measured in the same galaxy redshifted to $z = 0.3$. Disk galaxies are identified as those for which $f_{\rm features} \geq 0.3$. Since, on average, $f_{\rm features}$ decreases for the same galaxy as it is viewed at higher redshifts, the number of galaxies meeting this threshold is generally fewer at higher redshifts than lower redshifts. This is indicated by the dotted lines: galaxies to the right of the vertical dashed line at $\mathrm{f_{features,z=0.3}} = 0.3$ are identified as disks at $z = 0.3$; their sum is considered the "true" number of disks, $\mathrm{N_{true}}$. Similarly, the galaxies above the horizontal line at $\mathrm{f_{features,z=0.7}} = 0.3$ are identified as disks at $z = 0.7$; their sum is the "detected" number of disks at $z = 0.7$, or $\mathrm{N_{detected}}$. As obvious in the figure, $\mathrm{N_{detected}}$ is in general much lower than $\mathrm{N_{true}}$, emphasizing the increasing difficulty in detecting features at higher redshifts. Their ratio is the completeness ξ; in this example $\xi_{blue}(z = 0.7) = 0.61$, meaning only 61% of disks were detected at this redshift.

It was hypothesized that the completeness in disk detection may be a function of other parameters in addition to redshift. At fixed redshift, for example, it is reasonable to guess that features could be easier to detect galaxies that have higher mass, radius, or surface brightness. To test whether these parameters also impact the number of disks detected, the completeness was measured in fixed redshift bins as a function of surface brightness, effective radius, and mass. Surface brightness was measured using SExtractor calculations of `MAG_AUTO`, b/a and R_e measured in the I_{814W} band images, in the same way as described in Chapter 3. The effective radius used was the 50% `FLUX_RADIUS` converted in to kpc, and the masses used were the `MEDIAN` values calculated in the MPA-JHU catalog (Kauffmann et al., 2003b).

Figure 6.6 shows completeness as a function of redshift and surface brightness, for the red sequence and blue cloud galaxies. 8 redshift bins were further divided into bins of surface brightness with varying widths, where the sizes were chosen to satisfy that $\mathrm{N_{detected}} + \mathrm{N_{true}} \geq 10$ in each bin. This was chosen as a comprimise between having a sufficient number of galaxies in each bin to compute the completness fraction $\xi = \mathrm{N_{detected}}/\mathrm{N_{true}}$, and to have enough bins of surface brightness to measure a trend with confidence of completeness as a function of μ. Visual inspection of the data did not suggest any relationship between the two. To be sure, the data were fit to a linear

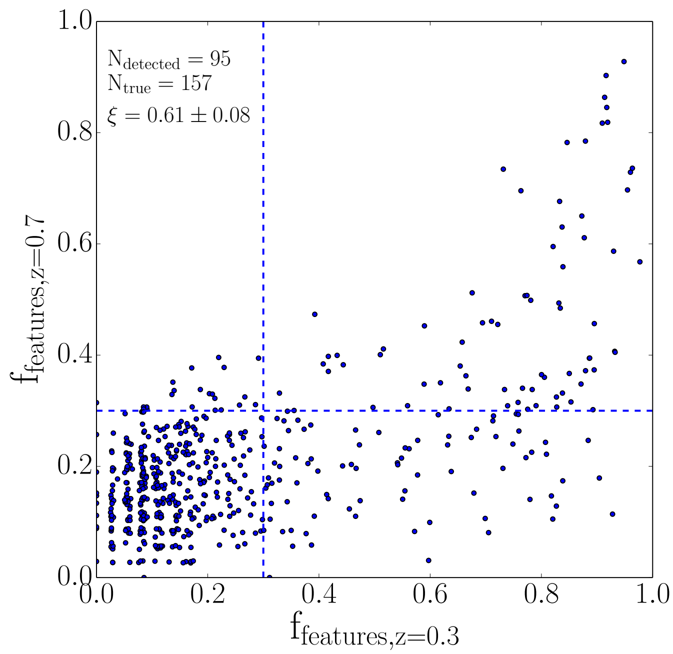

Figure 6.5 Example calculation of completeness ξ at redshift $z = 0.7$. Points represent FERENGI2 images classified in Galaxy Zoo. The y-axis corresponds to the value of f_{features} measured at the galaxy redshifted to $z = 0.7$, and the x-axis corresponds to the value of f_{features} measured at the galaxy redshifted to $z = 0.3$. On average, the f_{features} is lower at the higher redshift, indicating users on average have more difficulty identifying features in images at higher redshifts. The dotted lines correspond to f_{features}=0.3, the threshold above which a galaxy is considered to have a disk. Galaxies to the right of the vertical dashed line were identified as disks at the lowest redshift $z = 0.3$, the total number defined as N_{true}, the true number of disks. Galaxies above the horizontal dash line were identified as disks at the higher redshift $z = 0.7$, the total number defined as N_{detected}. The ratio $\xi = N_{\text{detected}}/N_{\text{true}}$ is the completeness value; in this example, only 61% of disks were detected at $z = 0.7$.

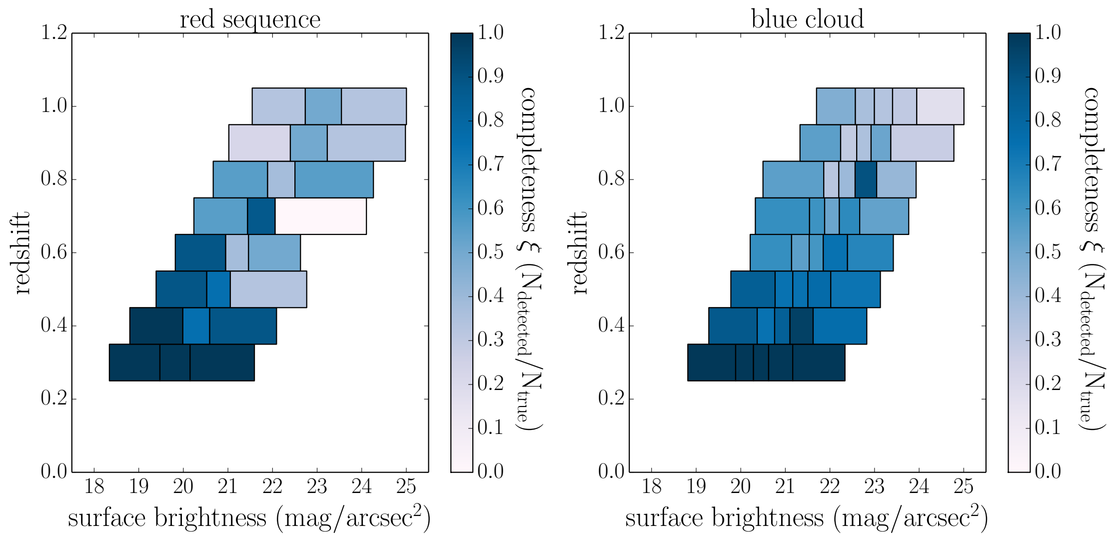

Figure 6.6 Completeness ξ as a function of redshift and surface brightness for red sequence (left) and blue cloud galaxies (right). In each redshift bin, galaxies were binned by surface brightness in varying widths such that $N_{\text{detected}} + N_{\text{true}} \geq 10$ in each bin. The completness ξ was computed in each z, μ bin, represented by the colors. Darker colors represent a completeness of 1, such that all disks were detected, while fainter colors represent a completeness near 0, representing a failure to detect disks. ξ tends to decrease with redshift, but no correlation of ξ with surface brighness is observed at fixed redshift.

function in each redshift bin (Figure 6.7). For each fit, a p-value representing a hypothesis test whose null hypothesis is that the slope is zero was computed. Only one reached the criteria $p < 0.05$, but with a low R^2 value of 0.28 which is not considered large enough to represent a good fit. This process was repeated using effective radius and mass as parameters, with the same results. Therefore only redshift was used as a parameter which impacted completeness value with confidence.

The completeness values ξ_{red} and ξ_{blue} were then measured as a function of redshift for the red sequence and blue cloud FERENGI2 galaxies; results are shown in Figure 6.8. No significant difference was detected for the two functions, which is apparent from the overlapping $1-\sigma$ errors on the plot. Therefore ξ was computed for all galaxies in bins of redshift between 0.3 and 1.0 with widths $\Delta z = 0.1$; from here a linear relationship for ξ as a function of redshift was derived: $\xi(z) = -0.9 \pm x(z) + 1.2 \pm y$. This correction was used to calculate the fraction of disks on the red sequence:

$$f_{D|R} = \frac{N_{RD} \times \xi^{-1}}{N_{RD} + N_{RE}} \quad (6.4)$$

6.3 Results

In this section we present our results of the evolution of disc galaxies from $z = 1$ to $z = 0.2$ in a sample of 27,355 *COSMOS* galaxies morphologically classified in GZH. We will show x, y, and z and talk about it.

6.3.1 The evolving passive disk fractions: $f_{R|D}$ and $f_{D|R}$

The change in the relative number densities of active/passive disk/elliptical galaxies traces the dominant evolutionary pathways they follow at different mass thresholds. In Figure 6.9 we measure these using the fractions defined in the previous section, $f_{R|D}$ (left panel) and $f_{D|R}$ (right panel) for four mass bins. We observe significantly different trends in $f_{R|D}$ for the two highest mass bins ($log(M/M_{\odot}) > 10.7$): for higher-mass galaxies, the fraction of red disks vs. all disks, within error, is either relatively flat or exhibits a small decrease, while the lower-mass galaxies have trends which increase sharply from $z = 1$ to $z = 0.3$. Similarly for the fraction of red disks on the red sequence: the highest mass bin $log(M/M_{\odot}) > 11.0$ decreases in $f_{D|R}$, while the lowest-mass bin increases sharply from $f_{D|R} \sim 0.05$ to ~ 0.2.

To gain a more intuitive understanding of how the trends of these fractions depend on the different possible evolutionary pathways and their transition rates, it is helpful to rewrite them in a reduced form: $f_{R|D} = (1 + \frac{N_{BD}}{N_{RD}})^{-1}$; $f_{D|R} = (1 + \frac{N_{RE}}{N_{RD}})^{-1}$. Using the former as an example: at zeroth order, it can be seen that if the number of red disks increases at a higher rate than an increase in blue disks in some time interval, the overall fraction $f_{R|D}$ would also increase. For a single mass bin, this scenario would be consistent with a model in which blue galaxies are quenching faster than they are entering the mass bin via star formation. A strong decrease in $f_{R|D}$ would, in constrast, indicate a higher rate of red disks exiting the mass bin than the blue disks; the strength of the decrease would depend on the relative frequencies of blue galaxies quenching to form new red disks and red disks merging to form red ellipticals. The precise relative

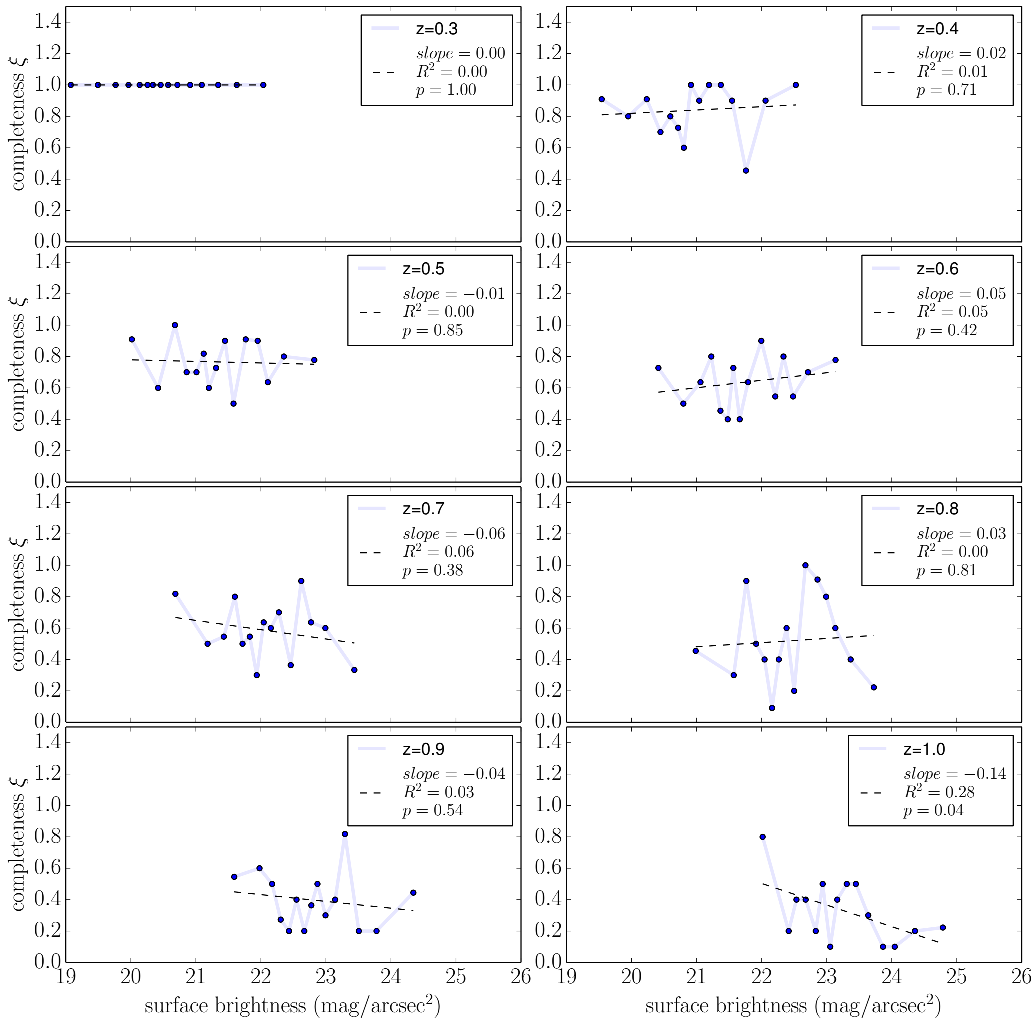

Figure 6.7 No observed dependence on completeness ξ with surface brightness at fixed redshift. Shown is ξ vs μ in bins of redshift for blue cloud galaxies (average values of ξ in each redshift bin are shown in Figure 6.6, right panel). Linear fits were computed in each bin, shown as the dashed black lines. Low overall R^2 values and large p values, displayed in the legends of each panel, suggest surface brightness does not have a strong effect on completeness. The final calculation for ξ was therefore only a function of redshift.

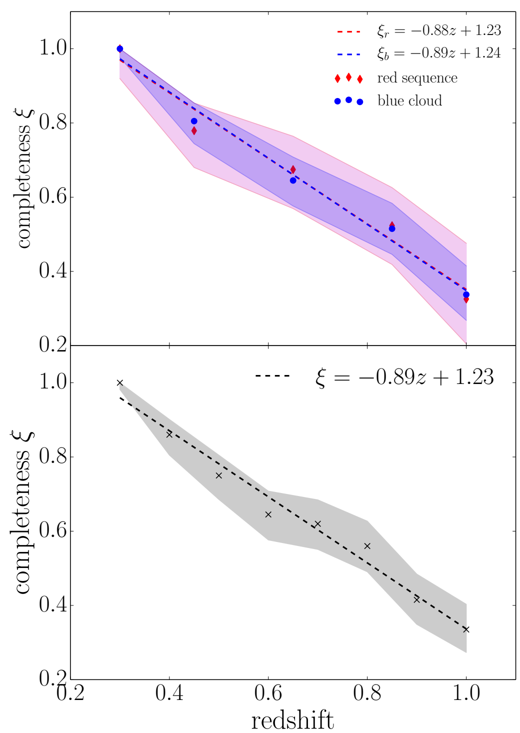

Figure 6.8 **Top:** Completeness ξ as a function of redshift for red sequence and blue cloud FERENGI2 galaxies separately. Both populations show a strong dependence on ξ with redshift, but are indistinguishable from each other. **Bottom:** Completeness as a function of redshift for all FERENGI2 galaxies (red and blue combined). The equation representing the linear fit is displayed.

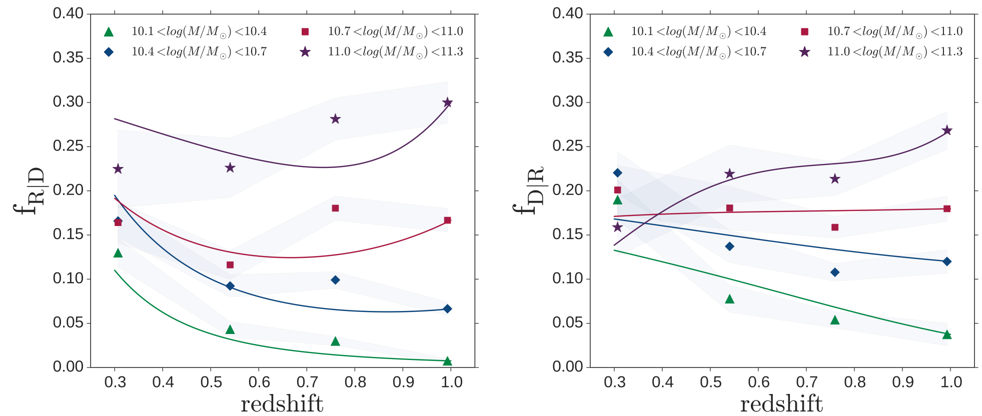

Figure 6.9 **Left:** Passive disk fraction ($N_{\text{red disks}}/(N_{\text{red disks}} + N_{\text{blue disks}})$) vs redshift in four mass bins. **Right:** Fraction of disks on the red sequence ($N_{\text{red disks}}/(N_{\text{red disks}} + N_{\text{red ellipticals}})$) vs redshift in four mass bins. The solid lines represent the evolution of the fractions computed by the toy-model described in Section 6.3 using rate parameters which yielded the lowest χ^2.

values of these rates cannot be deduced by a simple by-eye analysis of the fraction, however.

We therefore implement a simple toy model to track the change in $f_{R|D}$ and $f_{D|R}$, given a range of parameters representing the quenching and morphological transformation rates for galaxies at fixed stellar mass. We begin by considering the rate of change in the number of blue disks (dN_{BD}/dt), red disks (dN_{RD}/dt), and red ellipticals (dN_{RE}/dt). In a given mass bin, the change in numbers for each population will depend on several parameters, illustrated visually in Figure 6.10.

Blue Disks

First, galaxies in a blue bin may transition into a red disk bin via a quenching process that does not destroy its disk; we define this rate as $r_{BD\rightarrow RD}$, representing the fraction of blue galaxies to transition to red disks per Gyr (path A in Figure 6.10). Blue galaxies may also exit a bin via a quenching process which *does* destroy the disk; this fraction per Gyr we define as $r_{BD\rightarrow RE}$ (path C in Figure 6.10).

The number of galaxies in a blue disk bin will also change due to star formation, which brings active galaxies from a lower mass bin into the current mass bin. To

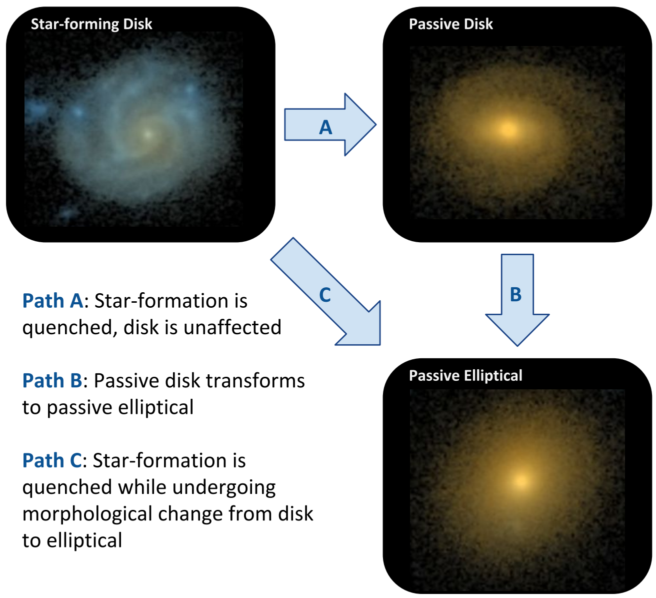

Figure 6.10 Cartoon representing three evolutionary pathways represented in the toy-model described in Section 6.3. Path A represents an active star-forming galaxy which quenches without destroying the disk, becoming a red disk; the fraction of blue galaxies to follow this track is represented by $r_{BD \to RD}$ in the model. Path B represents a red disk morphologically transition to red ellipitcal; the fraction of red galaxies to follow this track is $r_{RD \to RE}$. Path C represents a blue disks simultaniously quenching and morphologically transforming to become a red elliptical; the fraction of blue galaxies to follow this track is $r_{BD \to RE}$. (The fourth driver of the relative numbers of different morphological types is κ_{RE}, the net merger rate of ellipticals in a given mass bin, and is not represented in the cartoon.)

account for this term we use the formalism outlined by Peng et al. (2010), in which this rate of change is given by $(\alpha + \beta)sSFR$. Here $\alpha = d\phi_{blue}/dm$ is the derivative of the mass function for blue galaxies, which equates to $\alpha = (1 + \alpha_s) - m/M^*$ for a mass function described by the Schechter (1976) function. We use best-fit parameters for blue galaxies measured by (Ichikawa & Matsuoka, 2017), which give $\alpha_s = -1.4$ and $M^* = 10.28$ $(log(M/M_\odot))$. Following the method of Peng et al. (2010), we let $\beta = 0$, both for simplicity, and because their conclusions found not to be strongly dependent on β. Last, the specific star-formation rate is given by $sSFR(t) = 2.5(\frac{t}{3.5Gyr})^{-2.2}Gyr^{-1}$ (Peng et al., 2010).

Accounting for all sources and sinks of blue disks entering or exiting a bin of given mass, the rate of change of blue disks can be written fully as:

$$\left.\frac{dN_{BD}}{dt}\right|_m = \Big(- r_{BD\to RD} - r_{BD\to RE} - \alpha(m)sSFR(t)\Big)N_{BD} \tag{6.5}$$

Red Disks

Galaxies exiting a blue bin as they quenched without disrupting their disks enter the pool of red disks, increasing N_{RD} for a given mass bin. Red disks also may undergo a morphological transformation, depleting the pool of red disks as they enter the red elliptical bin (path B in Figure 6.10). The fraction of galaxies to undergo this pathway per Gyr is denoted as $r_{RD->RE}$. Combining these factors gives the expression:

$$\left.\frac{dN_{RD}}{dt}\right|_m = +r_{BD\to RD}N_{BD} - r_{RD\to RE}N_{RD} \tag{6.6}$$

Red Ellipticals

In this simple model, it is assumed that red, passive ellipticals are the final state in a typical galaxy's evolution. Therefore N_{RE} will always be increasing from the transformation from blue disks and red disks to red ellipticals ($r_{BD\to RE}$, $r_{RD\to RE}$). However, the number of red ellipticals *in a single mass bin* may still decrease due to ellipticals at the given mass merging to enter a bin of red ellipticals at a higher mass. Similarly, their number can increase as ellipticals from a lower mass bin merge to enter the current mass bin. A complete, semi-analytic model would consider this full range of possibilities and couple the resulting equations appropriately amongst all mass bins. For the purposes of this simple model, we opted to represent the total, net rate of change of the number of red ellipticals as a single parameter, κ_{RE}, which we note may be positive or negative, depending on whether more ellipticals are entering or leaving the given mass bin.

$$\frac{dN_{RE}}{dt}\Big|_m = \kappa_{RE} N_{RE} \tag{6.7}$$

We exclude the contribution from blue ellipticals from the model because they represent only a small fraction of the total population (find references which quantify this.) We initialize our model using the observed relative numbers of blue disks, red disks, and red ellipticals measured at $z = 1$, then use the model to compute their evolution to $z = 0.3$ using a range of values for each of the four parameters in four mass bins. For $r_{BD\to RD}, r_{BD\to RE}$, and $r_{RD\to RE}$, we test 25 values between 0 and 1, and 25 values between -1 and 1 for κ_{RE}. We note that a complete model would explore time-varying rates, but for the purposes of simplicity in our toy-model we only experiment with static parameters. For each mass bin, the model was implemented for each permutation of the four rate parameters. The success of each run was evaluated using a χ^2 metric; these results are shown for each mass bin in the corner-plot in Figure 6.11. The bins are weighted by $1/\chi^2$, such that white regions represent the rate parameters that yield the lowest χ^2, and black representing the largest.

We find a strong mass dependence on the fraction of blue galaxies to quench to red disks ($r_{BD\to RD}$), or Path A in Figure 6.10. Our observations of $f_{R|D}$ and $f_{D|R}$ are most closely reproduced when $r_{BD\to RD}$ = [0.05, 0.07, 0.1, 0.2] Gyr^{-1} for masses log(M/M$_\odot$) = [10.25,10.55,10.85,11.0]. [Note: need to measure peaks explicitely, current values are by-eye. Also calculate 1-sig errors.] These values for $r_{BD\to RD}$ correspond to the peaks of the 1-D histograms shown in Figure 6.11. This increase of $r_{BD\to RD}$ with mass could suggest either: 1) more massive galaxies are more likely to undergo quenching processes which do not destroy their disks, or 2) less massive galaxies simply quench less frequently overall, via any pathway.

Analysis of the next parameter in the low mass bin, $r_{BD\to RE}$, suggests that the former is more likely, given the peak of $r_{BD\to RE}$ at > 0.9 Gyr^{-1}. The high rate of low-mass blue disks quenching to red ellipticals is evidence that they do not quench any less frequently than high mass galaxies, and the increase of $r_{BD\to RD}$ with mass is indeed consistent with quenching processes less likely to destroy the disk of massive

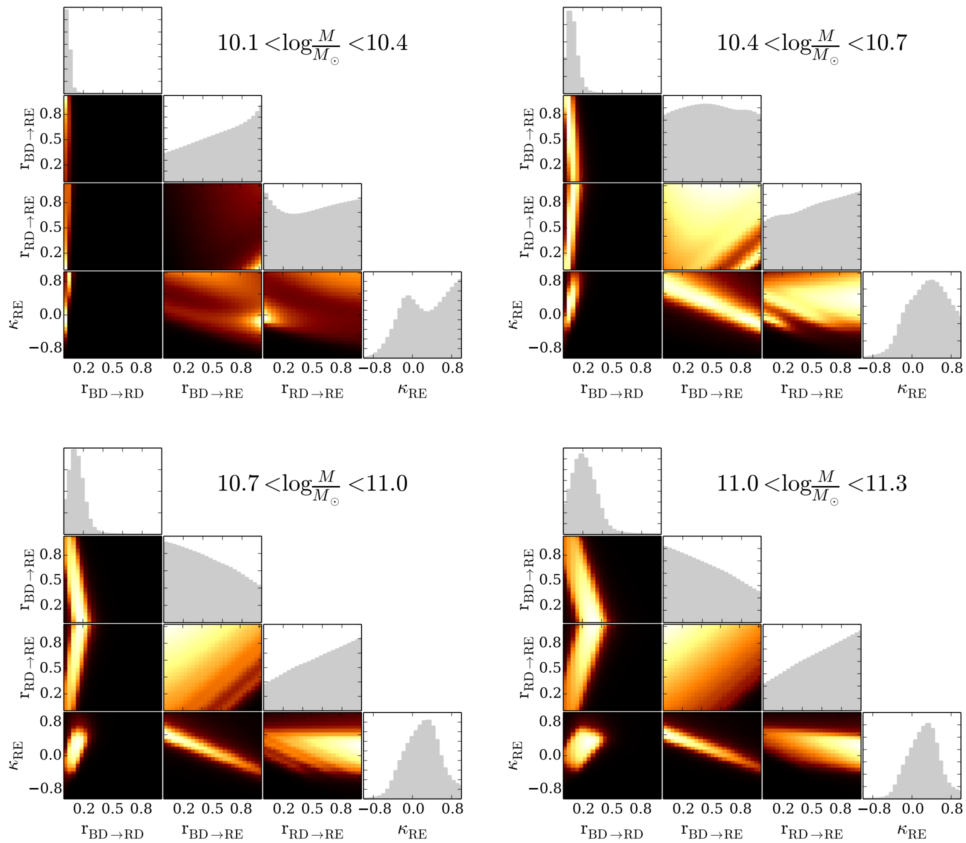

Figure 6.11 Results of the grid-search for the best-fit rate parameters $r_{BD\to RD}, r_{BD\to RE}, r_{RD\to RE}$, and κ_{RE} for four mass bins. The units for all rate parameters is Gyr^{-1}. 25 equally-spaced values were tested between (0,1) for each parameter, with the exception of κ_{RE} which was tested for 25 values between (-1,1); these are represented by the 25 bins on each axis. Each bin is weighted by $1/\chi^2$, such that white regions correspond to parameters which produced the lowest χ^2, and black representing the highest. There is a strong result in the dependence of $r_{BD\to RD}$ with mass, such that the fraction of blue disks which transition to red disks (ie, quench without disrupting the disk), increases for more massive galaxies. The other parameters are less constrained by this model; therefore a more complex semi-analytic model will be necessary for obtaining the precise values of these rates, and is the subject of future work.

galaxies. However, this result is not nearly as constrained, given the broad distribution of likelihoods for this parameter. $r_{BD \to RE}$ is even less constrained for all higher masses. The degeneracies evident in this rate and $r_{RD \to RE}$ make it clear that our model is not sufficient to constrain the relative fequencies of the processes involved in quenching and morphological transformations; a more sophisticated model with the adjustments we have described thus far would be necessary to paint the full picture.

6.4 Discussion

We have explored the evolution of the passive disk population since $z = 1$ by quantifying their abundances in terms of the fraction of disk galaxies that are red $f_{R|D}$ and the fraction of the red sequence occupied by disks $f_{D|R}$. For both fractions, we observed dependencies on both mass and redshift; this is a strong indication that passive disks play an important role in understanding the processes involved in the quenching and morphological transformation of galaxies. We identified three pathways to describe the evolution of a star-forming disk: $r_{BD \to RD}$ (the rate of blue disks quenching to red disks), $r_{BD \to RE}$ (the rate of blue disks quenching and transforming directly to red ellipticals), and $r_{RD \to RE}$ (the rate of red disks transforming to red ellipticals), and we argue that the relative frequencies of these rates drive the trends in $f_{R|D}$ and $f_{D|R}$. To begin quantifying the occurances of each of the pathways, we developed a toy model to reproduce $f_{R|D}$ and $f_{D|R}$ given some set of rates. Our model was able to constrain $r_{BD \to RD}$ to a reasonable degree of certainty, but the rest would require a more sophisticated model to deduce.

An analysis of $r_{BD \to RD}$ provides an estimate for the fraction of galaxies to go through a passive disk phase. For the most massive galaxies, we find $r_{BD \to RD} = 0.20 \pm .1\ Gyr^{-1}$, indicating that 20% of massive galaxies become red disks at some point in their lifetime. Whether these 20% tend to stay red disks or tend to evolve to ellipticals is unclear without a more solid constraint on $r_{RD \to RE}$. Using the same logic for the other three mass bins, we can find that [5%, 7%, 10%] of galaxies with masses [10.25,10.55,10.85] become red disks in their lifetimes. These estimates are in agreement with Bundy et al. (2010) (hereafter B10) who estimate an upper limit of 60% of massive galaxies to experience a red disk phase. Their estimation comes from a different approach to ours, via an analysis of the mass function of galaxies with different morphologies and the fractional contribution of disks on the red sequence $f_{D|R}$.

Our estimation of the significance of the passive disk population is in agreement with B10 for the most massive galaxies, as is the downward trend in $f_{D|R}$ with redshift from $z = 1$ to $z = 0.3$. As suggested previously, a downward trend of $f_{D|R}$ represents either a depletion of the total pool of red disks (via a transformation to elliptical), but could also be an indication of an increase in the pool of red ellipticals (which could result from blue or red disks transforming morphology). In contrast, an upward trend is only possible via a pile-up of red disks, which is what we observe for the lower mass bins. Thus far our results are then consistent with a physical scenerio in which 1) more massive galaxies are more likely to become passive disks (given by the increase of $r_{BD\to RD}$ with increasing mass), and 2) less massive galaxies who enter a red disk phase are more likely than massive galaxies to stay in that phase, rather than transform to elliptical (given by the increase of $f_{D|R}$ from $z = 1$ to $z = 0.3$ for low mass bins).

Our first point is in agreement with literature which explores the unimodality of disk galaxies across a CMD (Schawinski et al., 2014; Powell et al., 2017). The smooth transition from the blue cloud to the red sequence in the distribution of low to medium mass disk galaxies is evidence for slow quenching timescales. For higher mass disk galaxies, the unimodality is broken, suggesting a more rapid quenching. This could be due to a higher merger rate for more massive galaxies, or as suggested by Schawinski et al. (2014), evidence for a mass-quenching effect, in which the galaxy's halo reaches a critical mass whereby the gas is inhibited from cooling sufficiently to continue star-formation (Kormendy & Kennicutt, 2004; Dekel & Birnboim, 2006; Peng et al., 2010). This result is also consistent with B10, who observe the strongest decrease in $f_{D|R}$ from $z = 1$ to $z = 0.3$ for their most massive galaxies.

Our second point is in disagreement with B10, who observe downward trends in $f_{D|R}$ in low mass galaxies. At the lowest redshift bin ($z \sim 0.3$), we measure similar absolute fractions of disks occupying the red sequence for all masses. However, B10 find their contribution to increase at higher lookback time to $z = 1$, while we find a decreasing contribution. The fact that our results agree for the highest mass at all redshifts, but only at the lowest redshift for lower masses, suggests the differences may be attributed in biases in morphological classification. B10 indentifies early and late-type disk galaxies using ZEST (Scarlata et al., 2007) morphologies, which they acknowledge are biased towards disk classification for faint apparent magnitudes, which tend to be attributed to the lowest mass, highest redshift objects. This bias could influence their observed increase in red sequence disks toward $z = 1$ for low masses. On the opposite end, GZ classifications tend to be biased towards elliptical morphologies at fainter magnitudes. We attempted to quantify and correct for this effect as described in Section 6.2.1, but if our correction was under-estimated, that may have driven the decreasing abundance of disk galaxies observed at increasing redshift for low masses. However, it has been shown in the local Universe that red disk galaxies tend to be more massive, as in Masters et al. (2011). If this is true at all epochs, we would not expect such a significant contribution of red disks for low mass galaxies as found in B10.

6.5 Conclusions

We have investigeted the influence of the passive disk population by measuring the relative abundances of blue disks, red disks, and red ellipticals since $z = 1$ using morphological classifications from Galaxy Zoo: Hubble and rest-frame colors from UltraVISTA. Using data from artificially-redshifted FERENGI2 images to quantify the known redshift bias in the GZ classifications, we implemented a correction to the incompleteness in the number of disks detected as a function of redshift. The relative numbers were measured in terms of the fraction of disk galaxies that are red $f_{R|D}$ and the fraction of disk galaxies on the red sequence $f_{D|R}$. A simple toy-model was developed to simulate the evolution of these fractions as a function of the rates of three dominant evolutionary pathways: $r_{BD \to RD}$, the rate of blue disks quenching to red disks, $r_{BD \to RE}$,the rate of blue disks quenching and transforming directly to red ellipticals, and $r_{RD \to RE}$,the rate of red disks transforming to red ellipticals. Our main conclusions are as follows:

- $f_{R|D}$ and $f_{D|R}$ decrease from $z = 1$ to $z = 0.3$ for massive galaxies, and increase for the least massive galaxies.
- We estimate as high as 20% (+-error) of massive ($log(M/M_{\odot}) > 11$) galaxies experience a passive disk phase. This fraction decreases with mass, down to 5+-% for galaxies $log(M/M_{\odot}) < 10.4$.

- Low mass galaxies which experience a passive disk phase are more likely than massive galaxies to remain disks, while massive galaxies are more likely to continue thier evolution by transforming to passive ellipticals. To quantify and validate this result would require a more sophisticated model than the simple approached used in this project.

Chapter 7

Looking Forward

Morphology has been, and continues to be, one of the strongest tools available for unravelling the fundamental aspects of the evolution of galaxies. Understanding the myriad secular and environmental processes which give rise to the multitude of morphological types observed contributes to our growing knowledge of the past, present, and future of our Universe.

Using morphology as such a tool, however, is not without its own challenges. Most of these stem from the difficulty in obtaining accurate morphological classifications on a sufficiently large scale. For example, while the SDSS has imaged the largest number of galaxies in a single survey to date ($N \sim 900,000$), only a small fraction of these are nearby enough, large enough, and bright enough to accurately classify their morphologies. Figure 7.1 shows side-by-side images of a galaxy at $z = 0.1$ imaged by SDSS (left) and HST (right). The ground-based image at 0.4"/pixel is not resolved enough to even make out the strong bar or spiral arms, which are very easy to identify in the HST image at 0.04"/pixel.

The solution to this problem has typically been to limit one's sample to only include the most bright galaxies, via a magnitude or volume-limit, to ensure all morphologies in the study are accurate. However a statistical price is paid, particularly in population studies which seek to identify dominant trends in large samples of galaxies. Such studies tend to require extensive binning of the parent sample to remove inter-dependencies in the variables, which as a consequence increases the statistical error in the results as the number of subjects per bin decreases. This type of limitation amplifies as one extends

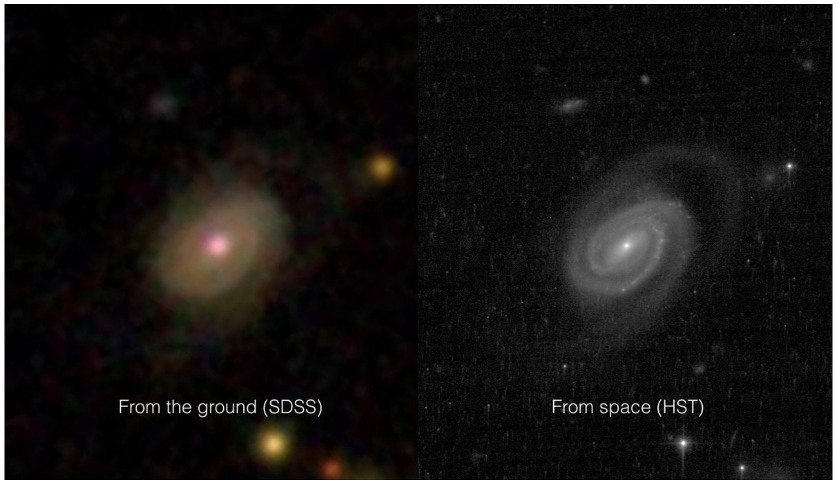

Figure 7.1 Resolution of the instrument has a strong impact on the physical appearance of a galaxy, and large differences could change a morphological classification drastically, even for nearby galaxies. Shown is a spiral galaxy at $z = 0.1$, imaged by SDSS at $\sim$.4"/pixel (left), and HST at $\sim$.04"/pixel (right) (HST Program ID 14606, PI: Simmons). The strong bar and distinct spiral arms in the HST imaging are mostly lost in the low-resolution ground-based image.

to higher redshift; even the high-resolution capability of HST is insufficient in capturing consistent detailed morphological substructures for galaxies beyond $z \sim 0.5$, except for the very largest and brightest objects.

The future of the field is incredibly promising, as technological advances in instrumentation continue to improve on these limitations. Noteworthy examples include the Giant Magellan Telescope (GMT), Extremely Large Telescope (ELT), and the Thirty Meter Telescope (TMT) which will provide images 10-16 times sharper than HST, due to their improved light-collecting areas via large mirrors and implementation of sophisticated adaptive optics technology.

Perhaps the most notable upcoming advances in this field involve the Large Synoptic Space Telescope (LSST) and the Euclid mission, which will be imaging galaxies on scales previously unattainable. Producing data on the order of terabytes per night, the surveys are ultimately expected to produce detailed images of more than a billion galaxies. While samples on this scale may certainly solve the afforementioned statistical challenges of morphological population studies, this inflow of data presents an entirely new challenge: how can we possibly obtain accurate morphologies on such a large scale in a reasonable timeframe? On these scales, even crowdsourced visual inspection via Galaxy Zoo is nowhere near fast enough.

The next stage of Galaxy Zoo is tackling this issue by combining human and machine effort, beginning with an innovative system dubbed Galaxy Zoo Express (GZX) (Beck et al. 2017, submitted). GZX improves on the speed and accuracy of human classifications in two ways. First, it maximizes the information that can be obtained from human effort via the algorithm SWAP (Space Warps Analysis Pipeline) (Marshall et al., 2016). SWAP continuously tracks and updates the probability that a galaxy has a given feature, given the history of the volunteers' classifications and their performance classifying known galaxies as part of a training set. Using this technique, human effort is greatly reduced as most galaxies would not require 40 volunteers all classifying each galaxy, which was the retirement threshold in all previous GZ projects. Second, GZX incorporates a machine-learning algorithm which works together with the human classifications to increase the classification time even further. With all of these improvements combined, Beck et al. 2017 showed that GZX could classify 70% of the GZ2 catalog in *32 days*, a feat that took a full year using the current approach.

This thesis began with the observation that all data available for studying the evolution of the Universe is contained in a single snapshot of the present cosmos. Methods of imaging galaxies in this snapshot are continuously advancing, as are methods for fast and efficient morphological classification. These advancements undoubtedly point to a promising new era of discovery, which should unveil a whole new wealth of information to further our understanding of the life and fate of galaxies in the Universe.

So long and thanks for all the fish!

References

Abazajian, K. N., Adelman-McCarthy, J. K., Agüeros, M. A., et al. 2009, The Astrophysical Journal Supplement Series, 182, 543

AdelmanMcCarthy, J. K., Agüeros, M. A., Allam, S. S., et al. 2008, The Astrophysical Journal Supplement Series, 175, 297

Aird, J., Coil, A. L., Moustakas, J., et al. 2012, The Astrophysical Journal, 746, 90

Alonso, S., Coldwell, G., & Lambas, D. G. 2013, 10

Anderson, D. P. 2002, Commun. ACM, 45, 56

Ann, H. B., & Thakur, P. 2005, The Astrophysical Journal, 620, 197

Antonini, F., Barausse, E., & Silk, J. 2015, arXiv:1506.02050

Arnouts, S., Walcher, C. J., Le Fèvre, O., et al. 2007, Astronomy and Astrophysics, 476, 137

Athanassoula, E. 1992, Monthly Notices of the Royal Astronomical Society, 259, 328

—. 2003, Monthly Notices of the Royal Astronomical Society, 341, 1179

Athanassoula, E., Lambert, J. C., & Dehnen, W. 2005, Monthly Notices of the Royal Astronomical Society, 363, 496

Athanassoula, E., Machado, R. E. G., & Rodionov, S. A. 2013, Monthly Notices of the Royal Astronomical Society, 429, 1949

Baillard, A., Bertin, E., de Lapparent, V., et al. 2011, Astronomy & Astrophysics, 532, A74

Baldry, I. K., Glazebrook, K., Brinkmann, J., et al. 2004, The Astrophysical Journal, 600, 681

Baldwin, J. A., Phillips, M. M., & Terlevich, R. 1981, Publications of the Astronomical Society of the Pacific, 93, 5

Bamford, S. P., Nichol, R. C., Baldry, I. K., et al. 2009, Monthly Notices of the Royal Astronomical Society, 393, 1324

Barden, M., Jahnke, K., & Häußler, B. 2008, The Astrophysical Journal Supplement Series, 175, 105

Barnes, J. E., & Hernquist, L. 1996, The Astrophysical Journal, 471, 115

Bekki, K., Couch, W. J., & Shioya, Y. 2002, The Astrophysical Journal, 577, 651

Bell, E. F., Wolf, C., Meisenheimer, K., et al. 2004, The Astrophysical Journal, 608, 752

Benson, A., Bower, R., Frenk, C., et al. 2003, The Astrophysical Journal, 599, 38

Bernardi, M., Sheth, R. K., Annis, J., et al. 2003, The Astronomical Journal, 125, 1882

Block, D. L., Buta, R., Knapen, J. H., et al. 2004, The Astronomical Journal, 128, 183

Block, D. L., & Puerari, I. 1999, Astronomy & Astrophysics, 342, 627

Block et al., D. 1994, Astronomy & Astrophysics, 288, 365

Bournaud, F., Combes, F., & Semelin, B. 2005, Monthly Notices of the Royal Astronomical Society: Letters, 364, L18

Bower, R. G., Benson, A. J., Malbon, R., et al. 2006, Monthly Notices of the Royal Astronomical Society, 370, 645

Brinchmann, J., Charlot, S., White, S. D. M., et al. 2004, Monthly Notices of the Royal Astronomical Society, 351, 1151

Brown, J. S., Valluri, M., Shen, J., & Debattista, V. P. 2013, The Astrophysical Journal, 778, 151

Bruzual & Charlot. 2003, Monthly Notices of the Royal Astronomical Society, 344, 1000

Bundy, K., Scarlata, C., Carollo, C. M., et al. 2010, The Astrophysical Journal, 719, 1969

Buta, R. J. 2013, 106

Buta, R. J., Sheth, K., Regan, M., et al. 2010, The Astrophysical Journal Supplement Series, 190, 147

Cameron, E. 2013, Publications of the Astronomical Society of Australia, 28, 128

Cardamone, C., Schawinski, K., Sarzi, M., et al. 2009, Monthly Notices of the Royal Astronomical Society, 399, 1191

Cassata, P., Cimatti, A., Kurk, J., et al. 2008, Astronomy and Astrophysics, 483, L39

Cheung, E., Athanassoula, E., Masters, K. L., et al. 2013, The Astrophysical Journal, 779, 162

Cheung, E., Trump, J. R., Athanassoula, E., et al. 2015, 13

Cirasuolo, M., McLure, R. J., Dunlop, J. S., et al. 2007, Monthly Notices of the Royal Astronomical Society, 380, 585

Cisternas, M., Gadotti, D. A., Knapen, J. H., et al. 2013, The Astrophysical Journal, 776, 50

Combes, F. 2007, Proceedings of the International Astronomical Union, 3, doi:10.1017/S1743921308017535

Conselice, C. J. 2003, The Astrophysical Journal Supplement Series, 147, 1

—. 2006, Monthly Notices of the Royal Astronomical Society, 373, 1389

—. 2012, arXiv:1212.5641

Consolandi, G., Dotti, M., Boselli, A., Gavazzi, G., & Gargiulo, F. 2017, arXiv:1701.00364

Cooray, A. 2005, Monthly Notices of the Royal Astronomical Society, 363, 337

Correa, C. A., Schaye, J., Clauwens, B., et al. 2017, arXiv:1704.06283

Croton, D. J., Springel, V., White, S. D. M., et al. 2006, Monthly Notices of the Royal Astronomical Society, 365, 11

Csabai, I., Budavári, T., Connolly, A. J., et al. 2003, The Astronomical Journal, 125, 580

D. Block, R. W. 1991, Nature, 353, 48

De Lucia, G., Springel, V., White, S. D. M., Croton, D., & Kauffmann, G. 2006, Monthly Notices of the Royal Astronomical Society, 366, 499

de Souza, R. E., Capelato, H. V., Arakaki, L., & Logullo, C. 1982, The Astrophysical Journal, 263, 557

de Vaucouleurs, G. 1963, The Astrophysical Journal Supplement Series, 8, 31

—. 1991, Third Reference Catalogue of Bright Galaxies. (New York: Springer)

Debattista, V. P., Carollo, C. M., Mayer, L., & Moore, B. 2004, The Astrophysical Journal, 604, L93

Debattista, V. P., Mayer, L., Carollo, C. M., et al. 2006, The Astrophysical Journal, 645, 209

Dekel, A., & Birnboim, Y. 2006, Monthly Notices of the Royal Astronomical Society, 368, 2

Deng, X.-F., He, J.-Z., Wu, P., & Ding, Y.-P. 2009, The Astrophysical Journal, 699, 948

Devour, B., & Bell, E. 2017, 5

Di Matteo, T., Springel, V., & Hernquist, L. 2005, Nature, 433, 604

Dieleman, S., Willett, K. W., & Dambre, J. 2015, Monthly Notices of the Royal Astronomical Society, 450, 1441

Dressler, A. 1980, The Astrophysical Journal, 236, 351

Dressler, A., Smail, I., Poggianti, B. M., et al. 1999, The Astrophysical Journal Supplement Series, 122, 51

Ellison, S. L., Nair, P., Patton, D. R., et al. 2011, Monthly Notices of the Royal Astronomical Society, 416, 2182

Eskridge, P. B., Frogel, J. A., Pogge, R. W., et al. 2000, The Astronomical Journal, 119, 536

—. 2002, The Astrophysical Journal Supplement Series, 143, 73

Fillingham, S. P., Cooper, M. C., Pace, A. B., et al. 2016, arXiv:1606.07810

Fortson, L., Masters, K., Nichol, R., et al. 2012, Advances in Machine Learning and Data Mining for Astronomy, 213

Franzetti, P., Scodeggio, M., Garilli, B., et al. 2007, Astronomy and Astrophysics, 465, 711

Friedli, D., & Benz, W. 1993, Astronomy and Astrophysics, 268

Fukugita, M., Nakamura, O., Okamura, S., et al. 2007, The Astronomical Journal, 134, 579

Galloway, M. A., Willett, K. W., Fortson, L. F., et al. 2015, Monthly Notices of the Royal Astronomical Society, 448, 3442

Ghez, A. M., Salim, S., Weinberg, N. N., et al. 2008, The Astrophysical Journal, 689, 1044

Giallongo, E., Salimbeni, S., Menci, N., et al. 2005, The Astrophysical Journal, 622, 116

Goto, T., Okamura, S., Sekiguchi, M., et al. 2003, Publications of the Astronomical Society of Japan, 55, 757

Graham, A. W., Driver, S. P., Petrosian, V., et al. 2005, arXiv:0504287

Graham, A. W., Onken, C. A., Athanassoula, E., & Combes, F. 2011, Monthly Notices of the Royal Astronomical Society, 412, 2211

Gültekin, K., Richstone, D. O., Gebhardt, K., et al. 2009, The Astrophysical Journal, 698, 198

Gunn, J., & Gott, J. 1972, apj, 176, 1

Hackwell, J., & Schweizer, F. 1983, The Astrophysical Journal, 265, 643

Hammer, F., Flores, H., Puech, M., et al. 2009, arXiv:0903.3962

Hao, L., Jogee, S., Barazza, F. D., Marinova, I., & Shen, J. 2009, Galaxy Evolution: Emerging Insights and Future Challenges, 419

Hart, R. E., Bamford, S. P., Casteels, K. R. V., et al. 2017, arXiv:1703.02053

Hart, R. E., Bamford, S. P., Willett, K. W., et al. 2016, Monthly Notices of the Royal Astronomical Society, 461, 3663

Hawarden, T. G., Mountain, C. M., Leggett, S. K., & Puxley, P. J. 1986, Monthly Notices of the Royal Astronomical Society, 221, 41P

Heckman, T., & Best, P. 2014, arXiv:1403.4620

Hickox, R. C., Mullaney, J. R., Alexander, D. M., et al. 2014, The Astrophysical Journal, 782, 9

Ho, L. C., Filippenko, A. V., & Sargent, W. L. W. 1997, arXiv:9704100

Hopkins, P. F., Hernquist, L., Cox, T. J., et al. 2006, The Astrophysical Journal Supplement Series, 163, 1

Hopkins, P. F., & Quataert, E. 2010, Monthly Notices of the Royal Astronomical Society, 407, 1529

Hou, A., Parker, L. C., Harris, W. E., & Wilman, D. J. 2009, The Astrophysical Journal, 702, 1199

Hring, N., & Rix, H.-W. 2004, The Astrophysical Journal, 604, L89

Hubble, E. 1926, The Astrophysical Journal, 64, 321

Huertas-Company, M., Gravet, R., Cabrera-Vives, G., et al. 2015, The Astrophysical Journal Supplement Series, 221, 8

Hughes, T. M., & Cortese, L. 2009, Monthly Notices of the Royal Astronomical Society: Letters, 396, L41

Hunt, L. K., & Malkan, M. A. 1999, The Astrophysical Journal, 516, 660

Ichikawa, A., & Matsuoka, Y. 2017, arXiv:arXiv:1706.03438v1

Ilbert, O., McCracken, H. J., Le Fèvre, O., et al. 2013, Astronomy & Astrophysics, 556, A55

Kauffmann, G., Heckman, T. M., Simon White, D. M., et al. 2003a, Monthly Notices of the Royal Astronomical Society, 341, 33

Kauffmann, G., Heckman, T. M., White, S. D. M., et al. 2003b, Monthly Notices of the Royal Astronomical Society, 341, 54

Kauffmann, G., Heckman, T. M., Tremonti, C., et al. 2003c, arXiv:0304239

Kawata, D., & Mulchaey, J. S. 2007, arXiv:0707.3814

Kewley, L. J., Dopita, M. A., Sutherland, R. S., Heisler, C. A., & Trevena, J. 2001, The Astrophysical Journal, 556, 121

Kewley, L. J., Groves, B., Kauffmann, G., & Heckman, T. 2006, Monthly Notices of the Royal Astronomical Society, 372, 961

Knapen, J. H., Shlosman, I., & Peletier, R. F. 2000, The Astrophysical Journal, 529, 93

Kormendy, J., & Gebhardt, K. 2001, in AIP Conference Proceedings, Vol. 586 (AIP), 363–381

Kormendy, J., & Kennicutt, R. C. 2004, Annual Review of Astronomy and Astrophysics, 42, 603

Kormendy, J., & Richstone, D. 1995, Annual Review of Astronomy and Astrophysics, 33, 581

Kraljic, K., Bournaud, F., & Martig, M. 2012, The Astrophysical Journal, 757, 60

Kruk, S. J., Lintott, C. J., Simmons, B. D., et al. 2017, arXiv:1705.00007

Laine, S., Shlosman, I., Knapen, J. H., & Peletier, R. F. 2002, The Astrophysical Journal, 567, 97

Larson, R.B., Tinsley, B.M. and Caldwell, C. 1980, The Astrophysical Journal, 237, 692

Laurikainen, E., Salo, H., & Buta, R. 2004, The Astrophysical Journal, 607, 103

Lawrence, A., Warren, S. J., Almaini, O., et al. 2007, Monthly Notices of the Royal Astronomical Society, 379, 1599

Lee, G.-H., Woo, J.-H., Lee, M. G., et al. 2012, 13

Lee, J., & Pen, U.-L. 2007, The Astrophysical Journal, 670, L1

Lilly, S., Schade, D., Ellis, R., et al. 1998, The Astrophysical Journal, 500, 75

Lintott, C. J., Schawinski, K., Slosar, A., et al. 2008, Monthly Notices of the Royal Astronomical Society, 389, 1179

Lintott, C. J., Schawinski, K., Keel, W., et al. 2009, Monthly Notices of the Royal Astronomical Society, 399, 129

Loveday, J., Norberg, P., Baldry, I. K., et al. 2011, arXiv:1111.0166

Marshall, P. J., Verma, A., More, A., et al. 2016, Monthly Notices of the Royal Astronomical Society, 455, 1171

Martin, D. C., Fanson, J., Schiminovich, D., et al. 2005, The Astrophysical Journal, 619, L1

Martin, D. C., Wyder, T. K., Schiminovich, D., et al. 2007a, The Astrophysical Journal Supplement Series, 173, 342

—. 2007b, The Astrophysical Journal Supplement Series, 173, 342

Martinet, L., & Friedli, D. 1997, Astronomy and Astrophysics, 323

Martini, P. 2004, in The Interplay Among Black Holes, Stars and ISM in Galactic Nuclei, ed. T. Storchi-Bergman, L. Ho, & H. Schmitt, 235–241

Martini, P., Regan, M. W., Mulchaey, J. S., & Pogge, R. W. 2003, The Astrophysical Journal, 589, 774

Masters, K. L., Mosleh, M., Romer, A. K., et al. 2010, Monthly Notices of the Royal Astronomical Society, 405, 783

Masters, K. L., Nichol, R. C., Hoyle, B., et al. 2011, Monthly Notices of the Royal Astronomical Society, 411, 2026

Masters, K. L., Nichol, R. C., Haynes, M. P., et al. 2012, Monthly Notices of the Royal Astronomical Society, 424, 2180

McCracken, H. J., Milvang-Jensen, B., Dunlop, J., et al. 2012, Astronomy & Astrophysics, 544, A156

Melvin, T., Masters, K., Lintott, C., et al. 2014, 18

MenendezDelmestre, K., Sheth, K., Schinnerer, E., Jarrett, T. H., & Scoville, N. Z. 2007a, The Astrophysical Journal, 657, 790

—. 2007b, The Astrophysical Journal, 657, 790

Merloni, A., Bongiorno, A., Bolzonella, M., et al. 2010, The Astrophysical Journal, 708, 137

Mignoli, M., Zamorani, G., Scodeggio, M., et al. 2009, Astronomy and Astrophysics, 493, 39

Mihos, J. C., & Hernquist, L. 1994, The Astrophysical Journal, 431, L9

—. 1996, The Astrophysical Journal, 464, 641

Moles, M., Marquez, I., & Perez, E. 1995, The Astrophysical Journal, 438, 604

Moore, B., Katz, N., Lake, G., Dressler, A., & Oemler, A. 1996, Nature, 379, 613

Moore, B., Lake, G., Quinn, T., & Stadel, J. 1999, Monthly Notices of the Royal Astronomical Society, 304, 465

Moran, S. M., Ellis, R. S., Treu, T., et al. 2006, The Astrophysical Journal, 641, L97

Morselli, L., Renzini, A., Popesso, P., & Erfanianfar, G. 2016, Monthly Notices of the Royal Astronomical Society, 462, 2355

Mulchaey, J. S., & Regan, M. W. 1997, The Astrophysical Journal, 482, L135

Nair, P. B., & Abraham, R. G. 2010, The Astrophysical Journal Supplement Series, 186, 427

Negroponte, J., & White, S. D. M. 1983, Monthly Notices of the Royal Astronomical Society, 205, 1009

Odewahn, S. C., Cohen, S. H., Windhorst, R. A., & Philip, N. S. 2002, The Astrophysical Journal, 568, 539

Oesch, P. A., Carollo, C. M., Feldmann, R., et al. 2010, The Astrophysical Journal, 714, L47

Oh, K., Sarzi, M., Schawinski, K., & Yi, S. K. 2011, The Astrophysical Journal Supplement Series, 195, 13

Oh, S., Oh, K., & Yi, S. K. 2012, The Astrophysical Journal Supplement Series, 198, 4

Peebles, P. J. E., Harrison, E., Peebles, P. J. E., & Harrison, E. 1994, 381–381, doi:10.1119/1.17585

Peng, C. Y., Ho, L. C., Impey, C. D., & Rix, H.-W. 2002, The Astronomical Journal, 124, 266

Peng, Y., Maiolino, R., & Cochrane, R. 2015, Nature, 521, 192

Peng, Y.-j., Lilly, S. J., Kovač, K., et al. 2010, The Astrophysical Journal, 721, 193

Planck Collaboration, Ade, P. A. R., Aghanim, N., et al. 2013, 69

—. 2015, arXiv:1502.01589

Poggianti, B. M., Smail, I., Dressler, A., et al. 1999, The Astrophysical Journal, 518, 576

Pontzen, A., Tremmel, M., Roth, N., et al. 2017, Monthly Notices of the Royal Astronomical Society, 465, 547

Postman, M. Geller, M. 1984, The Astrophysical Journal, 281, 95

Powell, M. C., Urry, C. M., Cardamone, C. N., et al. 2017, The Astrophysical Journal, 835, 22

Quilis, V., Moore, B., & Bower, R. 2000, Science, 288, 1617

Raddick, M. J., Bracey, G., Gay, P. L., et al. 2010, Astronomy Education Review, 9, 15

Richstone, D., Ajhar, E. A., Bender, R., et al. 1998, Nature, 385

Ryden, B., & Ryden, B. 2016, Introduction to Cosmology

S. Michaels, A. W. Shouse, H. A. S. 2008, Ready, Set, SCIENCE! Putting Research to Work in K-8 Science Classrooms (Washington, DC: The National Academies Press), doi:10.17226/11882

Salim, S., Charlot, S., Rich, R. M., et al. 2005, The Astrophysical Journal, 619, L39

Salimbeni, S., Giallongo, E., Menci, N., et al. 2008, Astronomy and Astrophysics, 477, 763

Sandage, A. 1961, The Hubble Atlas of Galaxies (Washington: Carnegie Institution)

Sarzi, M., Shields, J. C., Schawinski, K., et al. 2010, Monthly Notices of the Royal Astronomical Society, 402, 2187

Scarlata, C., Carollo, C. M., Lilly, S., et al. 2007, The Astrophysical Journal Supplement Series, 172, 406

Schawinski, K., Thomas, D., Sarzi, M., et al. 2007, Monthly Notices of the Royal Astronomical Society, 382, 1415

Schawinski, K., Lintott, C., Thomas, D., et al. 2009, Monthly Notices of the Royal Astronomical Society, 396, 818

Schawinski, K., Urry, C. M., Virani, S., et al. 2010, 22

Schawinski, K., Urry, C. M., Simmons, B. D., et al. 2014, 21

Schaye, J., Crain, R. A., Bower, R. G., et al. 2014, Monthly Notices of the Royal Astronomical Society, 446, 521

Schweizer, F. 1982, The Astrophysical Journal, 252, 455

Schweizer, F., Seitzer, P., Faber, S. M., et al. 1990, The Astrophysical Journal, 364, L33

Scoville, N., Capak, P., Giavalisco, M., et al. 2007, in AIP Conference Proceedings, Vol. 943 (AIP), 221–228

Scoville et al., N. Z. 1988, The Astrophysical Journal Letters, 327, L61

Seigar, M. S., & James, P. A. 1998, 11

Sellwood, J. A., & Wilkinson, A. 1993, Reports on Progress in Physics, 56, 173

Shen, J., & Sellwood, J. A. 2004, The Astrophysical Journal, 604, 614

Sheth, K., Regan, M. W., Scoville, N. Z., & Strubbe, L. E. 2003, The Astrophysical Journal, 592, L13

Sheth, K., Vogel, S. N., Regan, M. W., Thornley, M. D., & Teuben, P. J. 2005, The Astrophysical Journal, 632, 217

Sheth, K., Elmegreen, D. M., Elmegreen, B. G., et al. 2008, The Astrophysical Journal, 675, 1141

Sheth, K., Regan, M., Hinz, J. L., et al. 2010, Publications of the Astronomical Society of the Pacific, 122, 1397

Shlosman, I., Begelman, M. C., & Frank, J. 1990, Nature, 345, 679

Shlosman, I., Frank, J., & Begelman, M. C. 1989, Nature, 338, 45

Silk, J., Cintio, A. D., & Dvorkin, I. 2013, arXiv:arXiv:1312.0107v1

Simmons, B. D., Lintott, C., Schawinski, K., et al. 2012, arXiv:1207.4190

Simmons, B. D., Melvin, T., Lintott, C., et al. 2014, Monthly Notices of the Royal Astronomical Society, 445, 3466

Simon, P., Hetterscheidt, M., Wolf, C., et al. 2009, Monthly Notices of the Royal Astronomical Society, 398, 807

Singh, R., van de Ven, G., Jahnke, K., et al. 2013, Astronomy & Astrophysics, 558, A43

Skibba, R. A., Masters, K. L., Nichol, R. C., et al. 2012, Monthly Notices of the Royal Astronomical Society, 423, 1485

Skrutskie, M. F., Cutri, R. M., Stiening, R., et al. 2006, The Astronomical Journal, 131, 1163

Smethurst, R. J., Lintott, C. J., Bamford, S. P., et al. 2017, arXiv:1704.06269

Smethurst, R. J., Lintott, C. J., Simmons, B. D., et al. 2016, Monthly Notices of the Royal Astronomical Society, 463, 2986

Somerville, R. S., Hopkins, P. F., Cox, T. J., Robertson, B. E., & Hernquist, L. 2008, Monthly Notices of the Royal Astronomical Society, 391, 481

Springel, V., Di Matteo, T., & Hernquist, L. 2005, The Astrophysical Journal, 620, L79

Stanford, S. A., & Bushouse, H. A. 1991, The Astrophysical Journal, 371, 92

Steinhauser, D., Schindler, S., & Springel, V. 2016, arXiv:1604.05193

Stern, D., Assef, R. J., Benford, D. J., et al. 2012, The Astrophysical Journal, 753, 30

Strateva, I., Ivezić, Ž., Knapp, G. R., et al. 2001, The Astronomical Journal, 122, 1861

Strauss, M. A., Weinberg, D. H., Lupton, R. H., et al. 2002, The Astronomical Journal, 124, 1810

Thronson et al., H. 1989, The Astrophysical Journal, 343, 158

Toomre, A. 1977, Evolution of Galaxies and Stellar Populations

Tully, R.B., Mould, J.R., Aaronson, M. 1982, The Astrophysical Journal, 257, 527

van den Bergh, S. 1976, The Astrophysical Journal, 206, 883

van Dokkum, P. G., Quadri, R., Marchesini, D., et al. 2006, The Astrophysical Journal, 638, L59

Vogelsberger, M., Genel, S., Springel, V., et al. 2014, Monthly Notices of the Royal Astronomical Society, 444, 1518

Warren, S. J., Cross, N. J. G., Dye, S., et al. 2007, arXiv:0703037

Whyte, L. F., Abraham, R. G., Merrifield, M. R., et al. 2002, Monthly Notices of the Royal Astronomical Society, 336, 1281

Willett, K. W., Lintott, C. J., Bamford, S. P., et al. 2013, Monthly Notices of the Royal Astronomical Society, 435, 2835

Willett, K. W., Schawinski, K., Simmons, B. D., et al. 2015, Monthly Notices of the Royal Astronomical Society, 449, 820

Willett, K. W., Galloway, M. A., Bamford, S. P., et al. 2016, 32

Wright, E. L., Eisenhardt, P. R. M., Mainzer, A. K., et al. 2010, The Astronomical Journal, 140, 1868

Wright, G. S., James, P. A., Joseph, R. D., & McLean, I. S. 1990, Nature, 344, 417

Wyder, T. K., Martin, D. C., Schiminovich, D., et al. 2007, arXiv:0706.3938

Yan, R., & Blanton, M. R. 2012, The Astrophysical Journal, 747, 61

Yang, G., Chen, C.-t. J., Vito, F., et al. 2017, The Astrophysical Journal

Zhou, Z.-M., Cao, C., & Wu, H. 2014, The Astronomical Journal, 149, 1

Zubovas, K., & Bourne, M. A. 2017, arXiv:1703.10782